International journal
for science, technics and
innovations for the industry

MACHINES TECHNOLOGIES MATERIALS

ISSN PRINT 1313-0226
ISSN WEB 1314-507X
Issue 4 / 2018
YEAR XII

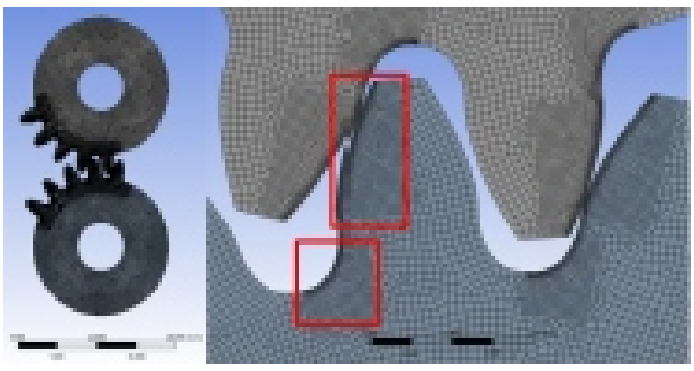

Published by
Scientific technical
Union of Mechanical Engineering "INDUSTRY 4.0"

MACHINES. TECHNOLOGIES. MATERIALS

INTERNATIONAL SCIENTIFIC JOURNAL

PUBLISHER

SCIENTIFIC TECHNICAL UNION OF MECHANICAL ENGINEERING "INDUSTRY 4.0"

108, Rakovski Str., 1000 Sofia, Bulgaria
tel. (+359 2) 987 72 90,
tel./fax (+359 2) 986 22 40,
office@stumejournals.com
www.stumejournals.com

ISSN PRINT 1313-0226, ISSN WEB 1314-507X, YEAR XII, ISSUE 4 / 2018

MACHINES. TECHNOLOGIES. MATERIALS

INTERNATIONAL SCIENTIFIC JOURNAL

ISSN PRINT 1313-0226, ISSN WEB 1314-507X, YEAR XII, ISSUE 4 / 2018

C O N T E N T S

MACHINES

TECHNOLOGIES

MATERIALS

DESIGN AND PERFORMANCE ANALYSIS OF OBSTRUCTION FLOW MEASUREMENT DEVICES FOR LOW AIR FLOW RATES USING CFD ANALYSIS

PhD. Murat Unverdı, Assist. Prof. PhD. Hasan Kucuk
Faculty of Engineering, Department of Mechanical Engineering, Sakarya University, 54050, Serdivan, Sakarya, Turkey

muratunverdi@gmail.com, kucuk@sakarya.edu.tr (Corresponding author)

Abstract: *This study, considering need of fresh air in the air-conditioning system in a small residence, geometrical dimensions of a flow nozzle and an orifice plate were determined by theoretical equations in the literature. The measurement performances of designed flow meters were compared with numerical method using Computational Fluid Dynamics (CFD). The measured air flow rate is in the range of 80-300 m^3/h and Reynolds numbers at the inlet of flow meters are 12,000-46,000. The β ratio of designed flow meters is chosen to be ≅ 0.45 in order to avoid excessive increase of pressure drop. Three dimensional numerical models were created to control the accuracy of flow meters. The results from numerical solution show that permanent pressure loss in the orifice plate is 2.6 times greater than the flow nozzle. Lower pressure and energy loss occur in the flow nozzle compared to the orifice plate. In a system where continuous measurement for the purpose of velocity control of fans is carried out, it has been found that electric power consumption of the fans will increase by 4.85 W and 12.42 W, respectively, at the flow rates of 150 and 200 m^3/h for flow nozzle.*

Keywords: *FLOW NOZZLE, ORIFICE PLATE, COMPUTATIONAL FLUID DYNAMICS (CFD), FLOW MEASUREMENT, HEAT RECOVERY VENTILATOR*

1. Introduction

Flow rate or flow measurement has evolved over years to meet increased accuracy requirements as the worth of measured fluid increases. For example; The Romans controlled water allocation for each family 4,000 years ago by measuring flow in the aqueduct. The Chinese controlled flow of salt water used in the production of salt, which was a very valuable spice at that time. Control of many different processes in similar situations is the main cause of flow rate measurement. Flow measurement became more widespread to control total flow and charge of consumption in later periods **[1]**.

At the beginning of the 1700s, Professor Poleni made his first studies to examine discharge of fluid from a section. Bernoulli developed a theory about head meter at the same time. In 1730, Pitot published a study on the meter. Venturi in the late 1790s and Herschel in 1887, studied similar to the paper of the Pitot. In the mid-1800s in London, first examples of positive displacement flow meters suitable for commercial use were seen. At the beginning of the 1900s, positive displacement meters were first categorized in the United States (Baltimore Gas Light Company) when gas-fuel industry started to develop. Flow rate and flow measurement until today has continued to evolve and evolve as the needs for industrial developments. Developments in flow rate measurement will continue as long as mankind uses gas and liquid energy sources that are required to measure the flow **[1]**.

Flow meters are measuring devices used to quantitatively determine flow rate of a fluid through a pipe, for example, natural gas, oil or water. The spread of measures to save energy and protect the environment in practice increases importance of flow measurement. For example; flow measurement is very important to ensure that compressed air systems operate efficiently and forceful. The largest share of total cost of compressed air systems belongs to electricity. Initial investment and maintenance costs are lower than electricity. 90% of the electricity consumed by a modern compressor is converted to heat, only 10% is used to compress air. For this reason, compressed air is 10 times more expensive than electricity. Common practice in compressed air systems is to measure electricity consumption. However, only a few companies measure pressurized air consumption. The statistics show that 30% of the compressed air is lost by leakages and that these leakages can be detected and eliminated **[2]**.

Industrial applications that constitute 40% of total CO_2 emissions are another important example of flow measurement. These CO_2 emissions are largely due to burning of fossil fuels (such as coal, oil, natural gas) used to generate electricity. As is known, CO_2 is responsible for global warming. While energy is a scarce resource and protection of the environment is an important issue, flow measurements help in the detection and analysis of consumption and leaks in systems. This allows to reduce energy consumption and costs **[2]**.

Since monetary returns of flow meters can be very large, the flow measurement is also important for economic control. In the journal "Flow Measurement and Instrumentation" (Volume 1, issue 1, 1989), it is emphasized that annual costs controlled by the flow meter are in the order of $10,000 million (an average of €10,000 billion per year). So even 1% uncertainty in the measurements represents a significant value **[3]**.

Accurate measurement of the flow of liquids and gases is indispensable for protection of quality of industrial processes. In fact, most of the industrial control cycles are often controlled by flow of liquids or gases in order to achieve the purposes **[4]**.

When physical measurements are made, choice of method is usually performed first. The simplest method should be aimed at providing simplicity, accuracy and precision in selecting a method. The best way to measure average flow rate of water through a pipe for a long period of time is to weigh the amount of water passing over a given time period or measure the volume. But weighing method cannot be applied to gases such as air. Volumetric measurement methods, which form the basis of widely used gas meters for fluids such as air, should be preferred. However, their use is very limited, because of engineers can only measure smaller flow rates of two standard types than ones that are of interest. For this reason, most of direct measurement methods for air flow rate in engineering applications cannot be used. It is usually necessary to measure some physical effects due to flow. There are three physical effects determined by experience and used in flow measurement: Movement-related pressure changes, mechanical effects that are induced by inducing rotation speed to a rotor with the light wings placed in the flow, physical changes similar to a hot wire cooling held in an air flow and heated by an electric current. The first of these is the most important because a measuring device properly designed and positioned within flow causes a characteristic pressure difference which can be measured with a pressure gauge **[5]**.

The equipment used in the measurement of pressure can be divided into two separate groups according to whether or not the air enter. The non-flow-through equipment is an anemometer consisting of two independent pipes of different shapes. An additional pressure effect occurs in a hole or a group of holes facing upstream of the airflow. The other ends of these tubes are connected to a differential pressure gauge that measures pressure difference between two groups of holes facing the downstream of the flow on the anemometer.

Anemometers with flow inside are more sensitive than pressure tube anemometers. Commonly used examples are; orifice plate,

flow nozzle and less used venturi tube. Such tools should be used under strict control conditions for proper operation **[5]**.

There may be various requirements in the flow measurement, such as measurement of volumetric or mass flow rate, the fluid being measured is gas or liquid, the measurement may be obstructed or unobstructed. As a result, there are different flow measurement methods used in the industry. Some of those; (a) Obstruction type, (differential pressure or variable area) (b) Inferential turbine type (c) Electromagnetic (d) Positive displacement (e) Fluid dynamic vortex shedding (f) Anemometer, (g) Ultrasonic and (h) Mass flow meter (Coriolis) **[4]**.

There are two types of obstruction flow meters: differential pressure type and variable field. Orificemeter, venturimeter and pitot tube enter the first group, while rotameter is in the second group. In all of these, an obstacle is created in the areas where flow passes, and pressure drop across the obstacle is associated with the flow rate. Differential pressure type flow meters are one of the most widely used flow meters. Due to their flexibility, cost and simplicity, they are used in many applications. Pressure differential producing flow meters can be used in almost all low viscosity fluid flow measurements and in a majority of gas applications **[4]**.

In this study, measurement performances of a flow nozzle and an orifice plate designed to be used in an experimental study of air to air heat recovery ventilation used in air conditioning systems were compared with numerical methods. The dimensions of the flow nozzle and orifice plate suitable for flow rate range to which the experimental study can be carried out are determined by theoretical equations found in the literature. The solid models of flow meters was designed in computer with SOLIDWORKS software. The expected measurement results from theoretical equations were compared with result of Computational Fluid Dynamic analyzes in SOLIDWORKS Flow Simulation software.

2. Problem definitions

The fans in the air conditioning and ventilation systems are usually selected at capacities above the requirements, with uncertainties and safety concerns. This excess capacity causes initial investment costs to increase and unnecessary energy loss during operation. The power that is consumed by fan is proportional to cube of flow rate. Therefore, a small decrease in flow rate will greatly reduce power requirement. For example, reducing the flow rate by 20% can reduce the power requirements by half **[6]**. Common methods for controlling flow and energy saving in fans are: (a) use of fan discharge damper b) use of fan suction damper, and (c) use of a variable speed drive **[7]**.

In case of using fan discharge damper, additional pressure loss is created by fan discharge damper, the loss characteristic of system is changed, fan outlet pressure is increased and flow rate is reduced. The use of fan suction damper is similar to the use of the fan discharge damper, in the fan suction line. As the fan suction flow rate decreases consequently the pressure at the outlet also decreases, flow rate varies according to system specifications in the case of fan suction damper. When the air flow rate drops to 60% of the nominal, a reduction of about 45% in power consumption can be achieved. If fan velocity is decreased, the fan characteristic is changed and both flow rate and pressure loss are reduced at the same time. In this process, without any significant change in fan efficiency, when the air flow drops to 60% of the nominal, a reduction of up to 75% in power consumption can be achieved. In summary, in the ventilation system using a fan operating at constant velocity: use of fan suction damper is 30% and variation by changing the rotational speed of fan is 70%, which saves electrical energy, according to the application with the use of fan discharge damper.

In the variable-flow systems, electrical energy consumption is less than the fixed-flow systems. This is because, air flow rate can be increased where the fresh air needs to be increased according to condition of ventilated residence, air flow rate can decrease when the residence is not being used, or when there are few people in the residence. This saves considerable electrical energy **[6, 7]**.

In this study, considering fresh air requirement in the ventilation system in a small residence, measured air flow range was determined as 80-300 m^3/h. The Reynolds numbers at the inlet of flow meters designed for these flow rates are in the range of 12,000-46,000. In the calculations, air temperature was assumed to be 20°C. Therefore, properties of the air ρ_{air} = 1.204 kg/m^3, μ_{air}= 1.825x10^{-5} kg/ms and ν_{air} = 1.516x10^{-5} m^2/s **[8]**.

The inner diameter of duct to carry air to the heat recovery ventilator is 152 mm. The flow rate in ducts and channels of ventilation system can be calculated by measuring decrease in pressure, due to throttling of cross-section and depending on increase in flow velocity of the throttling section. The permanent pressure difference between two pressure taps along the flow can be measured with a differential pressure transducer or manometer, or flow rate can be measured by obstructing the flow with a flow meter.

In this study, an orifice plate and a flow nozzle are designed by making necessary calculations to measure the same flow rate and performance of two flow meters is compared with numerical solution. The designed the flow nozzle and the orifice plate β ratio were chosen to be ≅0.45 so that avoid excessive increase of pressure drop. The minimum Reynolds numbers in the flow rate range to be measured are limited to 10,000 or more at the inlet of both flow meters.

3. Design of flow meters and determination of volumetric flow rates

3.1 ASME Long Radius Nozzle

The flow nozzle is an obstruction flow meter with a throttling in the flow direction toward outlet. A schematic cross-sectional view showing the characteristic dimensions of the ASME long-radius, low β-ratio flow nozzle is shown in Fig. 1. In the case of a low β-ratio flow nozzle, β ratio is recommended to be less than 0.5 **[9]**.

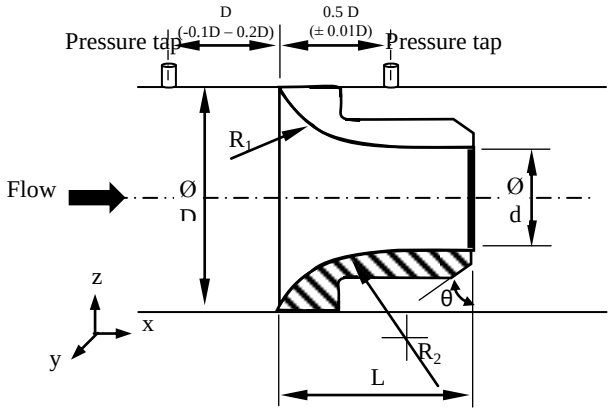

Fig. 1. *Schematic cross-sectional view of flow nozzle* ***[10]****.*

The equations used to calculate flow rate in the measurements made with the flow nozzle are as follows:

Method 1: Determination of volumetric flow rate by calculating discharge coefficient:

The discharge coefficient C_d is calculated by the following equation **[11]**.

$$C_d = 0.9975 - (6.53\,\beta^{0.5}/Re^{0.5}) \quad (1)$$

$$\beta = d/D \quad (2)$$

Where, β is the ratio of diameter of the outlet to diameter of inlet of the flow nozzle, Re is Reynolds number at the inlet.

The volumetric flow rate ($\dot{\forall}$) is calculated by substituting the discharge coefficient C_d with the following equation **[12]**.

$$\dot{\forall} = A_2\, C_d \sqrt{2\,\Delta p / \left(\rho\,(1-\beta^4)\right)} \tag{3}$$

Where A_2 (m^2) is the area of outlet section of the flow nozzle, Δp (Pa) is the pressure difference measured between inlet and outlet of the flow nozzle, ρ (kg/m^3) is density of fluid.

Method 2: Determination of volumetric flow rate using the discharge coefficient (C_d) read from the graphs **[9]**:

The discharge coefficient C_d is obtained depending on β and Reynolds numbers. The velocity of approach factor (M) is calculated by the following equation.

$$M = 1/\sqrt{1-(A_2/A_1)^2} \tag{4}$$

A_1 and A_2 are cross-sectional areas at the inlet and outlet of the flow nozzle. The volumetric flow rate is calculated by following equation using measured pressure drop (Δp) **[9]**.

$$\dot{\forall} = C\,M\,A_2 \sqrt{2/\rho}\ \sqrt{\Delta p} \tag{5}$$

Where A_2 (m^2) is the area of outlet section of the flow nozzle, Δp (Pa) is the pressure difference measured between inlet and outlet of the flow nozzle, ρ (kg/m^3) is the density of fluid.

3.2 Orifice Plate

The orifice plate is the simplest obstruction flow meter with low cost, design and manufacturing that occupies very little space because it consists of a bored plate in the middle. However, sudden contraction and expansion in the flow cross section of the orifice plate generates of significant vortex. This leads to large head losses and permanent pressure loss. A schematic cross-sectional view of the characteristic dimensions of the orifice plate is shown in Fig 2. β ratio for orifices is recommended in the range of 0.25-0.75 **[11]**.

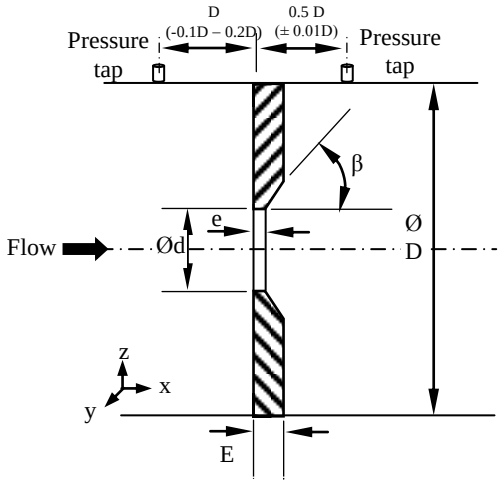

Fig. 2. *Schematic cross-sectional view of orifice plate* ***[12]****.*

The equations used for calculation of flow rate for the orifice plate are as follows:

Method 1: Determination of volumetric flow rate by calculating discharge coefficient:

The discharge coefficient C_d is calculated by the following equation **[11]**.

$$C_d = 0.5959 - 0.0312\beta^{2.1} - 0.184\beta^{8} + (91.71\beta^{2.5}/Re^{0.75}) \tag{6}$$

Where, β is the ratio of diameter of the outlet to diameter of inlet in the flow nozzle, Re is Reynolds number in the inlet.

The volumetric flow rate ($\dot{\forall}$) is calculated by substituting the discharge coefficient C_d with the following equation **[12]**.

$$\dot{\forall} = A_2\, C_d \sqrt{2\,\Delta p / \left(\rho\,(1-\beta^4)\right)} \tag{7}$$

Where A_2 (m^2) is the area of bore section of the orifice plate, Δp (Pa) is the pressure difference measured between inlet and outlet of the orifices plate, ρ (kg/m^3) is the density of fluid.

Method 2: The discharge coefficient (C_d) is arranged according to Reynolds numbers in the pipe section with β and is determined by reading from the graph **[9]**. This method is not used for the designed orifices because inner diameter of the duct to be studied is D=152 mm and the discharge coefficient graph given for orifices is out of range diameter.

Hydraulic power loss due to permanent pressure loss created by the flow meters and additional electrical power to be consumed in the fans by assuming 65% of fan efficiency is calculated by equations (8) and (9).

$$\dot{W}_{hp} = \dot{\forall}\,\Delta p \tag{8}$$

$$\eta_f = \dot{W}_{hp} \,/\, \dot{W}_{ee} \tag{9}$$

Where W_{hp} is the hydraulic power required to overcome pressure loss, η_f is the fan efficiency and W_{ee} is the electrical power consumed by the fan motor.

4. Numerical Modeling for Flow Meters

The Reynolds number at the inlet of flow meters for the studying air flow rate range of 80-300 m^3/h is 12,000-46,000. In accordance with preliminary design criteria mentioned in Section 3, the geometric dimensions of flow nozzle and orifice plate were determined for β=0.45. Before experimental study, numerical models of flow meters were developed to check the accuracy of designed flow meters. The numerical modeling of flow meters were performed by placing in a duct with a circular section and a length of 5 times the inner diameter. The average static pressures in the cross sections that follow D before flow meter inlet and D/2 after flow meter inlet, which is static pressure measurement sections defined in the standard, were calculated in numerical solutions. These pressures are used to determine pressure differences through the flow meters. The solutions of the numerical models were carried out with the trial version of SOLIDWORKS Flow Simulation software. In numerical solutions, a modified k-ε turbulence model is used with damping function proposed by Lam and Bremhorst **[13]**.

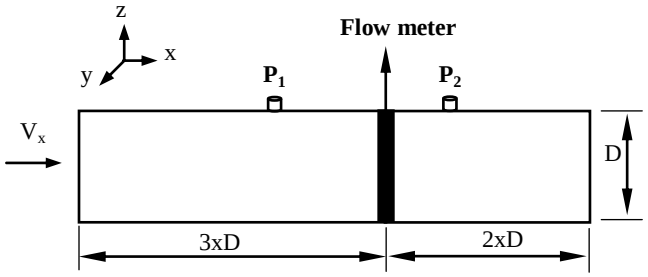

Fig. 3. *Numerical model and boundary conditions.*

A schematic drawing of the generated numerical model and boundary conditions are given in Fig 3. The modified k-ε turbulence model with damping functions proposed by Lam and Bremhorst describes laminar, turbulent, and transitional flows of homogeneous fluids consisting of the following turbulence conservation laws:

$$\frac{\partial \rho k}{\partial t} + \frac{\partial \rho k u_i}{\partial x_i} = \frac{\partial}{\partial x_i}\left(\left(\mu + \frac{\mu_t}{\sigma_k}\right)\frac{\partial k}{\partial x_i}\right) + \tau_{ij}^R \frac{\partial u_i}{\partial x_j} - \rho\varepsilon + \mu_t P_B \tag{10}$$

$$\frac{\partial \rho \varepsilon}{\partial t} + \frac{\partial \rho \varepsilon u_i}{\partial x_i} = \frac{\partial}{\partial x_i}\left(\left(\mu + \frac{\mu_t}{\sigma_\varepsilon}\right)\frac{\partial \varepsilon}{\partial x_i}\right) + C_{\varepsilon 1}\frac{\varepsilon}{k}\left(f_1 \tau_{ij}^R \frac{\partial u_i}{\partial x_j} + C_B \mu_t P_B\right) - f_2 C_{\varepsilon 2}\frac{\rho \varepsilon^2}{k} \tag{11}$$

$$\tau_{ij}=\mu s_{ij},\ \tau_{ij}^{R}=\mu_t s_{ij}-\frac{2}{3}\rho k\delta_{ij},\ s_{ij}=\frac{\partial u_i}{\partial x_j}+\frac{\partial u_j}{\partial x_i}-\frac{2}{3}\delta_{ij}\frac{\partial u_k}{\partial x_k} \quad (12)$$

$$P_B=-\frac{g_i}{\sigma_B}\frac{1}{\rho}\frac{\partial \rho}{\partial x_i} \quad (13)$$

$$C_\mu=0.09,\ C_{\varepsilon_1}=1.44,\ C_{\varepsilon_2}=1.92,\ \sigma_k=1,\ \sigma_\varepsilon=1.3,\ \sigma_B=0.9 \quad (14)$$

If $P_B > 0$ for $C_B=1$
If $P_B < 0$ for $C_B=0$

Turbulence viscosity:

$$\mu_t=f_\mu C_\mu \rho k^2/\varepsilon \quad (15)$$

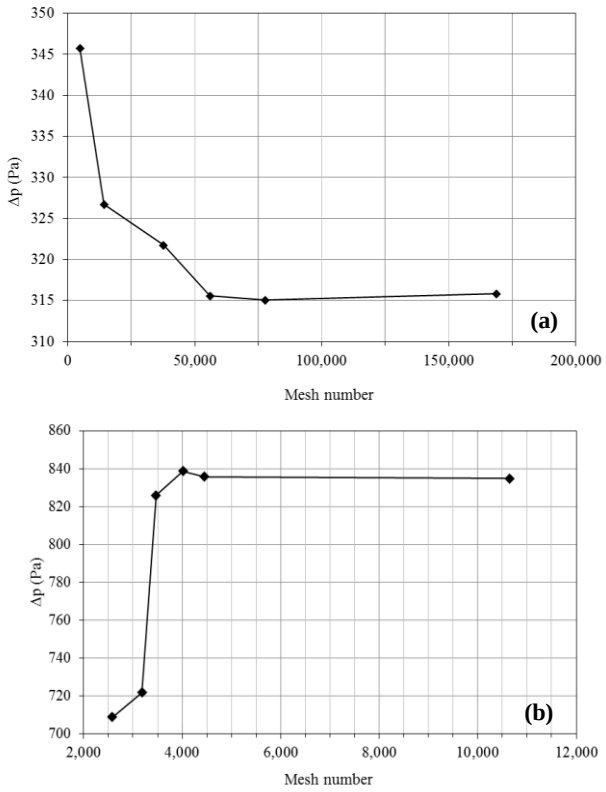

Fig. 4. *Mesh number independence study: (a) flow nozzle and (b) orifice plate.*

Lam and Bremhorst's damping function (f_μ):

$$f_\mu=(1-e^{-0.025R_y})^2(1+20.5/R_t) \quad (16)$$

$$R_y=\rho k^{1/2} y/\mu \quad (17)$$

$$R_t=\rho k^2/\mu\varepsilon \quad (18)$$

Where y is the distance from point to the wall and Lam and Bremhorst's damping function f_1 and f_2 are determined from:

$$f_1=1+(0.05/f_\mu)^3,\ f_2=1-e^{R_t^2} \quad (19)$$

Lam and Bremhorst's damping functions f_μ, f_1, f_2 decrease turbulent viscosity and turbulence energy and increase the turbulence dissipation rate when the Reynolds number R_y based on the average velocity of fluctuations and distance from the wall becomes too small. When $f_\mu=1$, $f_1=1$, $f_2=1$ the approach obtains the original k-ε model.

At the highest volumetric flow rate, for the numerical modeling of the flow meters, independence of mesh studies were carried out with 6 different mesh structures. The results of the mesh structure independence study are given in Fig 4. For the solutions, numerical models with 55,962 elements for the flow nozzle and 4,452 elements for the orifice plate were used. The results are almost constant, after these mesh numbers. Similar mesh structures have been used for other volumetric flow rates. In steady-state numerical solutions, it is assumed that average velocity at the inlet is constant, uniformly distributed and horizontal direction. Furthermore, in solutions where the physical properties of fluid do not change and flow is three-dimensional, and effect of gravity is neglected.

5. Result and Discussion

In order to measure the volumetric flow rate (80-300 m^3/h) of the air for use in an experimental study, a flow nozzle and an orifice plate were designed. The pressure losses in the flow meters were calculated by different calculation methods in the literature. Solid and numerical models of the designed flow meters are generated in SOLIDWORKS software. The performance of flow meters was obtained by numerical analysis in the trial version of SOLIDWORKS Flow Simulation software to verify suggested theoretical equations. The numerical solutions and pressure drops obtained from the suggested equations are compared. Volumetric flow rate changes of permanent pressure drops obtained from the numerical solution and the theoretical equations are given in Fig.5 for flow nozzle.

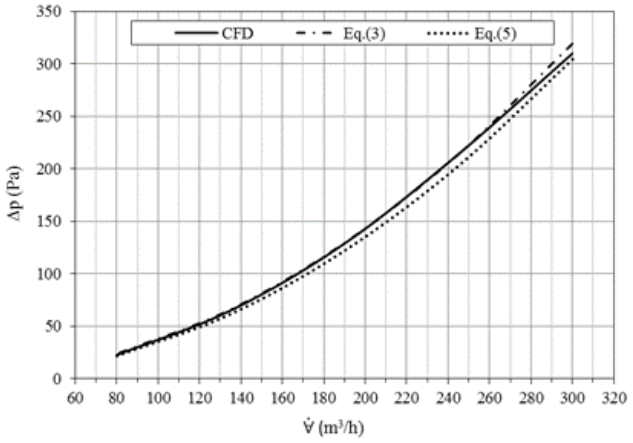

Fig. 5. *Volumetric flow rate dependence of permanent pressure drops for flow nozzle.*

It is seen that difference between the numerical and the theoretical results proposed in Section 3.1 for the flow nozzle is about ±4.5%. These results show that accuracy of measurement of flow nozzles to be used must be experimentally controlled and adjusted. Fig. 6 and 7 show pressure and velocity distributions obtained from the numerical solution in the symmetry plane of duct for the flow rate of 300 m^3/h, respectively.

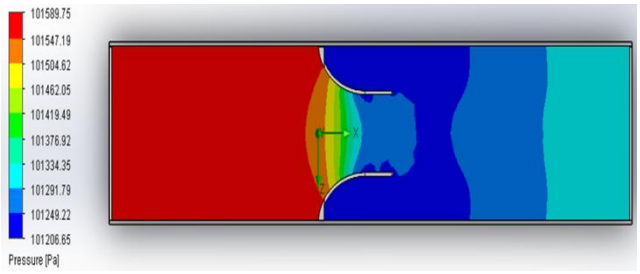

Fig. 6. *Pressure contours in the xz symmetry plane of duct at the flow rate of 300 m^3/h for flow nozzle.*

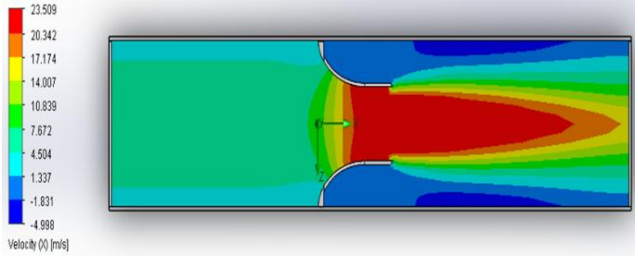

Velocity contours in the xz symmetry plane of duct at the flow rate of 300 m^3/h for flow nozzle

As can be seen from pressure contours, static pressure towards the outlet from the inlet section decreases in the regions where cross section in the flow nozzle starts to change. The velocity increases from the inlet section to the outlet. In other words, as velocity decreases in regions where static pressure increases, the velocity increases in regions where the static pressure decreases. Among pressure taps defined in the standards, permanent pressure loss caused by cross-sectional changes and friction effects is also obtained by numerical solution.

In the case of similar state, changes in permanent pressure drops in the orifice plate obtained from theoretical calculations and numerical solutions are given in terms of volumetric flow rate.

As seen in Fig. 8, difference between numerical and theoretical results from the proposed equations in Section 3.2 for the orifice plate is approximately +2%. Fig. 9 and 10 show pressure and velocity contours obtained from the numerical solutions in the symmetry plane of duct for the flow rate of 300 m^3/h, respectively. The change in the pressure and velocity contours obtained for the orifice plate is similar to the flow nozzle. The relationship between pressure and velocity contours is decreased at the flow velocity to region where the static pressure is increased and increase at the flow velocity to the region where the static pressure decreases.

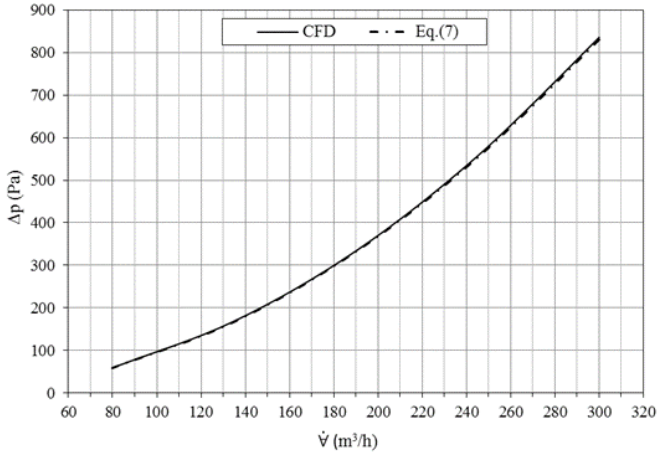

Fig. 8. *Volumetric flow rate dependence of permanent pressure drops for orifice plate.*

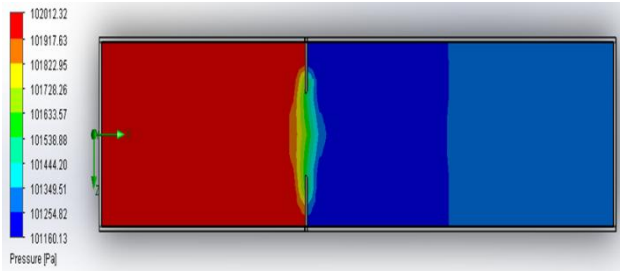

Fig. 9. *Pressure contours in the xz symmetry plane of duct for at the flow rate of 300 m^3/h for orifice plate.*

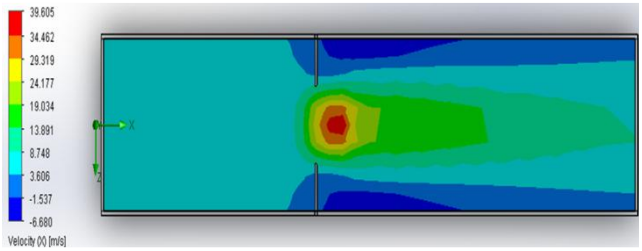

Velocity contours in the xz symmetry plane of duct at the flow rate of 300 m^3/h for orifice plate

When choosing between two flow meters, the measurement accuracy and the permanent pressure loss during measurement must be considered. The performances of the flow meters are compared

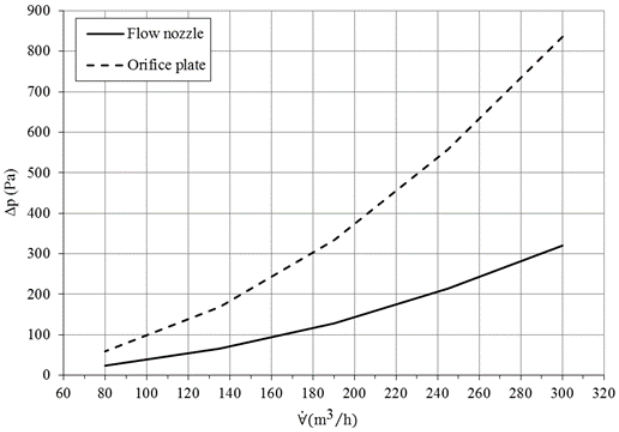

Fig. 11. *Comparison of permanent pressure losses obtained from numerical solution.*

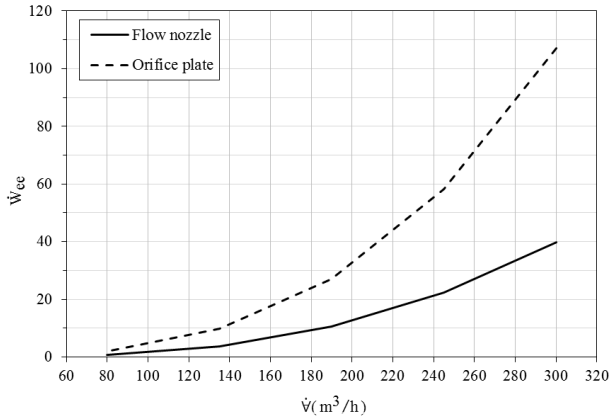

Fig. 12. *Hydraulic lost power depending on the volumetric flow rate in flow meters.*

with each other. Fig. 11 shows the permanent pressure drops obtained from numerical solutions of flow meters at flow rate ranges of 80-300 m^3/h. When looking at Fig. 11, the rate of permanent pressure drop in the flow nozzle is about 1/3 of that in the orifice. In other words, the pressure drop of orifice plate is about 2.6 times higher than the pressure drop in the flow nozzle. From these results, the flow nozzle is more advantageous because of less permanent pressure loss in the measurement of air flow and 1/3 of energy consumption. It was decided to use the flow nozzle in experimental study since it is possible to measure with less auxiliary equipment such as venturimeter which is not used in this study. However, it is also necessary to calculate lost hydraulic power from obstruction flow meters, in situation where continuous flow measurement is required to save energy especially in the fans. The hydraulic lost power in flow meters is given in Fig. 12 depending on the volumetric flow rate. The technical drawing details of the flow meters designed with the proposed calculation methods and investigated by numerical solutions are given in Fig 13.

6. Conclusion

In this study, obstruction flow meters were investigated by numerical method in order to control air flow rate to reduce electricity consumption of fans for ventilation systems used in small residence. The utility of the flow nozzle and orifice plate for controlling the air flow rate by changing the rotational speed of fan motor was compared in terms of additional permanent pressure loss, lost hydraulic power and measurement accuracy.

The hydrodynamic performance of the flow nozzle and orifice plate, which designed with the theoretical expressions proposed for flow meters at flow rates of 80-300 m^3/h, was numerically investigated with the trial version of SOLIDWORKS Flow Simulation software. The numerical and the theoretical results are compared and verified. The difference between numerical results

and recommended expressions is an average ±4.5% for the flow nozzle, while an average +2% for the orifice plate. The technical drawings of the flow nozzle and the orifice in which the design and numerical studies are given. The use of a non-inclusive CFD software gives results in acceptable accuracy in the design of flow meters. The permanent pressure drop in the orifice plate was 2.6 times higher than the flow nozzle. For this reason, the flow nozzle was chosen to be used for measuring the air flow. Reasons for selection of flow nozzle:

- Pressure losses are less than orifice plate (up to 1/3)
- It is less costly than equipment used in the measurement system and other flow meters (such as venturimeter).
- Acceptable precise measurements can be made.

However, it is necessary to calculate lost hydraulic power in addition to permanent pressure loss in systems where continuous measurement such as flow rate control by changing the fan motor revolution for energy saving purposes. Both flow meters cause too much hydraulic power loss for applications where continuous measurement is required.

References

1. LaNasa P.J, Upp, E.L., Fluid Flow Measurement: A Practical Guide to Accurate Flow Measurement (Third Edition), Elsevier Inc., 2014.
2. www.bvrg.com.au/News/Nov2010/Why flow measurement important, Access date: March 7, 2018.
3. Merzkirch W., Fluid Mechanics of Flow Metering, Springer, 2005.
4. Measurement systems, Module 2, Lesson 7, Flow measurement, Version 2 EE IIT, Kharagpur, Access date: March 7, 2018.
5. Ower, E., Pankhurst, R.C., The Measurement of Air Flow (Fifth Edition), Pergamon Press, 1977.
6. Küçükçalı, R., Energy economy and application proposal for air conditioning systems, (in Turkish), www1.mmo.org.tr/resimler/dosya_ekler/fceff75c9ebec6e_ek.pdf, Access date: January 10, 2018.
7. Energy Efficiency Applications: Flow Control in Fans (in Turkish), www.emo.org.tr/ekler/1a08b08ff559dd9_ek.pdf, Access date: January 18, 2018.
8. Cengel, Y., Introduction to Thermodynamics and Heat Transfer (Second Ed.), McGraw-Hill, 2007.
9. Holman, JP., Experimental Methods for Engineers (Eight Ed.), McGraw-Hill, 2012.
10. Measurement of Fluid Flow in Pipes Using Orifice, Nozzle, and Venturi, ASME MFC-3M-2004 [Revision of ASME MFC-3M-1989 (R1995)].
11. Miller, RW., Flow Measurement Engineering Handbook, 3rd ed. New York, McGraw-Hill, 1997.
12. Cengel, YA., Cimbala JM., Fluid Mechanics Fundamentals and Applications Third Ed., McGraw-Hill, 2014.
13. Lam, CKG., Bremhorst, KA., Modified Form of model for Predicting Wall Turbulence. ASME Journal of Fluids Engineering, Vol. 103, pp. 456-460,1981.
14. www.hawkridgesys.com/sites/default/files/resources/enhanced-turbulence-modeling.pdf, Access date: February 27, 2018.

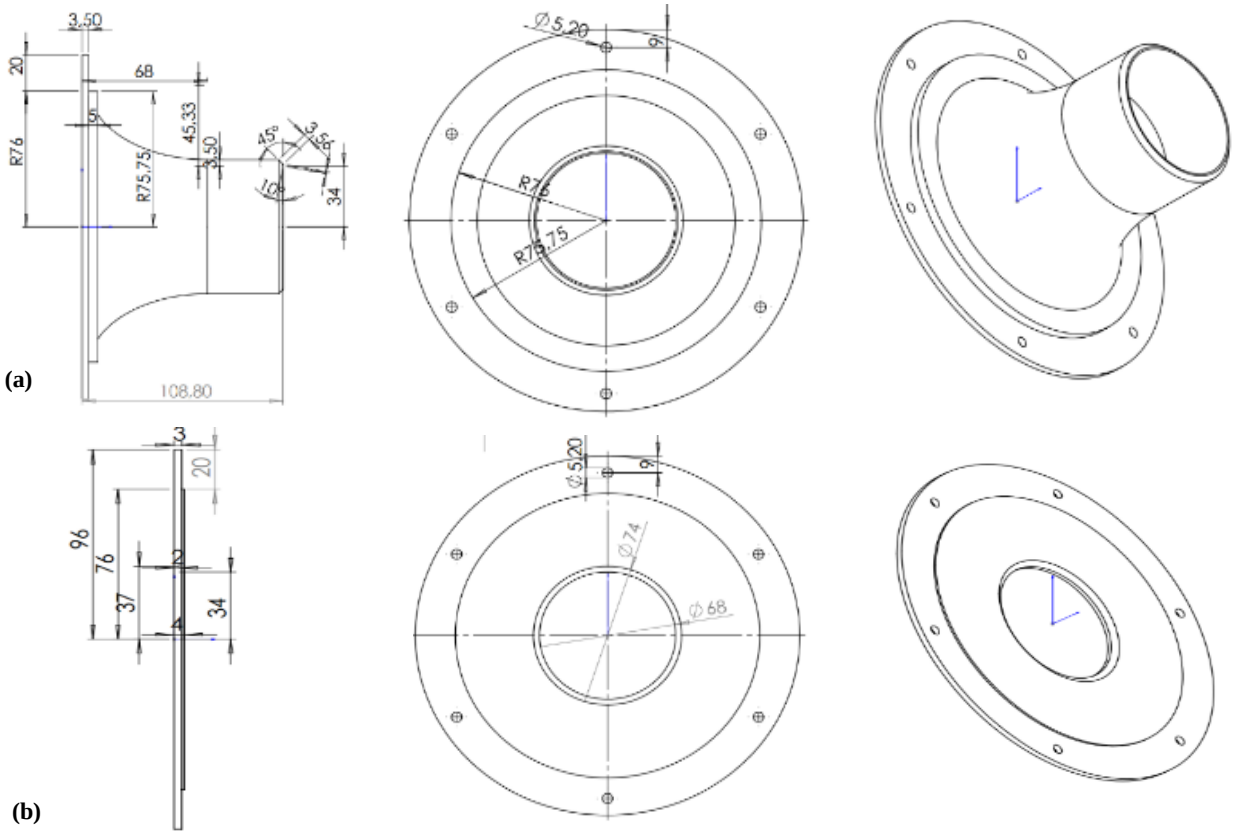

Technical drawing details of the designed flow meters: (a) flow nozzle and (b) orifice plate.

HEAT PUMP HEATING SYSTEM OPTIMISATION

M.Sc. Petrek J., PhD.,
DTI University, Slovakia
E-mail: petrek@dti.sk

Abstract: *The goal of this paper is to minimalize the gap between the heat pump's compressor COP and the system COP_S. A water-water heat pump was installed in a family house without piped floor heating, with 13 radiators, together with a 300 litres thermal storage and 200 litres hot water storage tank. Some measurements are published, taken before and after the system optimisation. The measured compressor COP is compared with theoretical data published by the device producer. The results show that the power consumption was decreased by 15 percent after the system optimisation. The influence of the equithermal curve settings and the power of the submersible pump are analysed and the results are presented. The seasonal COP (SCOP) for Bratislava area is calculated. for the system under consideration.*

Keywords: *HEAT PUMP, COP, ENERGY CONSUMPTION*

1. Introduction

A heat pump is an ecological and economical heat source. Because of high starting investment for families, it is cofinanced by many European countries to decrease CO_2 and other harmful gases emissions caused by heating. The principle of a heat pump is in Fig.1. The heat pump uses the solar energy accumulated in a cool space (heat from ambient) like air, ground or water and pumps it to a warm space, while usually using an electrically driven vapor-compression cycle. In the heating systems, we usually use water for energy transmission between the heat pump and the heated space, where floor, wall, ceiling heating or radiators are installed.

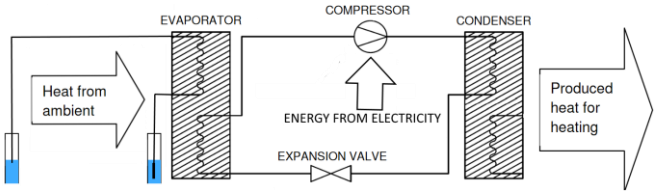

Fig. 1 *Water-water heat pump principle*

The source of ambient heat may be water (water-water system), ground (ground-water system) or air (air-water system). In the central circuit is the compressor, the expansion valve, the condenser and the evaporator. There is a suitable refrigerant in the central circuit pipes (e.g. R410a). Between the compressor, condenser and the expansion valve is a high pressure and the refrigerant condenses to liquid, while losing its thermal energy, which is transferred to the heating system via a heat exchanger. The expansion valve is computer controlled in high-tech devices. The refrigerant pressure between the expansion valve, evaporator and the compressor is relative low and therefore the refrigerant evaporates and changes its state to gaseous in the evaporator, thereby cooling the heat transfer medium in the heat exchanger.

A real advantage of the heat pump heating is high coefficient of performance (COP) factor, which is, for the compressor itself, more than 6.0 for some systems, under some conditions. The system COP factor COP_S may be much lower than compressor's COP. In the system COP_S, not only the energy consumption of the compressor, but also energy consumption of all other pumps and devices, associated in the heating system, are taken into account. The final relative low COP_S may be a disappointment for an investor. We define the COP_S factor as:

$$COP_S = \frac{Q}{E_S},$$

where Q is the heat produced by the system [kWh] and E_S is the energy consumption of the heat pump and all with the heat pump associated systems [kWh]. Fortunately, very high COP factor is not as important as many investors think. The energy saving from the heat pump implementation is:

$$ES = Q - E_S = Q - \frac{Q}{COP_S} = Q \cdot \left(1 - \frac{1}{COP_S}\right)$$

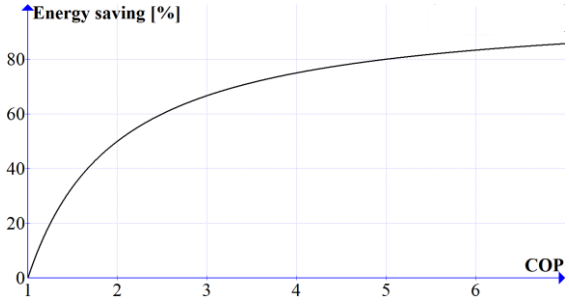

Fig. 2 *Relationship between the system COP and energy saving in comparison with an electrical boiler*

The relationship between the system COP and energy saving *ES* is in Fig. 2. We can state some consequences for a reasonable investment strategy:

1) It makes no economic sense to increase the COP_S over 3.5, if high additional investments are required (e.g. a much more expansive heat pump with an inverter driven compressor [1], in a water-water or ground-water system makes a sense only if there is no space for a storage tank)

2) A bivalent system (with additional electric boiler used during very cold days), with lower investment cost for the energy source and the heat pump, may be more economic. In case of ground-water and water-water systems, some decrease of COP_S during cold days may be compensated also with higher COP_S during not so cold days (most of heating season).

Therefore, before installing the heat pump, a proper system analysis with a project is inevitable for an optimal heat pump service. This paper will help potential investors with some ideas.

2. System descriptiom

In [2] authors analyzed the behavior of an air-water system, in [3] a ground-water system. In this paper, the behavior of a water-water system installed in a family house is analyzed and optimized. The system is described in Fig. 3.

The source of energy is the source well (1) with a water level 7.73 meters under the ground level. The water level does not falter - there is enough water throughout the year. A submersible pump (2) pumps the water through the water-to-refrigerant heat exchanger in the heat pump Mastertherm Aquamaster AQ22Z (3) to the collection well (4) placed 16 meters from the source well (1) in the direction of the underground water flow.

A circulating pump (5) is an accessory of the heat pump and was chosen to be high effective. It circulates the hot water between the head pump (3) and the 300 liters water tank (6). It has power consumption up to 150 Watts and water flow 0.6 l/s. The water tank (6) is installed to reduce heat pump on-off cycles. The heating water circulating pump Wilo Jonos Pico 25/6 (7) pumps the hot water into 13 radiators (8). The total amount of water in the heating system (including the wa ter tank and the heat pump) is 560 liters. The ex-pansion vessel (9) is necessary for the safety of the system.

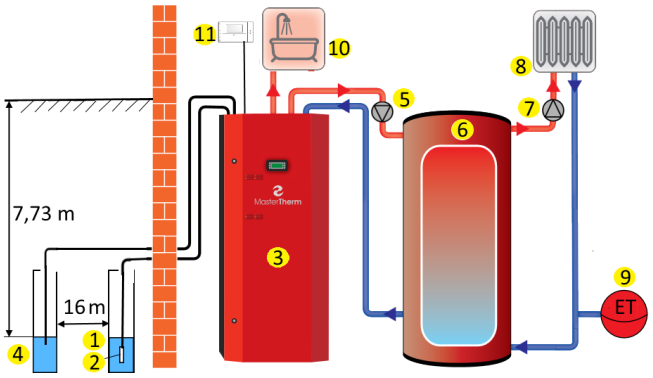

Fig.3 *Described heating system with a heat pump*

The system includes also a three-way valve and another water tank with a heat exchanger for hot water production (10). This is not depictured in Fig.3, because the hot water preparation is not the subject of this paper. We will consider only the heating system.

The system includes also a space terminal (11) with a user interface, thermometer and digital communication with the heat pump.

The described system is monovalent. The house is well insulated and the heat pump power is sufficient for house heating during all season.

3. System optimisation

Let us optimize some system components. The first component to optimize is the submersible pump (2). Its role is to supply the heat pump with the heat from underground water. In our system is its temperature between 13 °C (in winter and spring) and 14 °C (summer and autumn). To increase the compressor COP factor, the temperature gradient in the heat pump, between the "hot" water from the source well and the cold water returning to the collection well, should be as low as possible, which requires a high flow of water. On the other side, higher water flow means greater pressure losses on the pipeline and higher electricity consumption of the submersible pump (2) (Fig.3). We can see from Fig.4 that the pressure loss on the pipeline is a quadratic function of the water flow and better is to use thicker pipes. The pipe must not be coarse. To minimize the power consumption, thick plastic pipes with 5/4" diameter were used between both wells and the heat pump. Our heat pump requires minimal water flow 0.52 l/s, recommended is 0.61 l/s. The first pump tested in our system was Calpeda 4SDF 22/10 (Fig.5). The measured water flow was 0,85 l/s (which is much more than recommended 0,61 l/s), which corresponds with the total pressure loss 2,1 bar in our system.

The measured power consumption of both submersible pump (2) and circulating pump (5) was 939 Watts. In the second test, a lower power pump Calpeda 4SDF 16/9 was used (Fig.6). The measured water flow was 0,65 l/s and the measured power consumption of both submersible pump (2) and circulating pump (5) was 542 Watts, which is 397 Watts less. More important than the power consumption of the submersible pump is the total system consump-

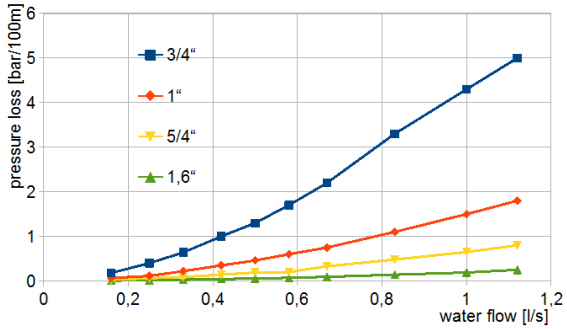

Fig.4 *Pressure loss on plastic pipeline with different pipe diameters as a function of water flow*

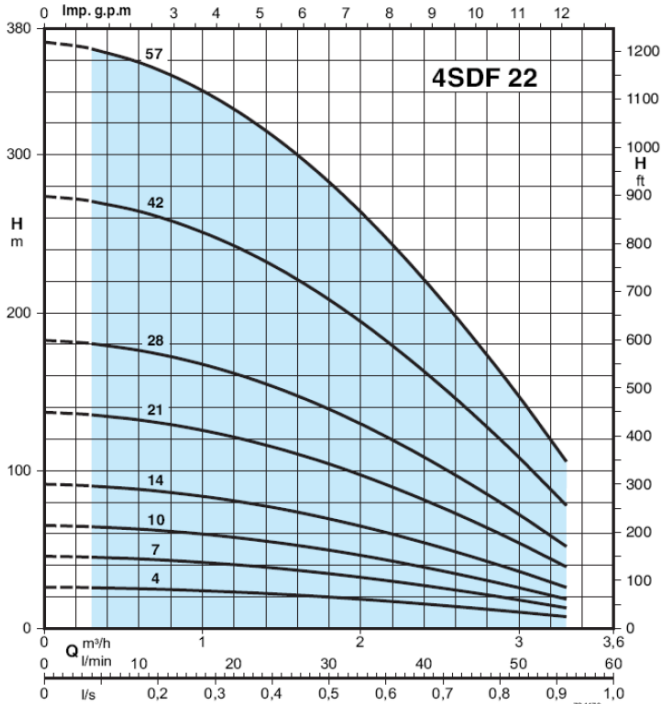

Fig.5 *Power curves of Calpeda 4SDF22/10 pump*

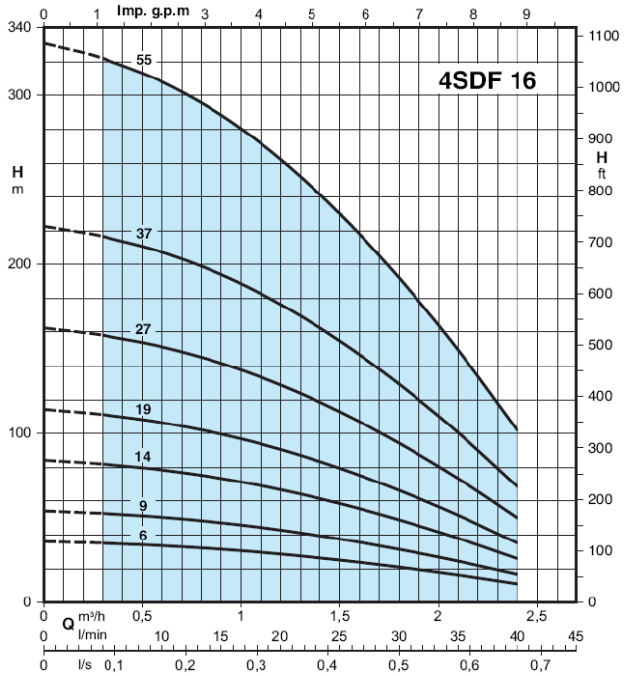

Fig.6 *Power curves of Calpeda 4SDF16/9 pump*

tion, including the heat pump. This depends on the temperature of the heating water. We will use the heat's pump output temperature T_0 (in the circulating pump (5)). The results are in Fig. 7. Blue line is the measured system power consumption with the more powerful pump 4SDF 22/10, the red line is with less power 4SDF 16/9 pump. The difference in electrical power consumption between both pumps in our system is 397 Watts, but in total power consumption (with the heat pump) it saves 350 – 380 Watts.

As we can see from Fig.7, the lowest power consumption and highest COP factor can be reached at low temperatures. Therefore we can achieve the best results with a floor heating, where the temperature T_o is up to 35 °C. In our system radiators are used and higher temperatures are necessary during cold days. To keep the temperature as low as possible, a balance must be found between the delivered output power from the heating and the thermal loss of the object. The heating water with optimal temperature circulates in

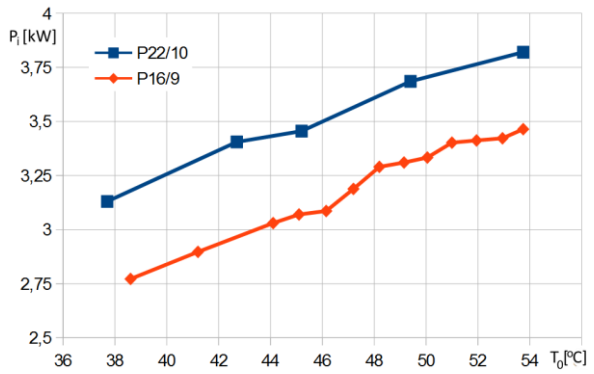

Fig.7 *Power savings after the submersible pump exchange.*

radiators, which ensures nearly the required temperature in the house. This is named eqithermal regulation [4]. A temperature sensor must be placed outside on the shadow wall at the height of 2 meters over the ground. In family houses and other objects, the room temperature may change also for reasons other than changing the outside temperature. Therefore the equithermal regulation is completed with an internal temperature sensor ((11) in Fig.3) in a reference temperature room. Such regulation is then called the equithermal regulation corrected to the reference temperature. The heat pump software heats the water in the water tank (6) according to the temperature from a equithermal curve, which was set by the user (Fig.8). The real equithermal curve refines the heat pump software, while utilizing also the observed system dynamics. The hysteresis is set to ±2.5 °C, which means the compressor switches on when the temperature of water in the water tank is 2.5 °C lower than temperature found from the equithermal curve and switches off when the temperature of water in the water tank is 2.5 °C higher than temperature found from the equithermal curve. The role of user is set the two points in Fig.8 optimally. In terms of heat pump consumption, the optimum mode is when the circulating pump (7) runs non-stop. The heat pump control software is able to increase or decrease the temperature of the heat water up to ±5 °C difference from the equithermal curve, according to room temperature measured by the space terminal, to compensate the system dynamics. The temperature in the reference room should be close to the temperature set by the user (22 °C in our case). It should not exceed 22,5 °C, else the heat pump control unit switches off the circulating pump (7). If this happens often, the heating water temperature is too high and COP factor is not optimal. The temperature in the reference room should not sink too much because of cold heating water, because the thermal comfort were disturbed.

To learn more about the COP and heating efficiency, an experiment with measurement of four temperatures (water from the source well with temperature T_S, water returning to the collection well T_C, output heating water T_O and water returning from radiators T_r) has been done. Two thermometers Extech EA, each with two calibrated contact temperature sensors, were used. The sensors were in contact

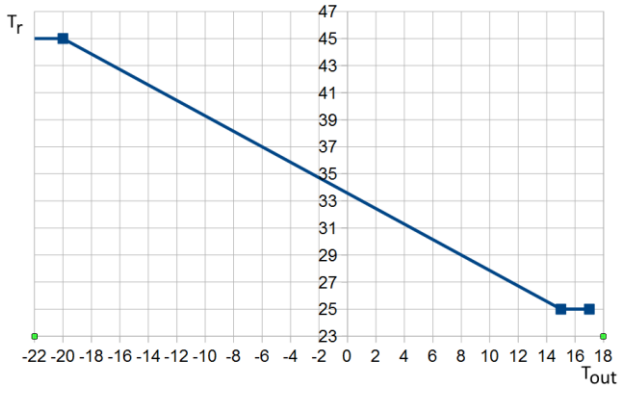

Fig. 8 *The equithermal curve – temperature of returning heating water T_r as a function of the outside temperature T_{OUT}. Both are in °C.*

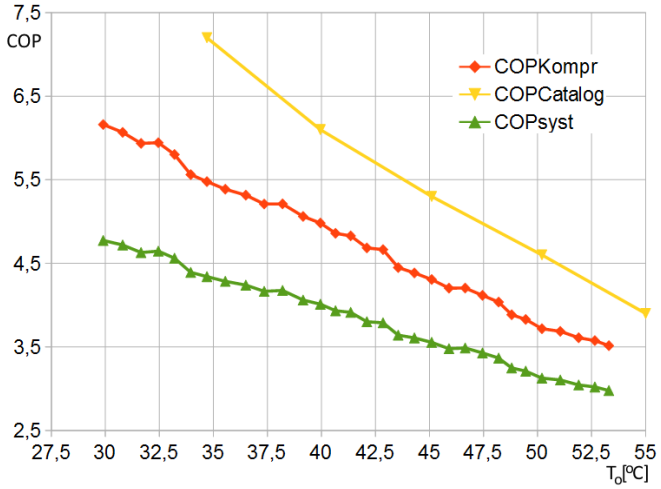

Fig. 9 *Comparison of compressor COP according to Matertherm catalogue and measurement, real system COPs (COPsyst), excluding the heating water circulating pump.*

with cupper pipes under thermal insulation. The power consumption of the heat pump system P_i (without the heating water circulating pump, which was switched off during the COP measurement), the output heating power P_o was measured, COP and COP_s were calculated. The results are in Fig. 9. Unfortunately, the measured heat pump's compressor power consumption is, according to our measurements, about 350 Watts higher than expected.

The heating water circulating pump Wilo Jonos Pico 25/6 (7) was also chosen to be effective and its power may be set by the user between 4 and 40 Watts. To optimize its behavior, two questions should be answered:

1. How much can be decreased the power of the circulating pump without significant compressor's COP decrease?
2. Is really optimal, if the circulating pump is running non-stop? Is the energy saved by better compressor COP higher than the power consumption of the circulating pump?

To answer these questions, the dependency between heating water temperature and radiated power by radiators must be known, for different powers of the circulating pump. The goal is to maximize the power radiated at given temperature of heating water, which depends on the temperature gradient between the radiator's input and output water. The temperature gradient between radiator's inflowing and outflowing water should be minimal (up to 5°C), therefore the circulating pump power should be sufficient. To measure the system cooling, water in the water tank and radiators was heated to the maximum temperature T_o=44,4°C (this is not the maximal output temperature of the heat pump. This temperature is limited by the maximal output power of the heat pump and power radiated by radiators). Then the compressor was switched off, the circulating pump (7) runs and the time dependency of the heating system cooling was measured for two different powers of the circulating pump (7) – 40 Watts (full power) and 30 Watts. The measured dependency is in Fig. 10 (blue cooling, also the heating curve was added). No significant change in radiated power was observed. The power radiated by radiators as a function of temperature is in Fig.11. We can see that there is no significant difference between both curves for 40 Watts and 30 Watts power. After some experiments the minimal acceptable power of the circulating pump (7) 22 Watts was found. The circulating pump is rather noisy at 40 and 30 Watts, the power 22 W minimized the acoustic discomfort in the house rooms. Lower power of the circulating pump leads to significant radiated power decrease, which increases required temperature of heating water and decreases heat pump's COP. Taking into account the circulating pump runs all the time during the heating season, decreasing its power from 40 to 22 Watts means up to 90 kWh annual energy sa-

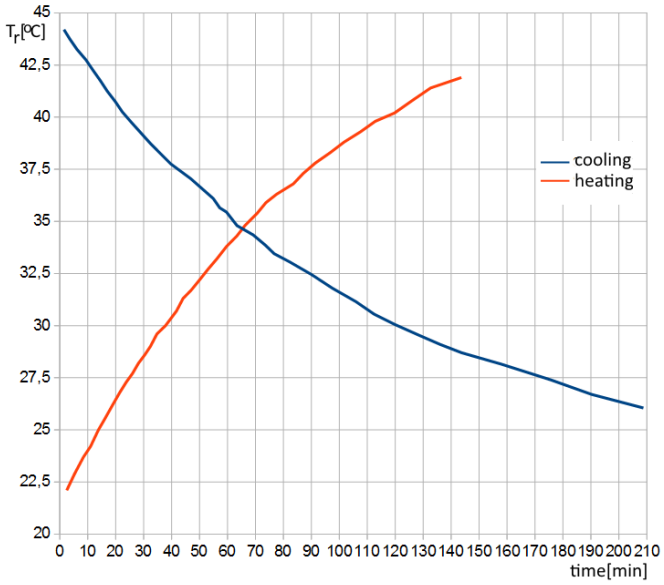

Fig.10 *Heating cooling the heating system. Circulating pump (7) is on, Compressor is off while cooling, compressor is on while heating.*

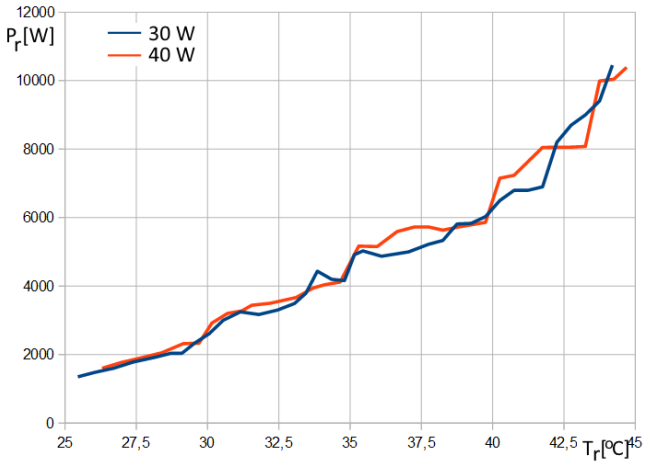

Fig.11 *Radiated power as a function of radiator's temperature for different powers of the circulating pump.*

vings.

To solve the second question, we must know the dependency of system power consumption as a function of output heating water temperature T_0 which is in Fig.12. Five degree increase of heating water means approximately 220 Watts power consumption increase, during the time the compressor is running. Five degree increase of heating water means also increase of radiated power by 1.6 factor (Fig.11). If we compare 220 Watts power consumption increase by the compressor and optimized 22 Watts of circulating pump power consumtion, switching off the circulating pump (7) brings some savings only if the compressor runs less than 10 % of time. This is at heating water temperature less than 25°C. This is too low temperature for our heating system. An impulsive mode of switching the circulating pump between the full power and zero power would bring better results (other simulation required) but this would be disturbing for acoustic discomfort and also bad for lifetime of the circulating pump. Therefore the best option for the circulating pump is to choice a high efficiency, low noise pump and optimize its power consumption for non-stop traffic. An important question for an investor is the seasonal COP_S factor ($SCOP_S$). It is defined as overall useful energy output to overall driving energy input [5]. In Table 1 are monthly temperatures for Bratislava region T_m, heating water return temperature T_r found from Fig.8, output temperature T_0 calculated as $T_0 = T_r + 4{,}7$ °C, and system COP found from Fig. 9. According to the Table 1 the $SCOP_S$ factor equals 4,32, which is not bad for a system with radiators. According

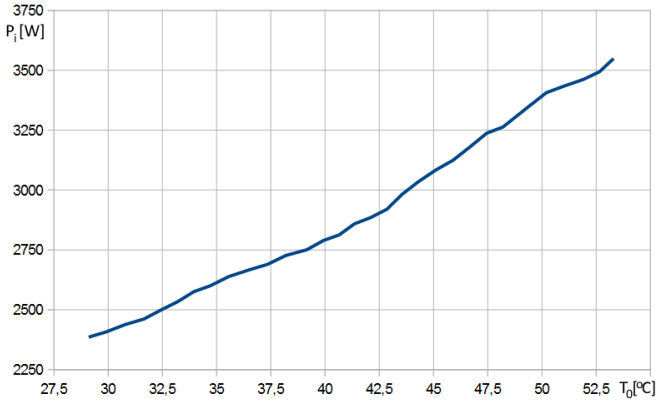

Fig.12 *The system power consumption (excluding the circulating pump (7) as a function of output heating water temperature T_0*

to Fig.2, the system brings 77 % of energy savings with comparison to a classical electrical boiler.

Table 1: *Seasonal COP for Bratislava region*

Month	Tm	Tr	To	COPs
January	-1	34,14	38,84	4,1
February	0,8	33,11	37,81	4,2
March	5,2	30,6	35,3	4,3
April	9,8	27,97	32,67	4,6
Oktober	9,9	27,91	32,61	4,65
november	3,7	31,46	36,16	4,25
december	0,4	33,34	38,04	4,15
average				4,3222

3. Conclusion

The system with a water-water heat pump was optimized. Considering the mean annual traffic of the compressor is 1200 hours, we saved 432 kWh of energy while choosing a submersible pump (2) with appropriate power. Optimizing the power of the circulating pump (7), we saved additional 90 kWh of energy. Improper installation was solved by adding a temperature sensor to the water storage tank (6), which saved 55 kWh. Additional 600 kWh a year could be saved changing the radiators heating for underfloor heating. Better results would be achieved with another heat pump with lower heating power (and bivalent system) and a lower power submersible pump. The problem is a small assortment of good quality low power submersible pumps and heat pumps. The last but not least is the possibility of looking for the reason of probably gap between the catalogue COP and the real compressor COP performance (about 420 kWh a year).

4. Literature

[1] Kim Y. J.-J., Norford L. K., Kirtley J. L., Jr.: Modeling and analysis of a variable speed heat pump for frequency regulation through direct load control. IEEE Trans. on Power Systems, Vol. 30, no. 1, 2015, .pp. 397–408

[2] Zhao, X., Long, E., Zhang Y., Liu, Q., Jin, Z., Liang, F.: Experimental Study on Heating Performance of Air - source Heat Pump with Water Tank for Thermal Energy Storage. 10th International Symposium on Heating, Ventilation and Air Conditioning, ISHVAC2017, 19-22 October 2017, Jinan, China

[3] Esen H., Esen M., Ozsolak O.: Modelling and experimental performance analysis of solar-assisted ground source heat pump system. Journal of Experimental & Theoretical Artificial Intelligence, Vol. 29:1, pp. 1-17

[4] Komínek P.: Heat Supply Optimization. Advanced Materials Research, Vol. 1041, 2014, pp. 139-145

[5] Hadom J-Ch.: Solar and Heat Pump Systems for Residential Buildings. Ernst & Sohn 2015, ISBN 978-3-433-03040-0

THE INFLUENCE OF THE TOOTH PROFILE SHAPE ON THE STRESS-STRAIN STATE IN THE GEAR

Zorko D. M.Sc., Prof. Tavčar J. PhD., Prof. Duhovnik J. PhD.
Faculty of Mechanical Engineering – University of Ljubljana, the Republic of Slovenia

damijan.zorko@lecad.fs.uni-lj.si

Abstract: *The shape of the tooth profile affects the stress-strain state in the gear. In the case of a fatigue failure the stress state is a decisive criterion for the lifetime of the gear. The shape of the tooth flank affects the magnitude of the contact pressure in the contact of the meshing teeth. The consequence of which are surface cracks and pitting. The shape of the tooth root influences the magnitude of the root stress, which, when limit is exceeded, leads to root cracks and teeth breakage. Many different types of gearing are known, but in the practice most widely used is the involute one. Other types of gearing become interesting especially when polymer materials are being used. If the gears are injection molded the type of gearing does not affect the cost of the tool. In the case of metal gears, standardized tools for involute gearing make the use of other special types of gearing economically unjustified. Our research is focused on the S-gears, which got their name from the S-shaped path of contact. The paper presents the research of how the defining parameters of S-gears impact the stress-strain state in the gear. This was done using a numerical model which simulates gear meshing. The stress state of two different types of S-gears was compared with the stress state in an involute gear of the same dimensions (same module, number of teeth and width). It was found that with a proper choice of gearing type we can improve the load bearing capability of the gear pair. With use of our numerical model we have also analyzed the impact of the tip relief on the stress state. The numerical model was validated for the case of meshing steel involute gears, where we can compare the results of the model with the results according the ISO 6336 calculation. A good match between the results of the model and results according the standard was obtained. After validation the same numerical model was used for the calculation of the stress-strain state in S-gears. This was calculated then for metal and polymer (POM/PA) gear pairs.*

Keywords: S-GEARS, POLYMER GEARS, NUMERICAL SIMULATION, STRESS-STRAIN STATE

1. Introduction

Gears are often used machine elements for the transfer of mechanical power. With the increasing supply of polymeric materials and their ever-increasing mechanical properties, the use of polymer gears increases. The reason for the growing use of polymer gears are some of the advantages when comparing them to metal gears. The most important ones are the lower mass, cheaper mass production, easier production, operation without lubrication and better dampening of the vibrations. Partially crystalline thermoplasts are mainly used for the production of polymer gears. Various reinforcing fibers can be added to these materials as well as materials that reduce wear and improve sliding properties, e.g. PTFE, MoS2 [1-4].

There is a valid international standard ISO 6336 [5] for the conversion of steel involute gears. Also, the German standard DIN 3990 [6] is often used. According to both of these standards, the conversion is divided into the calculation of the root and flank strength, as well as the calculation of thermal scuffing. There is no valid international standard yet for the conversion of polymer gears. Most commonly used is the recommendation VDI 2736 [7]. In the recommendation VDI 2736, the calculation of tooth root and flank strength is summarized and simplified according to DIN 3990. The recommendation offers a very limited set, of the necessary data for the calculation, as these are defined only for some basic engineering polymer materials. Existing calculation models apply only to involute gears. Our work will focus on the research of S-gears, which in certain conditions have better properties than the involute ones. This means a certain competitive advantage. Thus, the problem arises how to reliably dimension the polymer S-gears.

Hlebanja [8] proposed the shape of a tooth flank that defines the S-shaped path of contact and has some advantages over the involute flank profile. The main advantages are the convex/concave contact at the beginning and end of the meshing and consequently the smaller flank stresses, smaller sliding speeds, more favourable rolling/sliding ratio, and consequently less losses. The S-gears roots are wider than the involute ones at the same normal module, leading to higher root strength, and it is possible to produce gears with a much smaller number of teeth - at least 4 teeth. Hlebanja et al. [8-10] confirmed the advantages of S-gears in several studies, comparing them to the involute ones. They tested and compared the lifetime of steel involute and S-gears and analyzed the damage mechanisms. Kulovec and Duhovnik [11] analyzed the influence of individual parameters on the S-gear tooth profile shape. Duhovnik et al. [12] tested the lifespan of injection molded polymer S-gears and compared the results of the tests with polymer involute gears. They found that the S-gears are sensitive to the quality of the manufacturing, for which, in the case of injection molding, a well-controlled technological process is required. In one of our previous works we experimentally compared the lifetime of the machine cut S and involute gears. S-gears have shown a longer lifetime [13]. The aim of our work presented in this article was to use the numerical methods to study the influence of the tooth shape on the stress-strain state in the gear.

2. Methodology

Gear geometry

The S-gear profile shape depends on two parameters, namely the size factor a_p and the exponent n [8]. The stress state was calculated for two different S-gear geometries and compared to the involute one. The parameters of the analyzed geometries are given in Table 1, and the analyzed teeth geometries are shown in Fig. 1.

Table 1: *Specification of the gear parameters. *Note: For the S-gears this is the initial pressure angle at the kinematic point C. In the case of S-gears the pressure angle is variable along the path of contact.*

Parameter	involute	S-gear 1	S-gear 2
module [mm]	1	1	1
number of teeth	20	20	20
width [mm]	6	6	6
pressure angle [°]	20	18*	23*
exponent - n	/	2.05	1.3
size factor - a_p	/	1.5	1.8
reference diameter [mm]	20	20	20
tip diameter [mm]	22	22	22
root diameter [mm]	17.30	17.70	17.60
center distance [mm]	20	20	20
contact ratio	1.557	1.383	1.352

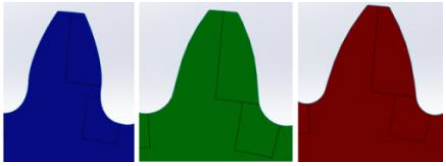

Fig. 1 *The geometry of analyzed gears: involute gear (blue), S-gear 1 (green), S-gear 2 (red)*

Numerical model

Due to the nature of the problem, the numerical model was set in 2D, taking into account the plane stress state. This reduces the use of computer resources and the calculation times are much shorter. The time it takes to solve the problem on a better desktop computer is approximately 20 minutes, which also makes it easy to use the model in practice. The advantage of the modeling in 2D is also the possibility to obtain a denser mesh in the contact area of the teeth, Fig. 2, without making solving times too long. Therefore, we expect a more accurate calculation of the flank stresses. We modeled the entire gear body and only 5 teeth, since the load is cyclically the same for each tooth. Stresses are examined on the central tooth, which passes through all the characteristic points of meshing.

In order to validate the model, in the first step we simulated the meshing of steel gears without considering the friction between the tooth flanks. This is an example that can be compared with the calculation of the stress according to ISO 6336. After the standard calculation, the maximum values of the root and flank stresses that occur during meshing are calculated. With our numerical model, we can calculate the stresses at all points of contact. According to ISO 6336, the actual root stress in the gear is calculated by the equation:

$$\sigma_F = \sigma_{F0} \cdot K_A \cdot K_V \cdot K_{F\beta} \cdot K_{F\alpha}$$

The nominal tooth root stress σ_{F0} is calculated by the equation:

$$\sigma_{F0} = Y_{Fa} \cdot Y_{Sa} \cdot Y_\varepsilon \cdot Y_\beta \cdot Y_B \cdot \frac{F_t}{b \cdot m}$$

where: Y_{Fa} is the form factor, Y_{Sa} is the stress correction factor, Y_ε is the contact ratio factor, Y_β is the helix angle factor, Y_B is the rim thickness factor, F_t is the nominal tangential force, b is the gear width and m is the normal module.

The actual tooth flank stress σ_{H0} is calculated by the equation:

$$\sigma_H = \sigma_{H0} \cdot \sqrt{K_A \cdot K_V \cdot K_{H\beta} \cdot K_{H\alpha}}$$

The nominal tooth flank stress σ_{H0} is calculated by the equation:

$$\sigma_{H0} = Z_H \cdot Z_E \cdot Z_\varepsilon \cdot Z_\beta \cdot \sqrt{\frac{F_t}{b \cdot d_1} \cdot \frac{u+1}{u}}$$

where: Z_H is the zone factor, Z_E is the elasticity factor, Z_ε is the contact ratio factor and Z_β is the spiral angle factor. The application factor K_A takes into account the overloads during the operation, the dynamic factor K_V takes into account the internal dynamic forces and factors $K_{F\beta}, K_{F\alpha}, K_{H\beta}, K_{H\alpha}$ take into account the manufacturing accuracy on the load distribution between the teeth. These effects are not considered in our numerical model, so the calculated stresses are compared with the nominal stresses σ_{F0} and σ_{H0}. According to the recommendation VDI 2736, the same equations are used to calculate the nominal root and flank stresses. The difference in the calculation of the actual stresses is that the coefficients K_A, $K_V, K_{F\beta}, K_{F\alpha}, K_{H\beta}, K_{H\alpha}$ are not defined for polymer gears, but rather it is recommended to take a factor $K_F \approx K_A$, the value of which is $1 - 1.25$.

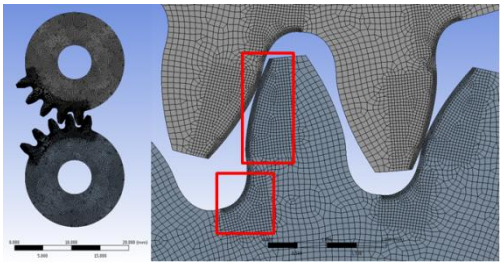

Fig. 2 *Geometry of the numerical model and presentation of the mesh density*

For all gear pairs analyzed, a load of 0.4 Nm was simulated. When a good match between the results of our numerical model and the ISO 6336 calculation was achieved, we upgraded the simulation by modeling friction in the contact between the meshing flanks. This is not taken into account by the standard ISO 6336. Steel gears are mostly lubricated with oil, so the influence of friction on the stress is also negligible. The frictional coefficient $\mu = 0.1$ was prescribed when modeling the frictional contact between the steel gears. Polymer gears often operate without additional lubrication, in which case the friction affects the stress in the gear. In order to calculate the stress state in the polymer gear, the same numerical model was used, which was previously validated in the case of steel gears. The material combination POM/PA6 was analyzed, where the drive gear was made from POM, and driven from PA6. This material combination was tested in our previous works [12, 13]. Due to the short duration of the load, the polymer material was modeled as linear elastic. The material parameters considered were: $E_{POM} = 2800$ MPa, $E_{PA6} = 3500$ MPa, $\nu_{POM} = 0.35$, $\nu_{PA6} = 0.4$. The friction coefficient $\mu = 0.28$ was prescribed for this material combination.

3. Results

Steel gear pair, frictionless contact

When simulating the meshing of the involute gear pair, the stress pattern (Fig. 3) corresponds to the theoretical stress, which is found in the literature [14]. The stress at the tooth root and on the flank appears at the initial meshing point A. When the gears are in mesh, the contact point moves towards the tip of the tooth. In point B, the single-tooth contact zone begins, where the previous pair of teeth leaves the meshing. In the area of single-tooth contact, the stresses increase rapidly, as the total load is transmitted only over one pair of teeth. The more the contact point moves towards the tip of the tooth, the longer is the lever and consequently the greater the root stress. This reaches the maximum value in the point D, which is the outer point of the single-tooth contact area of the drive gear. This appears shortly before the next pair of teeth gets into the mesh. The reversed image of the stress pattern occurs in the driven gear, where the maximum value of the root stress appears in point B. On Fig. 3 all the characteristic meshing points are indicated by the dotted lines for individual gear geometries. The stress pattern for both S-gear shapes is similar to the involute one, except that both S-gear geometries have a wider area of single-tooth contact as a result of a smaller contact ratio. The minimum root stress is calculated in the gear S2, which has the widest root, slightly higher is the root stress in the involute gear and the highest in the gear S1, where the calculated stress is higher in spite of the broader root. The higher stress in the gear S1 occurs due to the wider area of single-tooth contact, where the distance from the point D to the root is larger than in the involute one. This means a greater bending moment of the tooth and, consequently, higher stress at the tooth root. The gear S1 also has a smaller rounding radius in the root, which is also the reason for higher root stress.

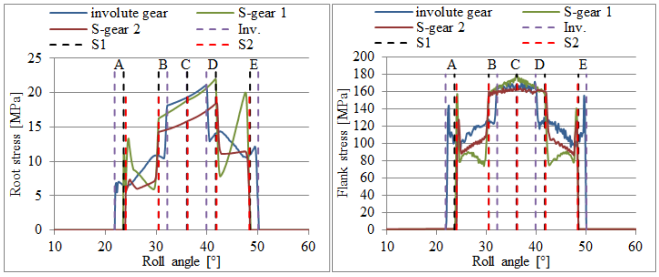

Fig. 3 *Root stress (left) and flank stress (right) in the driver gear*

If we look at the flank stresses, we see that stress peaks occur at the beginning and at the end of the meshing. These peaks occur due to the narrow contact area, where the tooth tip is pressed against the flank of the other tooth. The flank stresses are similar to theoretical ones, with the difference in the stress peaks at the beginning and

end of the meshing, resulting from the transfer of force through the narrow contact area. We can see that the flank stresses in the two S-gear geometries in the A-B and D-E range are smaller. In the single-tooth contact area B-D the flank stresses in all three analyzed geometries are approximately the same.

Polymer gear pair, frictionless contact

The stress pattern is different for the polymer gears comparing them to the steel gears, Fig. 4. Due to the small elastic module, the same load will result in a significantly greater deformation of the teeth. This results in an increase of the contact ratio, which results in the narrower single-tooth contact zone. The maximum root stress in the drive gear appears in the point D and in the driven gear in point B. The calculated root stresses are practically unchanged between the polymer and steel gear pairs, as the gear pair in both simulations was loaded with the same moment load.

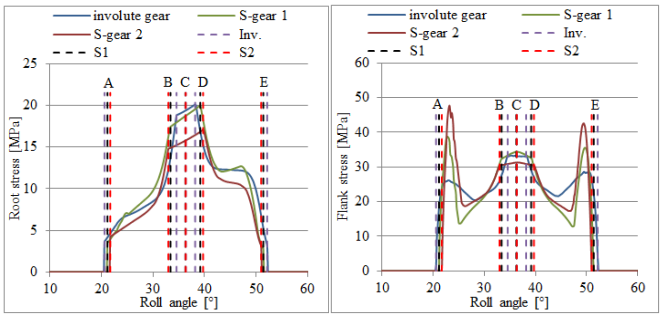

Fig. 4 *Root stress (left) and flank stress (right) in the driver gear*

Large differences can be observed when looking at the flank stresses, where these calculated for polymer gear pairs are much smaller. The elastic modulus of the material has an effect on the magnitude of the flank stress. In the standard calculation this effect is taken into account by the coefficient of elasticity Z_E. The flank stress peaks that occur at the start and end of the meshing are also present in the polymer gears.

Steel gear pair, frictional contact

In the following step, the numerical model was upgraded, taking into account the friction between the meshing flanks. The results obtained with this model are shown in Fig. 5. If the friction is taken into account, the stress pattern is similar, only in the kinematic point C there is a jump in the stress. This is due to the change in the direction of sliding, consequently the frictional force reverses the sign. Due to the wider tooth root in the S2 gear, the root stress was expected to be smaller. In the gear S1 with a similar profile to the involute gear, the root stress was even slightly larger. Even for the flank stresses, a smaller leap in the stress at the kinematic point C is observed.

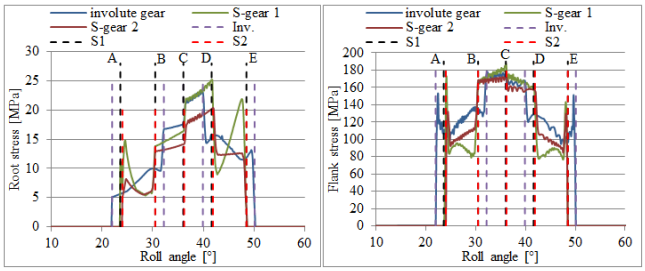

Fig. 5 *Root stress (left) and flank stress (right) in the driver gear*

Polymer gear pair, frictional contact

In the last step, the same numerical model was used to calculate the stresses in the polymer gears. The stresses, both the root and the flank ones, differ considerably from those of the steel gear pairs, Fig. 6. The reason is in the much smaller elastic modulus of the polymer gears, which leads to a greater deformation of the teeth. A rather large difference in the pattern of root stress also occurs in comparison with a frictionless model. The calculated root stress here is a bit larger, the maximum occurs in point D in both the drive and the driven gear.

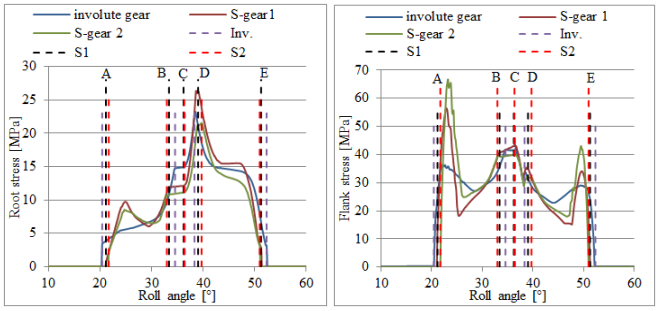

Fig. 6 *Root stress (let) and flank stress (right) in the driver gear*

In the case of flank stresses, the initial peaks are considerably higher for S-gears. This could most likely be avoided with a greater rounding of the tooth tip, which will be analyzed in the future. The teeth of the S-gears are also less deformable than involute, so no adaption is given which leads to a greater force at the stroke.

4. Discussion

Stresses calculated with the numerical models were compared with those analytically determined according the standard or recommendation. Comparison of the root and flank stresses in the steel gears is shown in Fig. 7. With the numerical model obtained maximum root stresses correlate well with the stresses calculated according to the standard. With the model that simulates a frictional contact between the meshing flanks, the calculated root stresses are approximately 8.5% larger, while in the frictionless model they are 2% smaller, comparing to the standard calculation. A big difference occurs when comparing the flank stresses. Here, it turns out that our model does not calculate the flank stress sufficiently precisely. In the case of steel gears, the contact area is very narrow, so there was a lack of elements in the contact area in spite of the very dense mesh. With further mesh refinement in the contact area, we managed to reduce the deviations to 7.5%.

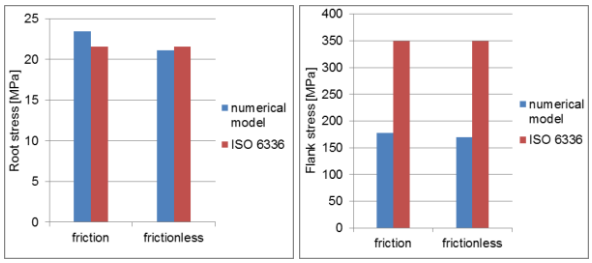

Fig. 7 *Comparison of the stresses calculated with our numerical model and according the standard ISO 6336*

Comparison of the root and flank stresses in polymer gears is shown in Fig. 8. In the case of polymer gear pairs, both the root and the flank stresses have a good match with the calculation according to VDI 2736. Based on this, we claim that our numerical model is also good for calculating the stress state in S-gears. Results obtained with the numerical model, which models a frictional contact, deviated by 2% from the calculation according to VDI 2736 in the case of root stress and in the case of flank stress by 3.6%, Fig. 8.

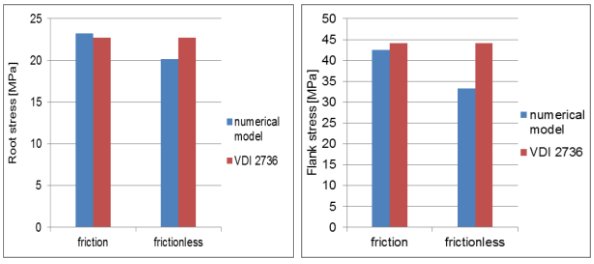

Fig. 8 *Comparison of the stresses calculated with our numerical model and according the recommendation VDI 2736*

When calculating the flank stresses with our numerical model, the stress peaks that occurred at the beginning and end of the meshing were observed. These peaks are ignored by the standard calculation. In practice, these peaks can be avoided by correcting the tooth profile, adding tip relief. This is reflected by improved meshing, leading to an extension of the lifetime of the flank and a reduction in noise during the operation of the gears. For the analysis of the effect of the profile correction, three different examples were examined. These were: a gear pair without any flank modification, a gear pair with the tip rounding of R = 0.05 mm and a gear pair with tip relief (Ca = 0.015 mm to the diameter of the outer point of single-tooth contact) and tip rounding of R = 0.05 mm. When adding the tip rounding, the results are much better, Fig. 9. The stress peaks at the start and end of the meshing are in this case smaller than the flank stress at the kinematic point C. When adding a tip relief, it is necessary to pay attention to the diameter to which it will go. In our example, the relief ran to the diameter where the single-engagement point B is located on the driven gear and point D on the drive gear. Due to the large teeth deformation of the polymer gears, we expected this correction to be appropriate. It turned out that when there is a tip relief the flank stress peaks are completely avoided, Fig. 9.

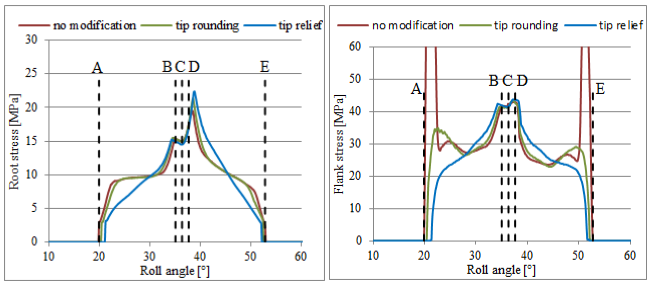

Fig. 9 *The impact of the tip relief on the root stress (left) and flank stress (right)*

5. Conclusion

From the calculated stresses we can see the difference between the involute and S-gears. The stresses in the S-gears are also affected by tooth geometry, as this can be quite different, depending on the choice of parameters n and a_p. By using a suitable S-gear shape, we get smaller stresses in the material when transferring the same load. Thus, with the S-gear pair, we can transmit heavier loads without exceeding the permissible stresses; the gear unit may be smaller. By changing the parameters n and a_p, we obtain a considerable number of different shapes of S-gears with different characteristics. In future research, we intend to analyze and set up a computational model for dimensioning of the S-gears.

Differences in the results between the frictional and frictionless models were observed. A jump in the tooth root stress was observed at the kinematic point C when modeling a frictional contact. In the case of polymer gears, no jump occurs, but the maximum stress of both the drive and the driven gear is calculated at the point D. The calculated root stresses are 25% higher when the friction is considered for polymer gears and 12% higher for steel gears. The calculated flank stresses in the kinematic point C are 27% higher in the case of frictional contact for polymer gears and 5% higher for steel gears.

In the case of polymer involute gears, the deviation between results obtained with our numerical models and those according the recommendation VDI 2736 is minimal. Thus, our assumption is that our numerical model can accurately calculate the nominal stresses also for polymer S-gears. In the recommendation, for the calculation of the actual stress, the nominal stress is multiplied by the factor of application K_A, whose recommended values are from 1 to 1.25. In the case of dimensioning of S-gears, the same value of the application factor should be used.

In the case of steel gears, the deviation between the numerical models and the calculation according to ISO 6336 is slightly larger. The calculation of the tooth root stress is still acceptable, but an excessive deviation occurs in the calculation of flank stress. We checked for the mesh density that would be needed to reduce the deviation between the flank stresses. When the mesh on the flank was refined for three times, the deviation of the flank stress was 7.5%.

With the use of a numerical model, we have proved that with a proper tip relief we can avoid the stress peaks at the beginning and end of the meshing. From practice we have experience that this has a beneficial effect on the lifetime and the noise of the gears.

6. References

[1] Crippa, C. , P. Davoli, Comparative fatigue resistance of fiber reinforced nylon 6 gears, Journal of Mechanical Design 117, 1995, 193 – 198.

[2] Goel, A. , K.K. Chawla, U.K. Vaidya, N. Chawla, M. Koopman, Characterization of fatigue behaviour of long fiber reinforced thermoplastic (LFT) composites, Materials Characterization, 60, 2009, 537 – 544.

[3] A. Bernasconi, P. Davoli, A. Basile, A. Filippi: Effect of fibre orientation on the fatigue behaviour of a short glass fibre reinforced polyamide 6, International Journal of Fatigue 29 (2007) 199 – 208.

[4] Senthilvelan, S. , R. Gnanamoorthy, Selective carbon fiber reinforced nylon 66 spur gears, Development and performance, Applied Composite Materials, 13, 2006, 43 – 56.

[5] ISO 6336: Calculation of load capacity of spur and helical gears, Parts 1-6, International standard, 2006.

[6] DIN 3990: Calculation of load capacity of cylindrical gears, German National Standard, Berlin, 1987.

[7] VDI 2736: Blatt 2, Thermoplastische Zahnräder, Stirngetriebe, Tragfähigkeitsberechnung, VDI Richtlinien, VDI-Verlag GmbH, Duesseldorf, 2014.

[8] Hlebanja J. , G. Hlebanja, Constructive Measures to increase the load-carrying capacity of gears: The characteristics of S-gears, Machine Design, 1, 2008, 33-42.

[9] Hlebanja G. , Specially shaped spur gears: A step towards use in miniature mechatronic applications, Balkan Journal of Mechanical Transmissions, 1, 2001, 25-31.

[10] Hlebanja G., S. Kulovec, J. Hlebanja, J. Duhovnik, S-gears made of polymers, Ventil, 20, 2014, 358-366.

[11] Kulovec, S. , J. Duhovnik, Variation of S-gear shape and the influence of the main parameters, in: Proceedings of the International Conference on Gears 2013, 2013, 1535-1541.

[12] Duhovnik, J. , D. Zorko, L. Sedej, The effect of teeth shape on polymer gears performance, Technical Gazette, 23, 2016, 199-207.

[13] Zorko, D. , S. Kulovec, J. Tavčar, J. Duhovnik: Different teeth profile shapes of polymer gears and comparison of their performance, in: Proceedins of MPT2017-Kyoto, Kyoto, 2017.

[14] Linke, H. Stirnradverzahnung: Berechnung, Werkstoffe, Fertigung, Carl Hanser Verlag, Műnchen, 2010.

ANALYTICAL AND FINITE ELEMENT IN-PLANE VIBRATION ANALYSIS OF A GANTRY CRANE

M.Sc. Şahin T.[1], M.Sc. Candaş A.[2], Prof. İmrak C.E. PhD.[2]
Istanbul Technical University, Graduate School of Science Engineering and Technology, Turkey[1]
Istanbul Technical University, Faculty of Mechanical Engineering, Turkey[2]

candas@itu.edu.tr

Abstract: *Every object in nature has an infinite number of vibration frequency and amplitude as called "Natural Vibration Frequency". Developing computer capacities allow calculating of natural frequencies and shapes of complex structures more accurate and understandable. In this study, a dual-trolley (2x400 tons) heavy-duty overhead gantry crane that can carry loads up to 800 tons was analysed by mathematical and finite element methods. The mathematical method is based on Euler-Bernoulli transverse vibration approach. On the other hand, finite element method is one of the most common numerical methods that can solve many engineering problems in a range from solid mechanics to acoustic. The generated solid model was analysed by the finite element method with the help of ANSYS Workbench 14.5 which is a commonly used analysis program. The obtained values of natural frequencies at mathematical calculations and finite element analysis were compared and presented.*

Keywords: GANTRY CRANE, EULER-BERNOULLI TRANSVERSE VIBRATION, VIBRATION ANALYSIS, FINITE ELEMENT ANALYSIS

1. Introduction

The cause of environmental impact and other reasons, vibration is a problem in gantry crane constructions. Vibrations can lead to serious consequences, sometimes leading up to the collapse of a crane. Concepts of "Natural Frequency" and "Resonance" should be examined firstly when determination of mentioned vibrations. The calculation of "Natural Vibration Frequencies" and to know the amplitudes of them are essential in solving of the vibration-induced engineering problems. Natural frequency is a frequency which depends on mass and flexibility of a structure and if it is induced at that frequency, it will vibrate continuously at high amplitude. If an object is excited by a frequency coincides with the natural frequency of that object, a resonance occurs and it vibrates structure excessively. Different methods can be used to avoid the resonance problem during the design of structures. Analytical approaches for non-complex system makes it easy such as verifying by numerical methods for detecting errors in the calculations and preventing the problems that may be encountered. Although analytical calculations can be made, for calculating of complex shapes numerical methods should be applied, such as finite element method [1].

In this study a dual-trolley, 2×400 tons, heavy duty overhead gantry crane (Fig. 1) that can carry loads up to 800 tons was analyzed by mathematical and finite element methods.

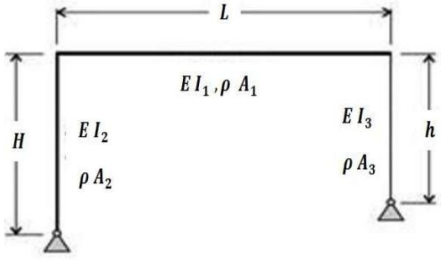

Fig. 1*Vibration model of the crane*

In this figure, dimensions and other parameters are L = 103.85 m; H = h =74.27 m; A_1 = 1.04 m^2; I_1 = 2.078 m^4; ρ = 7850 kg/m^3; E=210 GPa and the relation of this parameters with unknown parameters for α=0,332; β=75,643; ξ=0,8846; η=1,1663 are;

$$s = \frac{H}{L}\ , p = \frac{h}{L}\ , \alpha = \frac{I_1}{I_2}\ , \beta = \frac{I_1}{I_3}, \xi = \sqrt[4]{\alpha\ \frac{A_2}{A_1}}\ ,\ \eta = \sqrt[4]{\beta\ \frac{A_3}{A_1}}$$

The more precise dynamical analysis of engineering structure is based on the assumption that a structure has distributed masses. In this case, the structure has infinite number degrees of freedom and mathematical model is presented with a partial differential equation. Additional assumptions allow construction of the different mathematical models of transversal vibration of the beam. The simplest mathematical models consider a plane vibration of a uniform beam with, taking into account only, bending moments; shear and inertia of rotation of the cross sections are neglected. The beam upon these assumptions is called as Bernoulli-Euler beam.

2. Mathematical Modelling

The mathematical method is based on Euler-Bernoulli transverse vibration approach [2]. Early researchers recognized that that the bending effect is the single most important factor in a transversely vibrating beam. The Euler Bernoulli model includes the strain energy due to the bending and the kinetic energy due to the lateral displacement. The Euler-Bernoulli model dates back to the 18th century. Jacob Bernoulli (1654-1705) first discovered that the curvature of an elastic beam at any point is proportional to the bending moment at that point. Daniel Bernoulli (1700-1782), nephew of Jacob Bernoulli formulated the differential equation of motion of a vibrating beam. Later, Jacob Bernoulli's theory was accepted by Leonhard Euler (1707-1783) in his investigation of the shape of elastic beams under various loading conditions. Many advances on the elastic curves were made by Euler. The Euler-Bernoulli beam theory, sometimes called the classical beam theory, Euler beam theory, Bernoulli beam theory, or Bernoulli-Euler beam theory, is the most commonly used because it is simple and provides reasonable engineering approximations for many problems. The differential equation of a uniform beam [2]:

$$EI\frac{d^4y}{dx^4} = q$$

The elastic modulus is *E*; the moment of inertia is *I*, the transverse load that applied on a unit length of the beam is *q*. The load that applied on a unit length in case of free vibration:

$$q = -\rho A\frac{d^2y}{dt^2}$$

Here, *ρ* is density of the material and *A* is the sectional area. The mathematical model of plane vibration of Euler-Bernoulli Beam when the beam is under a force *f(x,t)*.

$$EI\frac{d^4y}{dx^4} + \rho A\frac{d^2y}{dt^2} = f(x,t)$$

Here, *y(x,t)* is the lateral displacement and *x* and *t* are x-axis and time respectively. The initial and boundary conditions are:

$$y(x,0) = u(x);\ \frac{dy}{dx}(x,0) = v(x)$$

The lateral displacement of the beam when t = 0 is *u(x)* and the first derivative of the displacement is *v(x)*. However, the Euler Bernoulli model tends to slightly overestimate the natural frequencies. The procedure of determining Eigen frequencies at complex systems (systems with large number of the freedom

degrees) is the most crucial phase of dynamic analysis. Accurate determination of Eigen frequencies was limited to the simple supporting structure (simple beam and console). Finding out solutions of frequent equation for complex elastic bodies is very difficult, because it contained the trigonometric and hyperbolic functions. Mathematica software enables routine solving of frequency equations for complex elastic bodies oscillation.

3. Finite Element Analysis

By Finite Element Method (FEM), structural analyzes can be made rapidly, reliably and nondestructively. Its popularity comes from his realistic results which were taken from the comparisons between FEM and analytical approaches. A variety of specializations such as mechanical, aeronautical, biomechanical engineering commonly use integrated finite element method in design and development of their products. As finite element method software, ANSYS helps tremendously in visualization of stiffness and strength and also in minimizing weight, materials, and costs. In this study, ANSYS is used to determine the natural frequencies with modal analysis. In analysis, 260991 meshed elements and 666104 nodes were used. Finite element method allows entire designs to be constructed, refined, and optimized before the design is manufactured.

4. Results

The maximum displacements in different mods are shown in Figure 2. The natural frequencies and relative error between mathematical and finite element analysis are shown in Table 2. The maximum difference is 7.02%. In modal analysis of a crane, the reliable results can be obtained by using of finite element analysis. It can be used in the design stage of a crane to avoid the resonance situations.

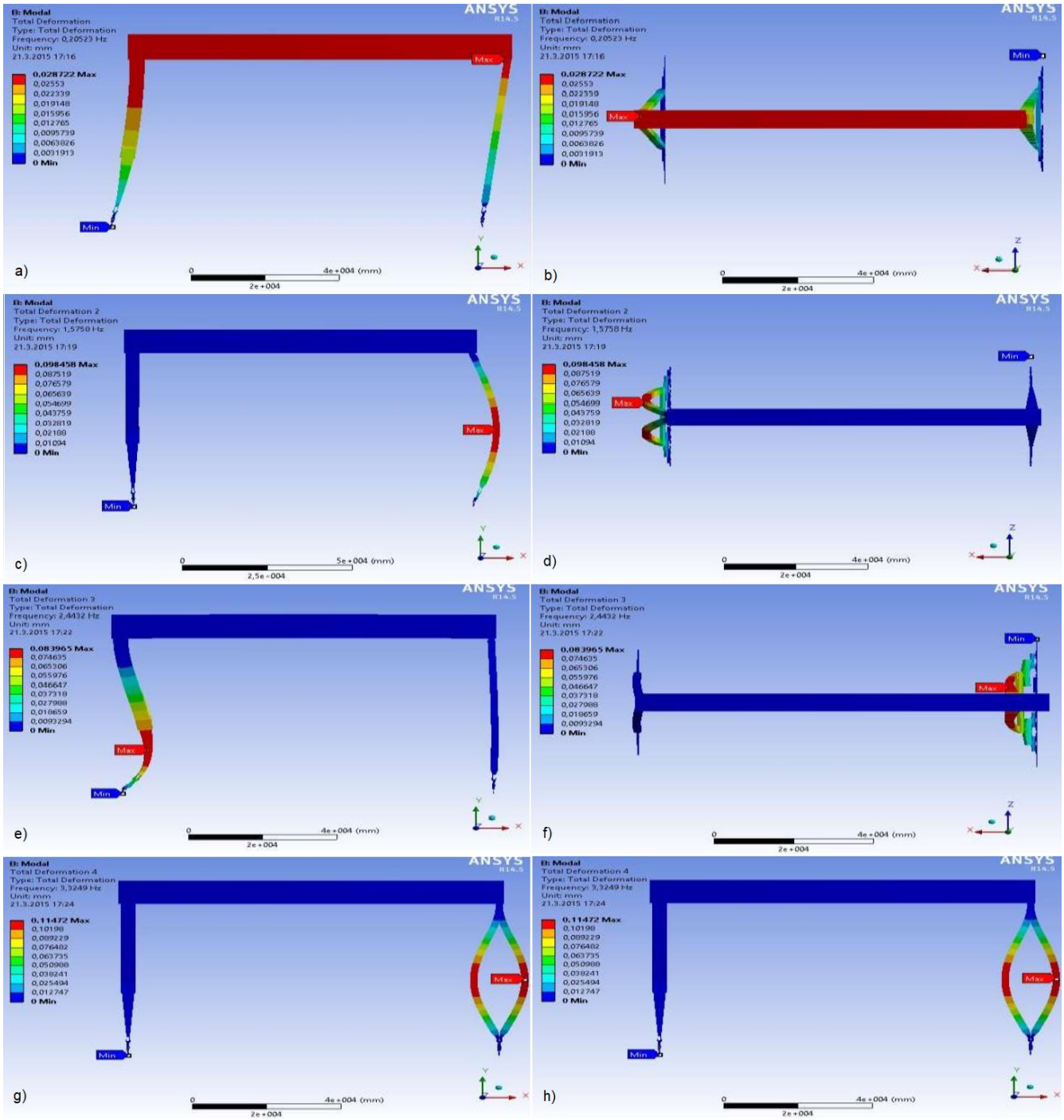

Fig. 2 *Maximum Displacements in Different Mods: a, b) Front and Top View in Mod 1; c, d) Front and Top View in Mod 2; e, f) Front and Top View in Mod 3; g, h) Front and Top View in Mod 4.*

Table 1: *Comparison of Mathematical and Finite Element Analysis Natural Frequencies [Hz]*

Mod	Natural Frequency [Hz] Mathematical Analysis	Natural Frequency [Hz] Finite Element Analysis	% Relative Error
1	0.1908	0.2052	7.02
2	1.4526	1.5758	7.81
3	2.3861	2.4432	2.33
4	3.3048	3.3249	0.60

5. Conclusion

In the first chapter, historical development of cranes and crane types are introduced primarily. Then, according to Euler-Bernoulli transverse vibration approach, the applied method for the creation of the mathematical model of the in-plane vibration of a gantry crane is introduced. For the mathematical model, the differential equations are prepared by using Fourier and Krylov-Duncan Methods. By the methods Fourier and Krylov-Duncan, the differential equation of the transverse vibration of the uniform Bernoulli-Euler beam changed to uncoupled ordinary differential equations with respect to unknown functions which are depend on coordinate and time. Eigen functions and eigenvalues, the natural frequencies of this crane was obtained. In the same section, the modal analysis of the crane made by using finite element method and natural frequencies are obtained. Before running the program, the general settings of modal analysis were prepared. Most important parts of the settings are, entering the engineering data, sizing and the tolerance value. After the settings, meshing was generated.

In the next section, the finite element method and the modal analysis has described. In order to apply this method to the problem, firstly, all parts creating the crane were 3-D modeled by using the SOLIDWORKS drawing program.3-D modeled parts were assembled by using the same drawing program. All 3-D models were created with the help of the draft drawings which were formed by mechanical calculations and the selection of the structural elements. The generated solid model was analyzed by the finite element method with the help of ANSYS Workbench 14.5. Mesh quality is the most important factor that affects the finite element results. Increasing mesh quality increases the accuracy of the finite element method. Although minimizing size of the meshes can be an effective method to increase mesh quality, the solving capacity of the computers limit us. Then, the boundary conditions were applied. It was applied by fix support and displacement commands.

In the last section, the obtained values of natural frequencies at previous section are compared and the results of comparison are presented.

5. References

[1] Akgün G. (2013) Design and analysis with numerical method of 2x400 ton gantry crane, MSc Thesis, ITU Graduate School of Science, Engineering and Technology, Istanbul Technical University, Turkey.

[2] Karnovsky İ.A. ve Lebed O. (2009) Advance Method of Structural Analysis, Springer, New York, USA.

INCREASE OF REALIBILITY OF OPTIC-ELECTRONIC DEVICES BY MEANS OF FINISHING ELECTRON-BEAM PROCESSING OF THEIR OPTICAL ELEMENTS

ПІДВИЩЕННЯ НАДІЙНОСТІ ОПТИКО-ЕЛЕКТРОННИХ ПРИЛАДІВ ШЛЯХОМ ФІНІШНОЇ ЕЛЕКТРОННОПРОМЕНЕВОЇ ОБРОБКИ ЇХ ОПТИЧНИХ ЕЛЕМЕНТІВ

D. Eng. Sc Yatsenko I. V[1]., d. Eng. Sc., Professor Antonyuk V. C.[2], d. Eng. Sc. Gordienko V. I.[3] ,
d. Eng. Sc Kyrychenko O. V.[4] , d. Eng. Sc. , Professor Vashchenko V. A [1]
Cherkasy State Technological University[1] , Ukraine; National Technical University of Ukraine " Kiev Polytechnic Institute name of Igor Sikorsky"[2], Ukraine; State Enterprise Scientific and Production complex "Photoprylad"[3], Ukraine; Cherkassy Institute of Fire Safety named after Heroes of Chornobyl[4] , Ukraine
E-mail: irina.yatsenko.79@ukr.net

Summary: *The range of parameters of the electron beam (density of thermal effect $F_n = 7 \cdot 10^6 \ldots 8 \cdot 10^8$ W/m² and travel speeds $V = 5 \cdot 10^{-3} \ldots 5 \cdot 10^{-2}$ m/s), within which there is an improvement in the performance characteristics of optical elements: increase of microhardness of the surface of elements from optical ceramics from $1{,}21 \cdot 10^3 \ldots 2{,}83 \cdot 10^3$ MPa to $4{,}84 \cdot 10^3 \ldots 7{,}15 \cdot 10^3$ MPa and increase of the spectral transmission coefficient of IR-radiation by 4... 6% for elements of optical glass and for 5... 7% – for elements of optical ceramics; there occurs an increase in the critical values of the external heat flow leading to the destruction of the elements by 1,5…2 times, thus the increase of external pressure up to 10^7 Pa decreases the specified critical values by 1,3…1,5 times; critical values of thermoelastic stresses in optical elements at heating temperatures 300... 1200 K increase by 1,5…2,5 times, indicating an increase in resistance to thermal effects and increased external pressures of optical elements processed by an electronic beam; the values of critical heights of falling of a steel ball on their surface, leading to destruction of elements, increase from 0,18…1,1 m to 0,37…1,35 m, so, their resistance to mechanical shocks increases. It is established, that increase of durability of optical elements, processed by an electron beam, to external thermal and mechanical effects leads to the increase of probability of non-failure operation of optic-electronic devices under extreme conditions of operation to 10... 20%.*

KEY WORDS: OPTO-ELECTRONIC INSTRUMENT MAKING, ELECTRON BEAM, OPTICAL GLASS AND CERAMICS, RELAIBILITY

1. Introduction

Modern optic-electronic devices with elements from optical glasses (K8, BK10, TF10, etc.) and ceramics (KO1, KO3, KO5, etc.) (laser rangefinders of sighting complexes, input windows of IR-visibility, optical fairings of IR devices of homing and tracking, etc.) are subjected to intense external effects under conditions of operation (elevated heating temperatures, external pressures, shock effects under the conditions of shot and flight [1 – 4]).

Under the specified conditions the properties of surface layers of optical elements are changed up to their destruction (appearance of cracks and chips, change of geometrical form and other defects), that leads to a significant deterioration of technical and operational characteristics of the devices and to their failure. That's why, the essential importance lies in the prevention of forced destructions of optical elements of devices under the conditions of their operation, taking into account the influence of external effects.

As the experimental researches of various authors have shown [5 – 11], for the prevention of optical elements destructions, of practical importance are electron-beam methods of finishing of their working surfaces at the manufacturing stage, that allow to improve properties of surface layers of elements and, thus, to make them more resistant to external influences, improving basic technical and operational characteristics of devices (reliability, service life, etc.). However, the patterns of electron beam effect onto the change in the properties of surface layers of elements of optical glass and ceramics are currently not investigated enough.

Therefore, the purpose of the given work lies in the prevention of destructions of optical elements of devices by improvement of properties of surface layers of elements and increase of their resistance to external effects by means of preliminary electron-beam processing .

2. Results and discussion

As a result of the conducted experimental researches for the first time the regularities of influence of electron-beam technology modes (density of thermal effect of the beam F_n and moving speed V) on optical elements are established.

It is obtained that after the standard machining the most characteristic is the presence of microdefects – cracks in depth up to 0,1…0,7 μm, with length up to 2... 5 μm, as well as bubbles with the size of $10^{-3} \ldots 10^{-2}$ μm. After electron-beam processing the sizes of bubbles (diameters) on the surface of elements decrease by 2... 4 times, thus other microdefects smaller than 1... 2 μm are not observed, so as a result of processing by an electron beam of the elements surface as though becomes "cleaned", small defects are eliminated. Thus, at an increase of F_n from $7 \cdot 10^6$ W/m^2 to $7 \cdot 10^7$ W/m^2 the area of these defects decreases by 1,8…2,7 times. The study of the topology of the elements surfaces before and after electron-beam processing shows that in the first case the value of microroughness is 30... 40 nm, and in the second case decreases up to the level of 0,5...1,2 nm.

Detailed studies of the surface structure of elements from optical glass by AFM methods allowed to determine the following effects of modes of electron-beam technology on the size of microroughness: increase of F_n from $7 \cdot 10^6$ W/m^2 to $7 \cdot 10^8$ W/m^2 and reduction of V from $3 \cdot 10^{-2}$ m/s to $5 \cdot 10^{-3}$ m/s leads to a decrease in the size of microroughness from 5... 6 nm to 0,7…1,2 nm (Fig. 1 – 3).

The study of the structure of surface layers of elements from optical glass before and after electron-beam processing showed that the maximum depth of major thermal action zone or the thickness of the melted layer of h_m essentially depends on the F_n and V (Fig. 4 – 6) and can reach the values of 300... 350 μm, which exceeds the maximum allowed values h_m^* = 100…150 μm with some critical values F_{ni}^* and V_{ni}^* (i = 1, 2,…), which leads to the formation of influxes and wave areas on the surface of the elements, resulting in violated flatness and, finally, geometric form.

It is established that the layers on the surface of the elements of optical glass modified by electron beam have to different extent changed chemical composition. So, the analysis of change of elemental structure of layers in thickness of 10... 20 μm on the surface of the elements of the optical glass K8 showed the decrease in the concentration of Na and O, the increase of concentration of Si and the inalterability of K concentration. At the same time, through the example of raw and processed by electron beam elements of

optical glass BK10, it is shown that there is no noticeable quantitative change in the chemical composition of the layers on their surface, but it is possible to conclude that the homogeneity of the elements distribution improves in the microvolumes of the surface layer after the electron-beam processing.

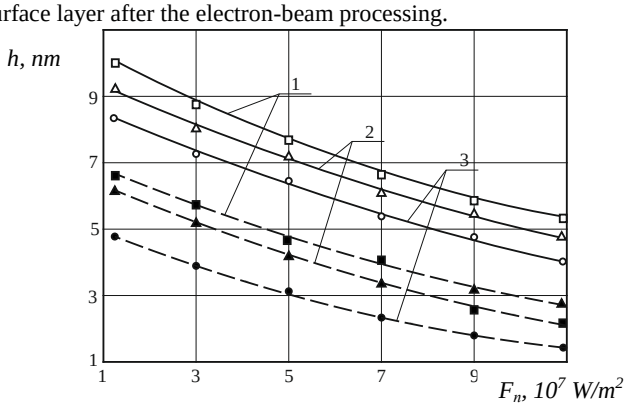

Fig. 1. *Dependence of the value of surface microroughness of the elements from the optical glass BK10 (1), K8 (2) and TF10 (3) on the density of the thermal effect of the electron beam: ——— –speed of the electron beam movement $V = 3 \cdot 10^{-2}$ m/s; – – – – speed of electronic beam movement $V = 5 \cdot 10^{-3}$m/s; Δ, ○, □, ▲, ●, ■ – experimental data.*

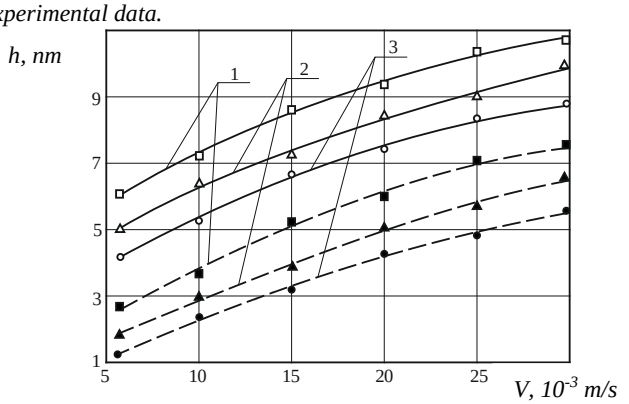

Fig. 2. *Dependence of the value of the surface microroughness of the elements from the optical glass K8 (1), K8 (2) and TF10 (3) on the speed of the electron beam:——— – the density of the thermal effect of the electron beam $F_n = 5 \cdot 10^8$ W/m^2; – – – – density of thermal effect of the electron beam $F_n = 7 \cdot 10^6$ W/m^2; Δ, ○, □, ▲, ●, ■ – experimental data.*

It is also established that electron-beam processing of elements from optical glass by flowing leads not only to the homogenization of layers, but also to the orientation adjustment near the surface of the silicon-oxygen glass grid, which is approaching to the structure of quartz glass. This is mainly due to the removal of K ions, as well as other elements-modifiers at simultaneous effects of high temperatures on the surface (up to 1200... 1300 K), that leads to increased stability of the optical elements to the external thermal and mechanical effects.

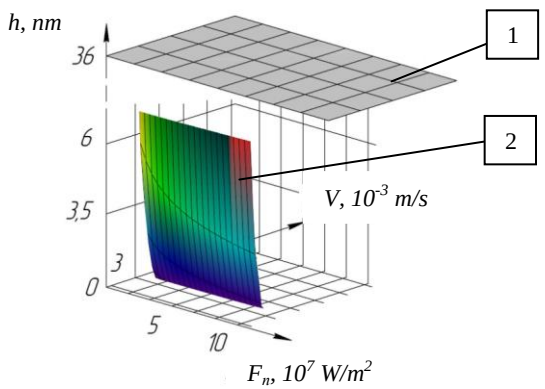

a)

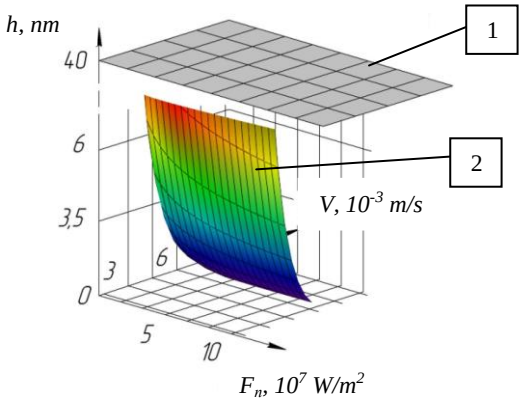

b)

Fig. 3. *Dependencies $h(F_n, V)$ for elements of optical glass TF10 (a) and BK10 (b): 1 – elements unprocessed by an electronic beam; 2 – elements processed by an electronic beam.*

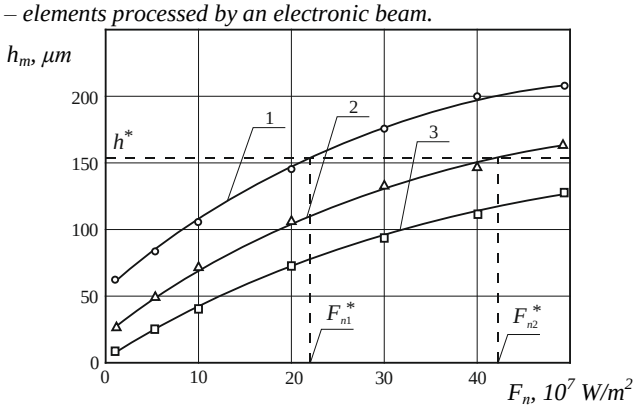

Fig. 4. *Dependence of thickness of melted layer h_m in elements from optical glass K8 on density of thermal effect of electron beam for different V: 1 – $V = 5 \cdot 10^{-3}$ m/s; 2 – $V = 9 \cdot 10^{-3}$ m/s; 3 – $V = 3 \cdot 10^{-2}$ m/s; Δ, ○, □ – experimental data.*

As a result of the conducted studies, it was shown that regardless of the nature of ceramics (KO1, KO2, KO5) in the surface layers of the elements processed by the electron beam, with an increase of F_n up to $1{,}5 \cdot 10^7$ W/m^2 and V to $2 \cdot 10^{-2}$ m/s noticeable phase changes are not observed, but there is an increase in mosaic blocks by 3,1…7,8 times and reduction of microdeformations in crystal grid by 1,2…6,3 times. The analysis of the received changes of parameters of crystalline grids of elements after electron-beam processing showed presence of compressive stresses in hardened surface layers of elements in the thickness of 90... 210 μm for the considered change ranges in the modes of electron-beam technology: for elements of optical ceramics KO2-up to 30...40 MPa; for elements of optical ceramics KO1 – up to 60...70 MPa; for elements of optical ceramics KO5 – up to 55... 65 MPa.

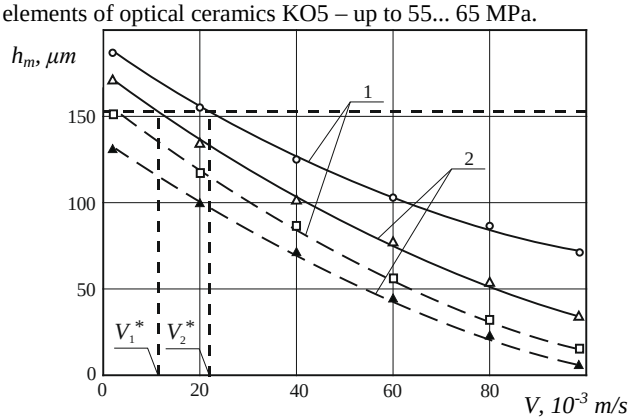

Fig. 5. *Dependence of thickness of melted layer h_m in elements from optical glass BK10 (1) and TF10 (2) on moving speed of electronic stream: ——— – $F_n = 5 \cdot 10^8$ W/m^2 – – – – $F_n = 3 \cdot 10^8$ W/m^2; Δ, ○, □, ▲ – experimental data.*

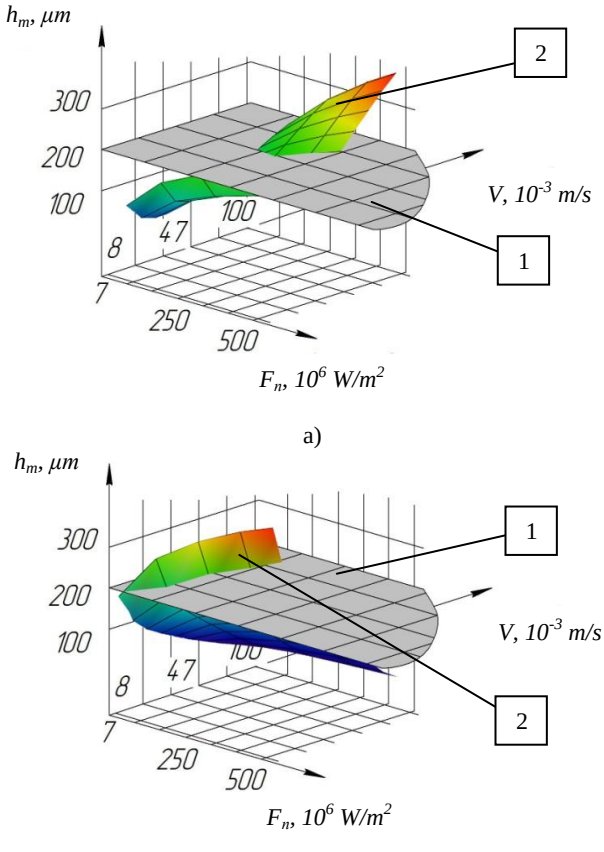

Fig. 6. *Dependencies* $h_m(F_n,V)$ *for elements of optical glass BK10 (a) and K8 (b): 1 – maximum permissible values of* h^**; 2 – values of* h_m *that are obtained when the elements are processed by an electronic beam.*

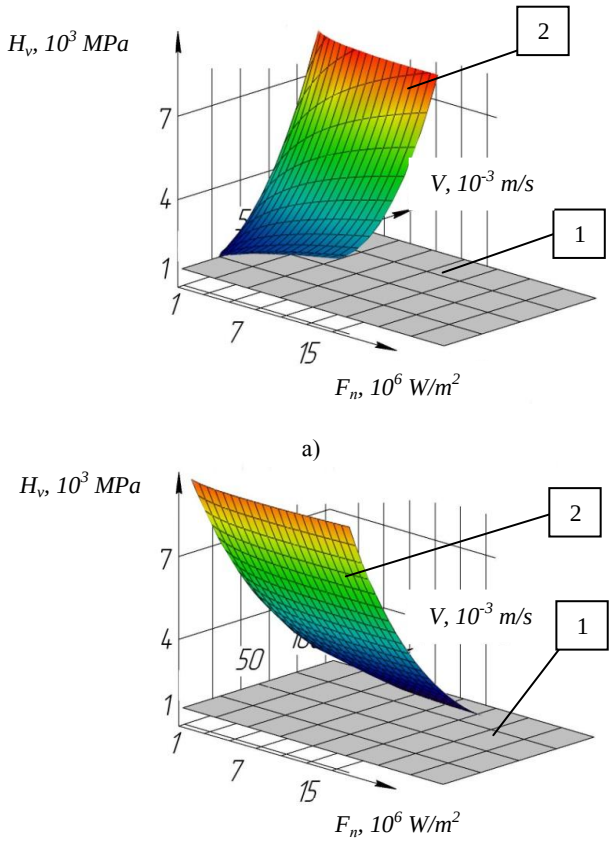

Fig. 7. *Dependencies* $H_v(F_n,V)$ *for elements of optical ceramics KO1 (a) and KO5 (b): 1 – elements unprocessed by an electronic beam; 2 – elements processed by an electronic beam.*

The influence of electron-beam technology modes on microhardness of H_v of surfaces of elements from optical ceramics is defined: increase of to $1{,}5\cdot10^7$ W/m^2 and V to $1{,}5\cdot10^{-2}$ m/s leads to increase of H_v from $1{,}21\cdot10^3\ldots2{,}83\cdot10^3$ MPa to $4{,}84\cdot10^3\ldots7{,}15\cdot10^3$ MPa (Fig. 7).

It is established, that after electron-beam processing of optical elements as a result of increase of cleanliness and reduction of microroughness of a surface by its flowing, the change of its chemical composition and transformation of a crystalline structure, the formation of hardened layers with compressive tensions, their resistance to external thermal and mechanical effects increases. Thus, with the increase of F_n до $8\cdot10^8$ W/m^2 and V до $5\cdot10^{-2}$ m/s, the critical values of external heat flows increase from $0{,}2\cdot10^5\ldots4{,}8\cdot10^5$ W/m^2 to $0{,}4\cdot10^5\ldots8{,}7\cdot10^5$ W/m^2 for the time of their effect 3...20 s (elements of optical glass), as well as from $5{,}1\cdot10^5\ldots2{,}6\cdot10^6$ W/m^2 to $0{,}7\cdot10^6\ldots5{,}2\cdot10^6$ W/m^2 for the time of their effect 5... 35 s (elements made of optical ceramics).

It is also shown that the critical values of thermoelastic stresses σ^* at heating temperatures T = 300…1200 K for elements of optical glass increase from 11... 62 MPa to 17... 115 MPA, and for the elements of optical ceramics – from 75... 115 MPa to 148... 281 MPa.

In addition, the analysis of tests of electronically-beamed elements from optical ceramics according to the standard method (finding the limit values of the critical altitude of the $H_{кр}$, with which the free-falling steel ball ($d = 4\cdot10^{-3}...5\cdot10^{-3}$ m) destroys the surface of the product (the occurrence of cracks, chips)) showed that at $F_n = 10^8\ldots5{,}5\cdot10^8$ W/m^2 и $V = 10^{-2}\ldots5\cdot10^{-2}$ m/s the critical height from which the steel ball falls, destroying the surface of the element, is: for raw elements – $H_{кр}$ = 0,18...1,1 m, and for the processed- $H_{кр}$ = 0,37...1,35 m, that means that for the elements, processed by electron beam, the values of $H_{кр}$ exceed their values for raw elements in 1,2…2,1 times.

The influence of modes of electron-beam technology on the spectral coefficient of transmission of optical elements $k_\lambda(\lambda)$ (λ – wave length) is established: at anincrease of F_n to $8\cdot10^8$ W/m^2 and reduction of V to $5\cdot10^{-3}$ m/s there is an increase of k_λ by 4... 6% for optical glass elements (IR-transparency range from 0,76 μm to 2,75 μm) and 5... 7% for elements of optical ceramics (IR-transparency range from 0,76 μm to 12,5 μm).

The analysis of the conducted experimental researches has allowed to establish the following modes of electron-beam technology within which there is an improvement of performance characteristics of optical elements (microhardness of the surface H_v, spectral coefficient of transmission, resistance to external thermal and mechanical effects): F_n = $7\cdot10^6\ldots8\cdot10^8$ W/m^2, $V = 5\cdot10^{-3}\ldots5\cdot10^{-2}$ m/s.

It is established (table 1), that after finishing electron-beam processing of surfaces of optical elements of devices deviation of their geometrical form from the set ones correspond to accepted in optic-electronic instrument making. In this case, the purity of the surface of optical elements in the class *P* after electron-beam processing is increased by one class of purity (for example, for aerophotographical lenses from VI and to V class, for mirrors- from IV to III, etc.).

Reliability coefficient as a criterion of efficiency of light conductors of laser medical devices at different speeds of external heating was determined according to standard methods (State Standarts of Ukraine 3004-95. Reliability of Techniques. Methods of estimation of reliability indicators by Experimental data). This allowed to establish that the increase in the heating speed of the end surfaces of light conductors of medical devices (from 100 K/s to 400 K/s) results, in the case of electron-beam processing of these surfaces (in the treatment modes $F_n = 3\cdot10^8$ W/m^2 and $V = 8\cdot10^{-3}$ m/s, that provides quartz treatment of the surfaces of elements from

optical glass, which increases their resistance to external heat loads), in increase of the probability of their non-failure work by 10... 15%.

Undertaken researches of hemispherical fairings from optical ceramics on the standard installation that simulate supersonic airflow of fairings by air stream with speed up to $2 \cdot 10^3$ m/s and their axisymmetrical rotation with angular speed up to $4 \cdot 10^3$ rad/s, to which they are exposed during operation, have allowed to establish that in the case of electron-beam processing of their surfaces (at modes of processing $F_n = 5 \cdot 10^8$ W/m^2 and $V = 5 \cdot 10^{-3}$ m/s that provide an increase of microhardness of a surface of optical elements to 5...6 GPa and formation of hardened layers with thickness up to 90... 210 μm, that significantly increases the durability of optical elements to external and mechanical shocks) there is an increase in the probability of their non-failure work by 15...20%.

Table 1

Tolerance values for the quality of raw and processed by an electronic beam optical elements raw ($F_n = 5 \cdot 10^7$ W/m^2, $V = 7 \cdot 10^{-3}$ m/s)

Elements of opto-Electronic devices \ Tolerances on the surface of optical elements by		Curvature N_0, $N^{обр}$		Form ΔN_0, $\Delta N^{обр}$		Purity class P_0, $P^{обр}$	
		N_0	$N^{обр}$	ΔN_0	$\Delta N^{обр}$	P_0	$P^{обр}$
Object glass	collimators and astronomical	1 – 3	3	0,2 – 0,3	0,2	VIII	VII
	Air-photographical	1 – 3	3	0,1 – 0,5	0,5	VI	V
	photographical	3 – 5	5	0,3 – 0,5	0,3	VI	V
Eyelens, enlarging lens		3 – 5	3	0,5 – 0,1	0,5	V	IV
Prisms	reflecting	0,5 – 1	0,5	0,1 – 0,3	0,1	III	II
	refractive	2 – 4	2	0,5 – 1	0,5	IV	III
Ligh filters behind and in front of the eyelens		5 – 10	5	0,8 – 2	0,8	III	II
Mirrors		1 – 2	2	0,2 – 0,3	0,3	IV	III

Note. The following designations are accepted: N_0, ΔN_0, P_0, $N^{обр}$, $\Delta N^{обр}$ and $P^{обр}$ – values of quality indicators of raw and processed by electron beam optical elements respectively.

3. Conclusions

1. For the first time the regularities of influence of electron-beam processing regimes on quantifiable values of quality of elements surface layers from optical glass and ceramics are established:
– the surface of the elements from the optical glass is completely cleared of defects, that were obtained at their mechanical polishing (cracks, scratches, etc.); thus there is an increase of cleanliness level, reduction of microroughness up to 0,4…1,3 nm;
– in the elements of optical glass there occurs superficial flowing to the depth of 130... 220 μm, not violating flatness, thus there is a homogenization of chemical composition of hydrolysis products, and also orientation adjustment near the surface of silicon-oxygen glass grid that approaches to the structure of quartz glass;
– in the elements of optical ceramics there arises compressive voltage up to 30... 70 MPa in hardened surface layers with a thickness of 90... 210 μm.
2. For the first time modes of electron-beam technology are found (density of thermal impact $F_n = 7 \cdot 10^6 \ldots 8 \cdot 10^8$ W/m^2, speed of electron beam movement $V = 5 \cdot 10^{-3} \ldots 5 \cdot 10^{-2}$ m/s), within which there is an improvement in the performance of optical elements:
– increase of surface microhardness of elements from optical ceramics from $1{,}21 \cdot 10^3 \ldots 2{,}86 \cdot 10^3$ MPa to $4{,}84 \cdot 10^3 \ldots 7{,}15 \cdot 10^3$ MPa and increase of the spectral transmission coefficient of IR-radiation by 4... 6% for elements of optical glass and for 5... 7% for elements of optical ceramics;
– there is an increase in the critical values of the external heat flow leading to the destruction of the elements by 1,5... 2 times, with the increase of external pressure up to 10^7 Pa decreases the specified critical values by 1,3…1,5 times; critical values of thermoelastic stresses in optical elements at heating temperatures 300... 1200 K increase by 1,5…2,5 times, indicating an increase in resistance to thermal effects and increased external pressures of optical elements processed by an electronic beam;
– the values of critical heights of falling of a steel ball on their surface, leading to destruction of elements, increase from 0,18…1,1 m to 0,37…1,35 m, thus increasing their resistance to mechanical shocks.
3. New methods of increasing of the operational characteristics of optical elements of optoelectronic devices with the help of electron-beam technology have been developed, allowing to increase the probability of non-failure operation of optical fairings of IR devices and fiber-optic light conductors of laser medical devices at their running by 15... 25%.

4. References

1. Yatsenko I. V., Antoniuk V. S., Vashchenko V. A., Tsybulin V. V. Uprezhdenie vozmozhnych razrushenii opticheskich obtekatelei IK-priborov v usloviyach vystrela i poleta (Preventing possible destruction of the optical fairings of infrared devices in the conditions of a shot and flight) Ezhemesyachnyi nauchno-technicheskii i proizvodstvennyi zhurnal "Nanoinzheneriya", 2015, 12(54), P. 26 – 31.
2. Yatsenko I. V., Antoniuk V. S., Vashchenko V. A., Tsybulin V. V. Poperedzhennya mozhlyvych ruinuvan optychnych elementiv tochnogo pryladobuduvannya v umpovach zovnishnich termodii (Prevention of possible destruction of optical elements of precision instrumentation in conditions of external thermo-influences) Zhurnal nano ta elektronnoi phizyki, 2016, Vol. 8, 1, P. 01027 – 01032.
3. Yatsenko I. V., Antoniuk V. S., Kiritchenko O. V., Vashchenko V. A. Vyznachennya krytychnych znachen parametriv zovnishnich termodii na optychni elementy tochnogo pryladobuduvannya (Determination of critical values of the parameters of external thermo-influences for optical elements of precision instrumentation) Visnyk Natsionalnogo technichnogo universytetu Ukrainy "Kyivskyi politechnichnyi instytut", 2016, 51(1), P. 71 – 75.
4. Yatsenko I. V., Antoniuk V. S., Vashchenko V. A., Tsybulin V. V. Vyznachennya krytychnych znachen parametriv elektronnogo promenu pry poverchnevomu oplavlenni optychnych elementiv tochnogo pryladobuduvannya (Determination of the critical values of the parameters of an electron beam at the surface melting of optical elements of precision instrumentation) Zhurnal nano ta elektronnoi phizyki, 2017, Vol. 9, 1, P. 01010(5).
5. Vashchenko V. A., Yatsenko I. V., Lega Y. G., Kirichenko O. V. Osnovy elektronnoi pbrobky vyrobiv z optychnych materialiv (The basics of electronic processing of optical materials) Kiev: Naukova Dumka, 2011, 562 p.
6. Yatsenko I. V. Doslidzhennya zalezhnostei energetychnych charakterystyk SEP vid yogo kerovanych parametriv pry vplyvi na vyroby mikrooptyky i integralnoi optyky (Investigation of dependencies of power characteristics of TES on its controlled parameters under the influence on products of micro-optics and integral optics) "Trudy Odesskogo politechnicheskogo universiteta", 2009, Issue 2(32), P. 143 – 149.
7. Yatsenko I. V. Experimental and statistical models of impact determination of the electron beam parameters on surface layers properties of optical elements in precision instruments building

"Pratsi. Odes'kyi politechnichnyi universytet", 2016, Issue 1(48), P. 63 – 69.
8. Yatsenko I., Antoniuk V., Bondarenko M., Vashchenko V. Influence of parameters by electronic ray on properties of superficial layers of optical elements of exact instrument-making. International journal for science and innovations for the industry "Innovations in discrete productions", ISSN 114-8907, YEAR III, ISSUE 1/2015, Sofia, P. 13 – 15.
9. Yatsenko I., Antoniuk V., Kiritchenko O., Vashchenko V. Improvement of technical and operational characteristics of devices with optical elements by preliminary electron beam treatment of their surface. International journal for science and innovations for the industry "Machines. Technologies. Materials", ISSN 1313-0226, YEAR X, ISSUE 6/2016, Bulgaria, P. 47 – 50.
10. Yatsenko I., Antoniuk V., Kiritchenko O., Vashchenko V., Tsybulin V. Increasing the resistance of precision instrument-making elements from optical glass to external thermo-influences by preliminary electron-beam processing of surfaces. International journal for science and innovations for the industry "Innovations in discrete productions" ISSN 1314-8907, YEAR IX, ISSUE 1/2016, Bulgaria, P. 9 – 12.
11. Yatsenko I., Antoniuk V., Kiritchenko O., Vashchenko V., Tsybulin V. Improving the reliability instruments of measuring and thermal control of objects of different physical nature by the finish of electron beam processing surfaces of optical elements. International journal for science and innovations for the industry "Machines. Technologies. Materials" ISSN 1313-0226, YEAR XI, ISSUE 1/2017, Bulgaria, P. 20 – 23.

THE STRUCTURAL RELIABILITY AND ADEQUACY ASSESSMENT OF THE INDUSTRIAL ELECTRIC POWER SYSTEMS WITH LOCAL POWER PLANTS

ОЦЕНКА СТРУКТУРНОЙ И БАЛАНСОВОЙ НАДЕЖНОСТИ ПРОМЫШЛЕННЫХ СИСТЕМ ЭЛЕКТРОСНАБЖЕНИЯ С СОБСТВЕННЫМИ ЭЛЕКТРОСТАНЦИЯМИ

Assoc. Prof. Malafeev A., PhD Student Iuldasheva A.
Nosov Magnitogorsk State Technical University, Magnitogorsk, Russia
alinayuldasheva1@gmail.com, malapheev_av@mail.ru

Abstract. *In this paper methods of estimating the structural reliability and adequacy of the large industrial enterprises are considered. The combination of the sequential network reduction method and the Newton's method is proposed for the calculation of structural reliability indices. Estimation of the adequacy is based on the random events simulation by Monte Carlo method.*
KEYWORDS: POWER SUPPLY, INDUSTRIAL ENTERPRISE, STRUCTURAL RELIABILITY, LOCAL POWER PLANT, RELIABILITY INDICES, ADEQUACY, MONTE CARLO METHOD, SEQUENTIAL REDUCTION

1. Introduction

Reliability indices as well as economic and operating parameters should be taken into account when analyzing operation of the power supply systems of large industrial enterprises. This is nessesary for the development of project proposals for reconstruction of distribution networks and for planning of normal operating schemes with predictive calculations of post-accident conditions. The analysis of existing reliability assessment methods for the power supply systems had shown that their use to the objects as the power supply system of a large industrial enterprise with a combination of open and meshed networks is difficult. This is primarily due to the fact that existing methods suggest the individual in-depth analysis of each scheme and different criteria for reliability assessment. Such methods as logic-probabilistic and table-logical practically inapplicable due to the extreme complexity of the resulting fault tree or a table of expected logical connections. Thus, development of a methodology for the equivalent reliability indices calculation of power supply systems of large industrial enterprises is of immediate interest.

2. Review of publications

System reliability includes two basic aspects – adequacy and security. Adequacy relates to the existence of sufficient facilities within the system to satisfy the consumer load demand. Security relates to the ability of the system to respond to disturbances arising within that system.

Evaluation of the adequacy is one of the main tasks in mode planning for power system. Deterministic and probabilistic techniques are the ones widely used for the evaluation of adequacy. Among probabilistic methods analytical, non-sequential and sequential Monte Carlo simulation are commonly used for calculation of generating system adequacy [1]. Sequential Monte Carlo simulation is often proposed for short-term reliability analysis of complex power system. In paper [2] the adaptive importance sampling technology is proposed for the improvement of the simulation efficiency of this method. There are also techniques based on minimal cut set approach (MCSA) or failure mode and effect analysis (FMEA) developed for reliability analysis [3]. Paper [4] presents a modified four-state model that can be used to assess adequacy with deterministic approaches at the power system generation level. Proposed technique allows to evaluate static reserve capacity and margin in a generating system for a given risk criterion.

Serious attention is paid to assessment of reliability from the regime positions. In a number of works the reliability assessment is considered in the context of the larger task of planning the development of generation, supply and distribution systems, taking into account the costs of reconstruction on the basis of a multi-purpose non-linear control model [5]. The approach based on a set of Pareto is widely used for this task. The article [6] devoted to assessing of the reliability indices sensitivity (primarily of loss of load probability (LOLP)), taking into account the regime restrictions of systems including power transmission on direct and alternating currents. The fault tree method in conjunction with the Monte Carlo method are used in [7] for reliability analysis in SmartGrids, this approach is applied to assess the criterion LOLP and to quantify the risks on its basis. The assesement of cogeneration system's reliability is also of great current interest; Markov chains are used for the failure flow simulation in the article [8] for such systems.

Literature review had shown that most of the researches concentrated on the reliability issues for generation, distribution and retail electricity companies, but reliability assessment for the consumers is considered less often. Analysis of existing methods demonstrated the necessity of development a method that takes into account the peculiarities of specific system and allows to calculate the reliability indices with the required accuracy.

3. The methodology for the calculation of structural reliability of power supply system

Combination of the sequential network reduction method [9] and the Newton's method is proposed for equivalent reliability indices calculation for meshed networks. According to the proposed algorithm, a block diagram, which represents an analog of real elements connections of power supply scheme: transformers (T), circuit breakers (CB), overhead lines (PL), generators (G) and cables, is composed. The algorithm takes into account power flow direction on the system's elements. Thus, the part of scheme which is not involved to the electricity transmission to particular consumer will be excluded from the equivalent reliability indices calculation. Detailed description of simplification algorithm is presented in [10]. On the basis of the developed algorithm in the program complex KATRAN [11] the block "Reliability" was created.

As an example the Magnitogorsk energy hub (MEH) is considered. The main electricity consumer of MEH is PJSC "Magnitogorsk Iron and Steel Works" with the blast furnace shop (BFS), the oxygen-converter plant, the electric-furnace melting shop (MSP), hot and cold rolling departments.

The algorithm was implemented for structural reliability analysis of power supply system of the BFS (the scheme is presented at Fig. 1). For reliability assessment of BFS power supply the scheme of Substation 7 (Ss-7) power supply was evaluated by 10 kV switchgear in various operating modes. Calculations are carried out in PC KATRAN and results are shown in Table 1.

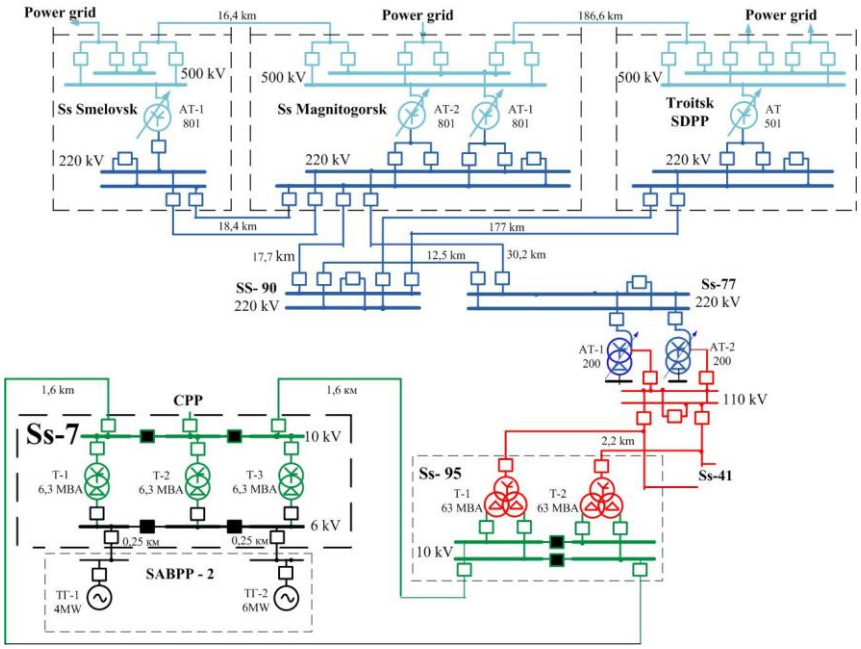

Fig. 1. *BFS power supply scheme.*

Table 1. The results of reliability indices calculation for BFS.

Operating mode	Probability of no-failure, p_{ekv}	Failure intensity, w_{ekv} (1/h)	Recovery time, T_{Rekv} (h)
Normal	0.99989	0.042	0.0026
Planned maintenance of G-2, failure of CB-1	0.99884	0.06	0.0193
Planned maintenance of T-2, failure of CL-1	0.99869	0.063	0.0208
Failure of B-2 and PL-1	0.99913	0.055	0.0158

On the basis of calculations it is possible to carry out comparison of the different operating modes and identify the emergency conditions. Among the considered options the combination of the repair mode (T-2 failure at Ss-95) and of the emergency outage (PL-1 failure) leads to the heaviest conditions. The analysis of outages statistics of Ss-7 had shown that 70% of the outages are caused by damage to cable lines (CL). Thus, to increase the power supply reliability such measures as CL-state control, adding of more protective devices and updating of equipment can be recommended.

4. Evaluation of power supply adequacy

The adequacy characterizes the ability to meet an electricity demand during system's elements outages. Adequacy is usually considered in the long-term development perspective for assessment of reserve capacity sufficiency and transmission capacitance of system interconnections.

Methodology of adequacy assessment is based on the Monte Carlo method, because majority of phenomena in the power supply system are random. According to this method, at the first step of calculation the possible states of overhead transmission lines, transformers and generators of enterprise's power plant are composed; at the next step the power shortage estimation and adequacy indices calculation are carried out.

It is proposed to evaluate following indices of the adequacy:

1. The average consumer's restriction on one node of the system, (MW/year)

$$\Delta P_{AV} = \frac{\sum_{i=1}^{K} \Delta P_j \cdot \lambda_j}{K},$$

where ΔP_j - average value of the restrictions, MW; λ_j - average number of restrictions, (1/year); K - number of nodes.

2. The system index of a power failure, (1/year)

$$S_{\Sigma} = \frac{\sum_{i=1}^{K} \Delta P_j \cdot \lambda_j}{P_{\Sigma}},$$

where P_{Σ} – the peak of total load of controlled system components, MW.

As an example, the MEH power supply system (Fig.2) was used to demonstrate the method of adequacy estimation. There are 3 main sources of their own power supply - combined heat and power plant (CHP), central power plant (CPP), steam-air blow power plant (SABPP). The installed capacity of CPP =191 MW, CHP=330 MW, SABPP-1,2=102 MW. The MEH has four distribution substations (MSDS) of 220/110 kV, which together with the CHP and the central power plant form two closed circuit.

With the help of the PC KATRAN the block diagram of the MEH networks was compiled and mode calculation for different parameters was carried out. The dependence of voltage on the CHP and CPP busbar from their power was considered (Table 2).

Table 2. The dependence of voltage at the switchgear of the entrprice's power plant on electricity production, kV.

Type of power plant	Normal mode	50% of production	10% of production
CPP, SABPP	114.5	113.24	112.04
CHP	112.81	108.98	104.94

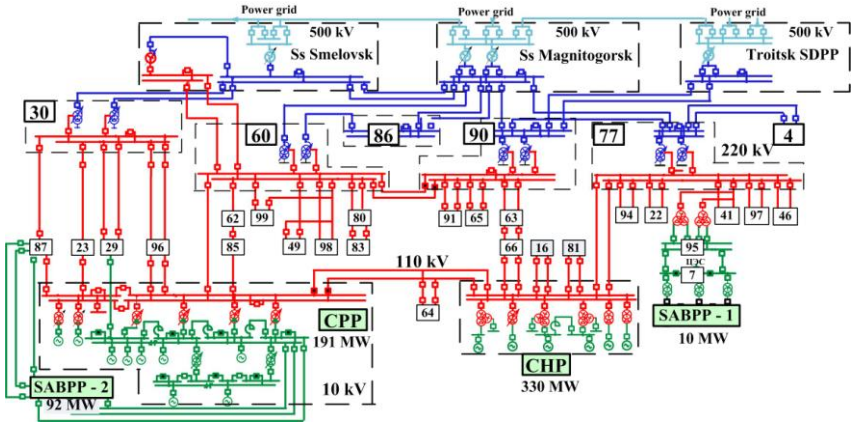

Fig. 2. *Scheme of power distribution of enterprise's power plants.*

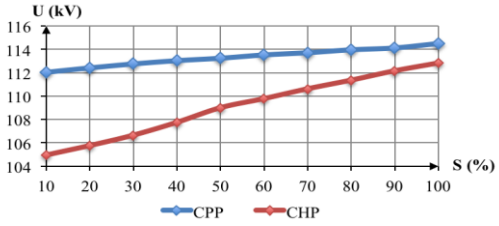

Fig. 3. The dependence of voltage (U) at the switchgear of the entrprice's power plant on electricity production (S).

1. The effect of power production reduction at the power plant on the voltage at the switchgears of consumers substations. Changes in CHP production were considered. When CHP production decrease up to 10% of the rated the voltage at power plant switchgears and at consumers switchgears is decreased by 4.6%, which adversely affects to the reliability of power supply. However, this operation mode may be needed in terms of increasing the output heat energy demands in the winter time, in case of failure of urban heat supply sources or in case of failure of enterprise peak boilers. The measures concerning consumers load reduction or regulation of OLTC transformers could be chosen to increase the voltage.

The CHP provides power for a great number of consumers due to this a lot of random combinations of changes in consumer load are possible. The Monte Carlo method is used to solve this problem. Using a random number generator (from MS Excel package) the possible combinations of load on the consumers busbar was generated. Load values are determined in accordance with the load diagram

$$P_i = M(P_i)[1 \pm \varepsilon_m(P_i)\xi_n], \quad (3)$$

$$Q_i = M(Q_i)[1 \pm \varepsilon_m(Q_i)\xi_n], \quad (4)$$

where $\varepsilon_m(P_i)$, $\varepsilon_m(Q_i)$ - the variation coefficients of active and reactive loads; ξ_n - random numbers ranging from 0 to 1 for normal law of distribution.

The load changes on the switchgears of substations, which provide power for the most energy-intensive consumers, are considered: Ss - 16, 22, 41, 46, 64, 66, 81, 94, 95, 97 (Fig. 2.). Thus, the number of nodes K=10. After analysis of the consumers peculiarities (the category of power supply reliability, production technology), the maximum possible load reduction was set for each substation. For example, the Ss-95 permissible load reduction is only up to 20% of nominal. In terms of CHP heat-end mode operation in order to avoid reducing the voltage at the control points to the emergency level the system operator decides to reduce the load; there could be a large number of load combinations. Some possible combinations of load reduction are given in Table. 3. The average value ΔP_j and the number l_j of restrictions for each substation and the peak of total load P_Σ for all substation in general can be estimated from this dependence.

Table 3. *The load limitation on the consumer substations busbar in order to maintain the mode setting*.

№	$\xi_н$	The load values on the Ss-16, MW					The load values on the Ss-22, MW							The load values on the Ss-95, MW		
		P_i	$0.9\ P_i$	$0.8\ P_i$	$0.7\ P_i$	$0.6\ P_i$	P_i	$0.9\ P_i$	$0.8\ P_i$	$0.7\ P_i$	$0.6\ P_i$	$0.5\ P_i$		Pi	$0.9\ P_i$	$0.8\ P_i$
1	0.54	12.15	1.22	2.43	3.65	4.86	21.51	2.15	4.3	6.45	8.61	10.8	…	8.56	0.86	1.71
2	0.59	5.7	0.57	1.14	1.71	2.28	10.09	1.01	2.02	3.03	4,04	5.04		4.01	0.4	0.8
…																
12	0.16	3.65	0.36	0.73	1.09	1.46	6.46	0.65	1.29	1.94	2.58	3.23		2.57	0.26	0.51
P_Σ=238.1 MW		$\lambda_{Ss\text{-}16}$=23/48, $\Delta P_{Ss\text{-}16}$=102.8 MW					$\lambda_{Ss\text{-}22}$=41/60, $\Delta P_{Ss\text{-}22}$=328.58 MW							$\lambda_{Ss\text{-}95}$=12/36, $\Delta P_{Ss\text{-}95}$=32.6 MW		

With the help of this data it is possible to calculate the average consumer restriction on the one system's node and the system index of power failure:

ΔP_{AV} =5.6 MW/year, S_Σ =0.235 1/ year.

The results testify that decrease of power generation by enterprise's power plants will promote the consumers power supply reliability decrease. Stable operation of system will be possible even in case of the significant decrease in the electricity production on enterprise's power plant if the operating and dispatching personnel work correctly. But at the same time the load decrease on the customer's switchgears leads to lower productivity, poor performance of variable speed drives and defective products. Thus, it is necessary to make an assessment of possible damage in the question of customers load reduction.

2. The effect of power production reduction at the power plant to the increment of power receiving from the grid. The increment of power receiving from the grid is considered at the example of the CPP production reduction. In case of CPP production decrease up to 10% of the rated, the normal operation of power plant and of its consumers will be maintained by the means of receiving the extra amount of the power from the grid. Meantime, additional power consumption will cause the breach of contractual obligations to the

energy retail companies. Increment of the power amount receiving from the grid when the mode transfer from the normal power generation (from values P_1, Q_1) up to the 10% power generation mode (to the value P_2, Q_2) is displayed in Table 4.

Table 4. *Change the volume of the received power from the system while reducing the generation of its own power plants*.

The load on the 220kV busbar of MSDS	Points of delivery (N)						Total
	Ss-30	Ss-90		Ss-60	Ss-86	Ss-77	
	1	2	3	4	5	6	
	PL-1,2 to the Ss Smelovsky	PL-1 to the Ss Magni-togorsk	PL-1,2 to the Ss Troitsk	PL-1 to the Ss Magni-togorsk	PL-1,2 to the Ss Magni-togorsk	PL-1 to the Ss Magni-togorsk	
P_1+j Q_1, MVA	-11.16-j6.98	-8.13-j7.76	506.72+j997.48	-1.45-j3.35	507.34+j61.62	171.9-j88.47	1165.22+j952.54
P_2+jQ_2, MVA	4.7-j8.6	-3.73-j1.06	604.48+j1030.12	3.54-j3.93	561.22+j109.66	242.99-j13.86	1413.2+j1112.33
ΔP+j ΔQ, MVA	15.86-j1.62	4.4+j6.7	97.76+j32.64	4.99-j0.58	53.88+j48.04	71.09+j74.61	**247.98+j159.79**

Thus, the power generation reduction to 10% of the nominal will lead to the extra reception of the power from the grid: by active power on ΔP= 247.98 MW and reactive power on ΔQ = 159.79 MVAr. Power reception form the grid wouldn't exceed contracted volumes only in two points of delivery (E) - 2 and 4. From Table 4 - the average number of cases exceeding the contractual consumption λ_i: $\lambda_i = \frac{E}{N} = \frac{2}{6}$.

According to the current legislation consumer is obliged to comply with the agreement of energy consumption mode. Responsibility in the form of compensation for actual damages for breach of power supply contract is formalized. Payment for power consumption difference is determined by the contract. Typically, such a penalty is set at multiple of the normal rate of pay actually consumed power (for example, by a factor of 5).

Costs for the purchase of an additional amount of power

$$C = \Delta P \cdot T \cdot F \cdot t \,, \tag{5}$$

where T – the electricity tariff, RUR/kW (for the considered example T = 2.7 RUR/kW); F – the amount of fines (for the considered example F = 5); t - period of reception of the additional power amount from grid (it is assumed that additional reception will be carried out in winter period, t = 3).

C =247.98 MW·2.7 RUR/kW·5·3 = 10,043,190 RUR.

Based on these data we can calculate the average increasing of power consumption at a single point of supply

$$\Delta P_{C.AV} = \frac{\sum_{i=1}^{N} \Delta P_i \cdot \lambda_i}{N} \,, \tag{6}$$

where ΔP_i – the value of increasing consumption, above specified in the contract, MW (ΔP=247.98 MW).

$$\Delta P_{C.AV} = \frac{247.98 \cdot \frac{2}{6}}{6} = 13.78\, MW.$$

The sale of additional volumes of heat energy will cover the purchase of electric power from the grid as in the case of deficiency of heat energy value the potential damage significantly exceeds the payment of fines for the deviation in electricity consumption.

5. Conclusion

The proposed algorithm allows to calculate basic structural reliability indices for the power system as a whole and for it individual sections, as well as for schemes of power distribution of the enterprise's own power plants. The algorithm can be used for the project development of normal and repair operational modes and for prediction calculations of possible post-emergency regimes taking into account reliability.

For the adequacy assessment the modes calculation of the enterprise's own power plants and their consumers, in case of reducing power generated at these power plants, was carried out. The Monte Carlo method is used for the compilation of the possible combinations consumer's load values. As a result, it was found that power generation decrease by enterprise's power plants adversely affects to the reliability of consumers power supply, as it reduces the voltage on the busbars of consumer substations. Therefore, when deciding on the limitation load is necessary to choose the best combination of consumer restrictions and to assess possible damage to consumers. In paper the additional adequacy criterion is proposed for power supply system, which is in evaluation of the value of average increasing of power consumption according to the number of supply points.

References

[1] Almutairi, A., A. Abdulaziz, M.M.A. Mohamed Hassan Salama, Probabilistic generating capacity adequacy evaluation: Research roadmap-Electric Power Systems Research, Vol. 129, 2015, p. 83-93.

[2] Wang, Y., C. Guo, Q. Wu, S. Dong, Adaptive sequential importance sampling technique for short-term composite power system adequacy evaluation, IET Generation, Transmission & Distribution., Vol. 8, 2014, p. 730-741.

[3] Allan, R., R. Billinton, A. Breipohl, C. Grigg, Bibliography on the application of probability methods in power system reliability evaluation-IEEE Transactions on Power Systems, Vol.9, 1994, pp.41–49.

[4] Chowdhury, N., H. Khonsari, Adequacy assessment using a modified four-state model-Quality & Reliability Engineering International, Vol. 14, 1998, p. 145-151.

[5] Cossi, A., L.G.W. da Silva, R.A.R. Lázaro, Primary power distribution systems planning taking into account reliability, operation and expansion costs-IET Generation, Transmission & Distribution, Vol. 6, 2012, pp. 274-284.

[6] Jirutitijaroen, P., C. Singh, Reliability Constrained Multi-Area Adequacy Planning Using Stochastic Programming With Sample-Average Approximations-IEEE Transactions on Power Systems, Vol. 23, 2008, p. 504-513.

[7] Arya, L., A. Koshti, A. Ganguly, R. Sheikh, Adequacy Assessment of a Distribution System Having Distributed Generation (DG) Under Extreme Probability Distributions-IUP Journal of Electrical & Electronics Engineering, Vol. 3 Issue 3, 2010, p. 42-48.

[8] Tanrioven M., Reliability and cost–benefits of adding alternate power sources to an independent micro-grid community-Journal of Power Sources, Vol. 150, 2005, p. 136-149.

[9] Igumenschev, V., B. Zaslavets, A. Malafeev, O. Bulanova, Y. Rotanova, The modified method of successive equivalenting for calculation of complex modes of power supply systems, Industrial Power Engineering, Issue 6, pp. 16-22, 2008.

[10] Yuldasheva A., Malafeev A., Electricity supply reliability of the industrial enterprises with local power plants and the outage cost evaluation: Proceedings of the International scientific symposium Electrical power engineering, TU Varna, 2014, p. 10 -12.

[11] Igumenschev, V., A. Malafeev, E. Panova, A. Varganova, O. Gazizova, Y. Kondrashova, V. Zinovev, K. Saveleva, A. Iuldasheva, A. Krubcova, N. Kurilova, Certificate 2015662725, Russia, Programme "The complex of automated modal analysis KATRAN 9.0"-The Bulletin Programme for the computer, database, TIMS, Vol. 4, 2015.

STRESS-STRAIN STATE OF OIL TANKS FOR TERRESTRIAL LASER SCANNING MODEL

НАПРЯЖЕННО-ДЕФОРМИРОВАННОЕ СОСТОЯНИЕ РЕЗЕРВУАРОВ ПО РЕЗУЛЬТАТАМ НАЗЕМНОГО ЛАЗЕРНОГО СКАНИРОВАНИЯ

Prof. Doctor of Science Vasiliev Gennady G., As.prof. PhD. Salnikov Anton P., As.prof. PhD. Leonovich Igor A, Eng. Kukurina Kalina K.

Gubkin Russian State University of Oil and Gas (National Research University), Moscow, Russia

E-mail: SRGNP@gubkin.ru, ahtoh-c@mail.ru, ned.flander@mail.ru, kalina_kras@abv.bg

Abstract: *The paper proposes a methodology for applying three-dimensional laser scanning to obtain an accurate three-dimensional models that will be used to calculate the stress-strain state of constructions of tanks for oil and gas.*

Keywords: GEODETIC INSPECTION, STRESS-STRAIN STATE, TERRESTRIAL LASER SCANNING, VERTICAL STEEL TANKS

1. Introduction

The paper proposes a methodology for applying three-dimensional laser scanning to obtain an accurate three-dimensional models that will be used to calculate the stress-strain state of constructions of tanks for oil and gas.

In the process of operation of the vertical steel tank it purchases a significant deviation from its design position and status. In particular, forms sludge in the tanks (uniform and non-uniform) and change of their geometric shapes (deviation of the generatrix from the vertical, indentations, curves, etc.).

2. Preconditions and means for resolving the problem

The decision making on the need to carry out work on the restoration of the state of the tank is made on the basis of two parallel and interrelated criteria:

1) comparison of data on the spatial position of the tank and its geometric shape, obtained in the process of geodetic inspection, with tabular data presented in normative documents;

2) determination of stress-strain state defects of the tank on the basis of geodetic inspection data.

However, this system has a number of significant disadvantages, including the following:

- Low level of detail in data on the spatial position and geometric shape of the tanks after the geodetic inspection. The data obtained during the geodetic inspection, allow only in general terms, by key points (in particular intersections forming with horizontal welds) to judge the actual geometric shape of the tank. Thus the form of a surface of the wall, lying between these points, except for inadmissible indentations (bulges), remains for us "unknown". In particular, it is possible to judge only approximately where this or that indentation (bulge) begins and ends, where the wall coincides with the vertical, etc.;
- High labor intensity of the work and subsequent post processing of the data of the tank geodetic inspection. The specialist in geodetic inspections is required to manually measure the spatial position of each necessary point, the number of which increases significantly with the increase in the volume of VST. In the presence of unacceptable indentations (bulges) the number of required measurements increases even more. Also, a significant amount of work must be done during the cameral processing of the data and the construction of a three-dimensional computer model of the tank;
- Long term performance of works;
- The need for additional travel to the object, when detecting errors in the geodetic inspection at the stage of the cameral processing of the data;
- High probability of errors (human factor) due to low automation of the process. In this case, it should be noted that the criticality of defects subject to additional measurement, in fact, is determined visually by a specialist conducting work on the geodetic inspection of the tank. At the same time, there is a high probability of errors, in which part of the critical defects will not be reflected in the results of the survey;
- Decide on the necessary repair of the tank according to standard tabular data occurs when the separate consideration of non-uniform sludge in the tanks and a forming deviation from the vertical. Moreover, if we analyze the values of the critical values specified in the regulations, we can establish that most of them were specified in the SN 26-58 “Technical conditions of manufacture and installation of steel cylindrical vertical tanks for storage of oil and petroleum products”;
- There is no specific method for calculating the stress-strain state of tanks in operation. All of the above says that the existing system for monitoring the spatial position of vertical steel tanks and determining their stress-strain state should be, if not changed, at least upgraded on the basis of the use of modern high-tech and high-performance measuring instruments and software systems. The solution to this situation can be the use of ground-based three-dimensional laser scanning and software systems that implement the finite element method. [1], [2], [3]

3. Solution of the examined problem

Laser scanning technology is based on measuring the distance from the laser rangefinder to the surface of the scanned object and two angles (horizontal and vertical) that determine the direction of the vector from the laser rangefinder to the object in the coordinate system of the laser scanner. The spatial vector determines the position of the surface point of the object being scanned. As a result, a cloud of surface points of the scanned object is formed, which reflects the real information about its spatial position and its geometric shape.

In other words, the technology of laser scanning represents a new stage in the development of technology of electronic total stations, in which a subject is being shot in automatic mode.

The technology of three-dimensional laser scanning was analyzed by the employees of the Department of Construction and repair of oil pipelines and storages of Gubkin Russian state University of oil and gas (NIU), were considered the main features of its applications, features of different generations of laser scanners

and their characteristics. As a result, a new approach to this technology was proposed. Precisely the consideration of laser scanners not as a replacement of existing surveying instruments, but as a conceptually and technologically new diagnostic device that opens up new opportunities.

So laser scanning was subjected to tanks with a pontoon volume of 5000 and 20000 m^3, located in earthen banking. Tanks of this volume are most common in the oil industry of Russia, and the earthen can improve the convenience of the scanner location when shooting. The tanks were emptied and prepared for repair.

4. Results and discussion

As a result of the performed works, clouds of points of both tanks were obtained, which were further processed in specialized software complexes to obtain three-dimensional models of the surface of the walls, suitable for the analysis of their stress-strain state in programs implementing the finite element method.

To perform the comparative analysis, models of stress-strain state of the real wall of vertical steel cylindrical tank-5000 (figure 1 and 2) and vertical steel cylindrical tank-20000 (figure 3 and 4), as well as the ideal wall of these tanks (figure 5, 6, 7), were constructed. The models were loaded with hydrostatic load.

A comparison of this models shows:

The stress-strain state of the model of the" real " tank wall obtained by three-dimensional laser scanning reflects the real state of the wall much more accurately and in more details than any idealized models;

- The pattern of deformations of the real wall model differs significantly from the deformations of the ideal model, both in terms of values and the nature of the distribution of deformation on the wall. For example, for VST-5000, the maximum deformation of the real wall is 1.5 times greater than the deformation in the ideal model, and the location of the maximum deformation zones is determined primarily by the defects in the geometry of the wall, rather than by the applied load. For VST-20000, the deformations of the real wall differ significantly from those of the ideal wall due to the presence of a significant number of geometric defects on the wall.

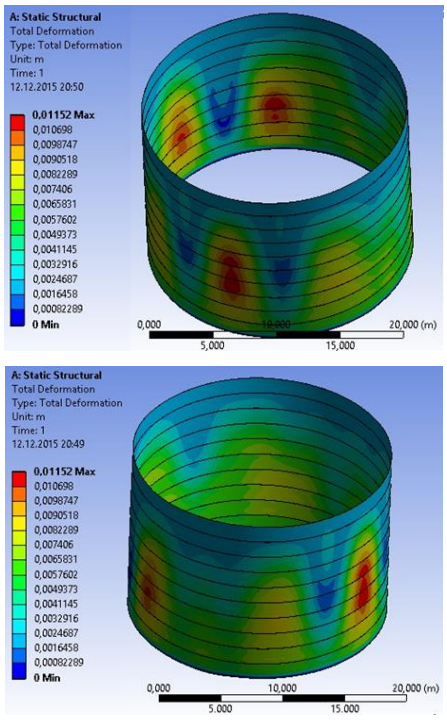

Fig. 1 *Deformation of a three-dimensional model of a "real" wall of vertical steel cylindrical tank-5000, m*

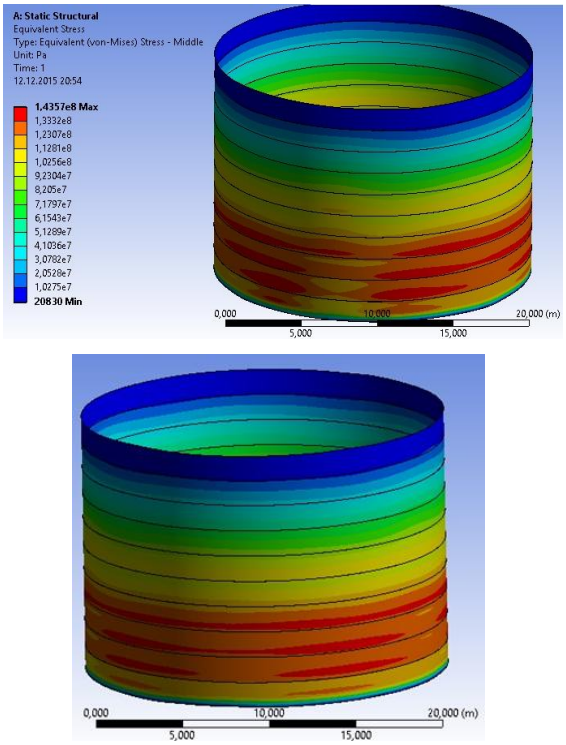

Fig. 2 *Median equivalent stresses according to Mises three-dimensional model of the "real" wall of vertical steel cylindrical tank -5000, Pa*

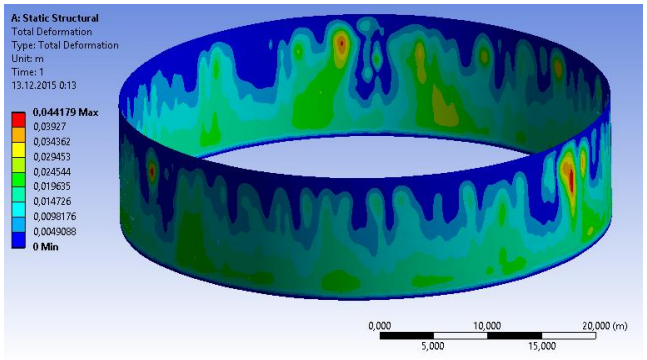

Fig. 3 *Deformation three-dimensional model of the "real"*

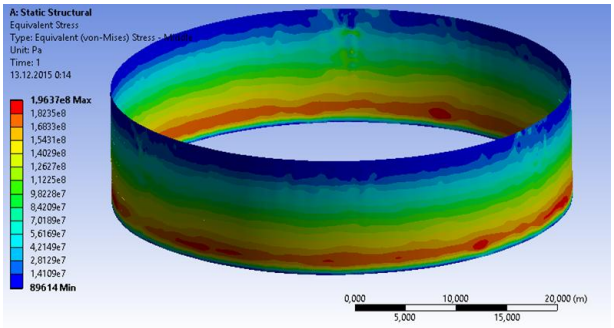

Fig. 4 *Median equivalent stresses according to Mises three-dimensional model of the "real" wall of vertical steel cylindrical tank -20000, Pa*

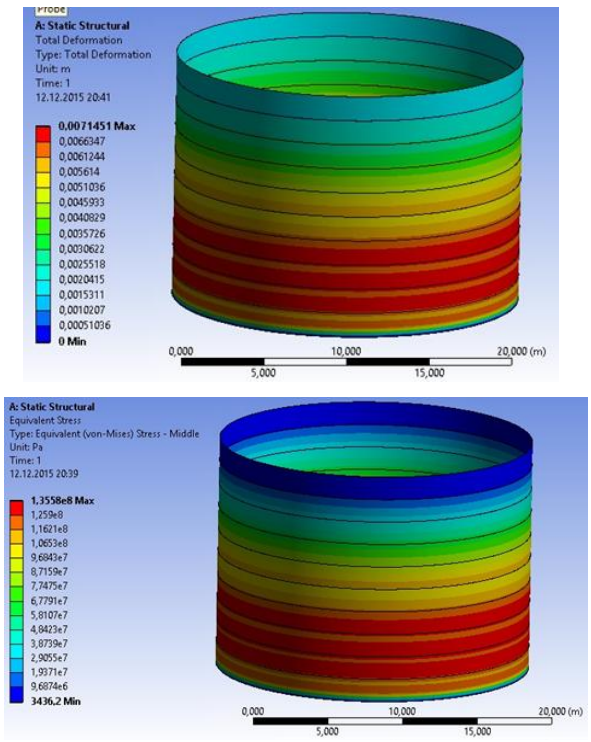

Fig. 5 *Deformation and median equivalent stress according to Mises three-dimensional model of «ideal» wall of vertical steel cylindrical tank-5000, m*

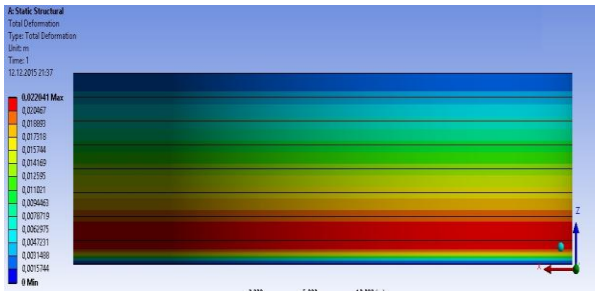

Fig. 6 *Deformation of a three-dimensional model of an "ideal" wall of vertical steel cylindrical tank-20000, m*

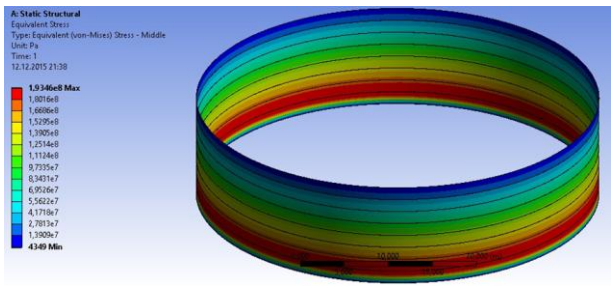

Fig. 7 *Median "equivalent" stresses according to Mises three-dimensional model of an "ideal" wall of vertical steel cylindrical tank -20000, Pa*

- It should be noted that the actual tank wall may be characterized by geometry defects such as indentations. Which will remain even under hydrostatic load (figure 8).

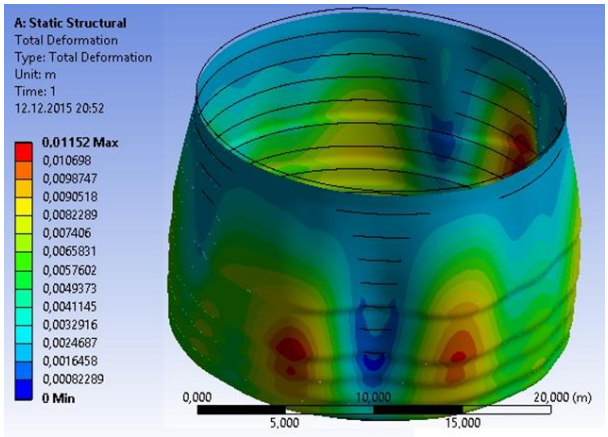

Fig. 8 *Deformation of the real wall vertical steel cylindrical tanks-5000 in scale (black curves show the location of the rings without load), m*

- The stress in the real wall of the tank is also different from the stresses generated in the wall of the ideal model. For example, the value of the equivalent mid-point stresses according to Mises model for each of the rings of the real wall of the VST-5000 is on average 10% more than the same stresses in the case of the ideal wall.

Conclusions: During operation the number of geometry defects increases and they begin to have a significant impact on the stress-strain state of these tanks. In order to determine their technical conditions and residual life, these defects should be taken into account to prevent the occurrence of an emergency situation. Widespread and used well-known geodetic methods for monitoring the geometry of tanks allow to assess the defects in geometry only at certain points that are significantly (up to 6 m) distant from each other. When modeling using this data, the surface of the tank between these points is restored by approximation methods using an ideal model that does not reflect the real geometry and its defects and does not allow to obtain reliable models of the stress-strain state.

The use of three-dimensional laser scanning when creating a strain-stressed state allows to avoid these disadvantages and to obtain the most realistic values of the parameters of the strain-stressed state for a tank in operation.

References

1) Vasiliev G.G., Lejnev M.A., Salnikov A.P.,.Leonovich I.A., Katanov A.A., Lijovztev M.V. On the application of ground-based laser scanning in the oil and gas industry // Science and technology of pipeline transportation of oil and oil products. – 2014. – №4(16), page. 47-51.

2) Vasiliev G.G., Lejnev M.A., Salnikov A.P.,.Leonovich I.A., Katanov A.A., Lijovztev M.V. Work on three-dimensional laser scanning of vertical steel cylindrical tanks -20000 // Science and technology of pipeline transportation of oil and oil products. – 2015. – №1(17), page. 54-59.

3) Vasiliev G.G., Lejnev M.A., Salnikov A.P.,. Leonovich I.A., Katanov A.A., Lijovztev M.V. Analysis of the experience in the use of three-dimensional laser scanning on the objects of "Transneft"Ltd. // Science and technology of pipeline transportation of oil and oil products. – 2015. – №2(18), page. 48-55.

PROSPECTS FOR DEVELOPMENT OF NUCLEAR ENERGY IN BULGARIA

ПЕРСПЕКТИВИ ЗА РАЗВИТИЕ НА ЯДРЕНАТА ЕНЕРГЕТИКА В БЪЛГАРИЯ

Chief Assistant Professor PhD eng. Dolchinkov N. T.,
National Military University „Vasil Levski“, Veliko Tarnovo, Bulgaria,
National Research University "Moscow Power Engineering Institute", Moscow, Russia
n_dolchinkov@abv.bg

Abstract: *The project to build a second nuclear power plant in Bulgaria emerged in the 70s of XX century. He repeatedly starts and stops over the past decades, mostly under the influence of external and internal policy decisions. Meanwhile, Bulgarian taxpayers pay large sums for errors and indecision of our political elite. Time specialists in this area say their arguments and take the best decision for Bulgaria instead of wasting money without end.*

KEYWORDS: *NUCLEAR ENERGY, DEVELOPMENT, NUCLEAR POWER, NPP, CONSTRUCTION, GOVERMENT*

1. Introduction

Nuclear power worldwide provides more than 30% of global electricity production. Under normal conditions of operation of the NPP there is no high risk and the potential damage to the population is much lower than in the areas around the TPP or the major chemical plants of the oil or nitrogen-fertilizer industries.

The construction of a second nuclear power plant in Bulgaria began to be heard in the middle of the 1970s at the highest state level. During this decade, the exploration of the terrain for the construction of a new nuclear power plant began. Detailed research has been made on 26 potential sites, 4 of which are inside the country, 7 are along the Black Sea coast and 15 along the Danube. In choosing a major factor was the availability of sufficient water for the technical water supply of the future plant in order to ensure the normal and safe operation of future reactors and the accompanying equipment. Until the last stage, there are 3 potential terrains located along the Danube - Belene, Vardim and Batin. By Protocol No. 315 / 26.02.1979 the Ministry of Economy offered the site in Belene for approval because:

1. It is the most favorable from the engineering point of view for the construction of the site, the adjacent infrastructure, the development of the general plan of the NPP, the construction of the accompanying communication and household infrastructure projects;

2. The Belene-East terrain falls on a very large block of earth crust in which there are no active faults;

3. Additional macro- and microseismic studies show that this terrain has better seismic characteristics than the other two.

In 1980-1981, the Geophysical Institute at BAS and Energoproekt made a re-analysis of 9 potential terrains and confirmed the earlier conclusions and conclusions. A review of the studies and findings made by the Institute of Earth Physics at the Academy of Sciences of the USSR was also carried out.

By Decree No. 9 / 20.03.1981 of the Council of Ministers of Bulgaria was approved the site in Belene for construction of a second NPP in Bulgaria.

2.1. NPP Belene

It is envisaged that the reactors will be initially 2 at 1000 MW, and then two more will be built, and there will be an option if there is a possibility to build another 2. According to the program of the contracts between the then existing CMEA there is envisaged construction of 3 NPPs with such reactors - in Belene, in Stendell on the territory of the former German Democratic Republic and Temelin in the former Czechoslovakia. Following the unification of Germany, the construction of the Standel NPP was terminated. Although the Temelin nuclear power plant is located close to the border of Czechoslovakia with Austria and close to Vienna, it is upholding its construction and has been in operation since 2002 and currently operates 2 blocks of 1000MW.

For the history of Belene NPP, thousands of pages have been written and countless words have been spoken. To build this strategic site, however, I think not the lack of financial resources, but the political pirouettes continue to play an important role.

Between 1982 and 1986, the Atomic Energy Investor Belene was placed in the possession of 1460 acres of arable land, 1078 acres of forest stock and 164 decares of non-cultivated land. The building permit was issued by the NSA Belene on 12.12.1987. The technical project was approved by the Ministry of Energy with Protocol No. 82 / 12.10.1988. This is the beginning of the construction of the first two power units, on the basis of the signed agreement for cooperation between the governments of Bulgaria and the then USSR. Meanwhile, many accompanying facilities and communications have been built in these years, such as roads, railway lines, power lines, embankments, drains, dwellings, etc.

For the construction of the reactors and the adjacent nodes of our headquarters, as well as those in the DDR and Czechoslovakia, the modern then-type association of the type of international cooperative with the participation of the USSR, GDR, Czechoslovakia, Poland, Hungary, Bulgaria and others is being built. Each country participates in the elaboration of specific units and details in which it is specialized and has internationally recognized specialists and enterprises. By 1991, between 25 and 80% of the necessary equipment had been delivered from the various units of Unit 1. It was more than 17 00 tonnes and represented 60% physical delivery and 40% value delivery.

The reactor compartment of the power block No. 1 is initially composed of 3 building elements, placed one above the other. The foundation area is 74.7x71.4 meters, built from elevation -6.70 m to elevation 13.20 m. The hermetic shell is a cylinder with an inner diameter of 44.80 m and a thickness of 1.20 m. It steps on a foundation slab 2.40 m thick and 66 x 66 m in size. The containment or non-sealing portion comprises the cylinder of the containment shell. At an elevation of 13.20 m, 69 000 m3 or 55% of all concrete works on the reactor compartment were completed.

The machine room is also planned to consist of 3 interconnected elements - a turbine hall, a deaerator shelf and a power stack. The concrete works in a machine room are about 80% of their total volume. The mounted and prepared metal structures of carcasses (2800t) are 70% of their total volume.3

2.2. Construction of Belene NPP

In 1990, Decision No 106 / 17.05.1990 "Financing the costs associated with limiting the construction of Belene NPP limited the financing of the construction of the plant. The next year, Alexander Tomov, in his capacity of deputy prime minister, without visiting the building and having used the expert opinion, is also preparing the Council of Ministers Prime Decision No. 288 / 28.08.1991 "To overcome the problems stemming from the suspension of the construction of Belene NPP. With the subsequent decision of the Government of Philip Dimitrov № 12 / 06.02.1992, the construction of our second NPP was actually stopped.

A decade later marked by many new expertise, opinions, games, and more. Meanwhile, care is being taken to store the equipment delivered, to conserve the construction and to preserve the equipment and materials, which leads to the expense of additional resources. According to international expertise and publications, the value of our reactor was about $ 2 billion by 1990, with just over 1 billion invested until then. To spend this money by 2002, we spend roughly as much without taking a step forward towards completing or rejecting the project. Several missions of the International Atomic Energy Agency (IAEA) were conducted during these years under the leadership of Adidar Gurpinar, Ashley Erwin and Hans Blix. The site was visited by ambassadors of leading nuclear energy countries such as Russia, France and the United States. There are also international expertise on seismic conditions with the participation of prominent Japanese specialists, Siemens, Wesinghouse and others.

In 1999, the IAEA verified the storage of the equipment supplied and gave a very high estimate of the storage conditions and its condition.

In June 2002, the National Assembly passed a new law on safe use of nuclear energy (ASUNE). At the end of 2002, the Bulgarian Government adopted Decision No. 853 / 12.12.2002, which repealed the 1991 decision to suspend the construction of Belene NPP and renewed the procedures and licensing processes in connection with the construction of the plant. An expert working group was set up by order of the Minister of Energy and Energy Resources on 7 May 2003 in connection with the construction of the plant. It includes experts from the Ministry of Energy and Energy Resources, the Ministry of Environment and Waters, the Ministry of Transport and Communications, the Ministry of Interior, the Ministry of Health, the Nuclear Regulatory Agency, the State Energy Regulatory Commission, the State Agency for Civil Protection , NEC and Bulatom.

In April 2004, the construction of the second nuclear power plant in Bulgaria was decided in principle, and by decision № 260 / 08.04.2005 the Government gave its consent to construction of a nuclear power plant at Belene site with a maximum installed capacity of 2000 MW. A public tender was announced for a procedure for the selection of a contractor for the design, construction and commissioning of Units 1 and 2 of the power plant.

By the deadline - 1 February 2006, two companies have submitted bids: ZAO "Atomstroyexport", Russia and "Skoda Alliance" consortium, Czech Republic. On October 30, 2006, it was officially announced that the Russian ZAO Atomstroyexport won the A92 option for the construction of two 1,000 MW units with pressurized water at the approved site.

On 24 January 2007 Bulgaria, in compliance with the requirements of Art. 105 of the Euratom Treaty, notified the European Commission (EC) of an agreement signed on 29.11.2006 between NEC and Atomstroyexport for the design, construction and commissioning of Belene NPP. In response, the EC is of the opinion that they are in line with the principles of the treaty and can be applied.

In the selection procedure, 10 companies are involved, 2 - Elektrabel (Belgium) and RWE (Germany) were selected after selection. The choice falls for the German company. The French "BNP Paribas" was chosen as the leading structuring and organizing bank.

On 18.08.2008, an agreement for engineering, supply and construction of Belene NPP was signed in the presence of the presidents of Bulgaria - Georgi Parvanov and Russia - Vladimir Putin. The main foreign subcontractor of the Russian company Atomstroyexport is a consortium between the French nuclear power group "Areva" and the German company "Siemens". On 05.12.2008, Appendix 5 of the Agreement of 29.11.2006 on the Order and Production of Equipment was signed.

In November 2008, the Commission officially named the Belene NPP as one of the three examples of a third-generation nuclear project and recommended that future new nuclear capacities should only be at a level of safety and cost-effectiveness like third-generation reactors.

At a later stage, in September 2009 and in January 2010, RWE and BNP Paribas were withdrawn from the project. This led to the bilinging of the project and its suspension on 28.03.2012 by a decision of the National Assembly.

After another stoppage of the construction of the plant in Bulgaria, a subscription containing 770,000 signatures for holding a national referendum was initiated. On 24.10.2012, the National Assembly decided the question of the national poll to be: "To develop the nuclear energy in the Republic of Bulgaria by building a new nuclear power plant?" And the consultation itself should be on 28.01.2013. In order to be valid the referendum, that is, it has legal value and the decision to enter into force definitively must meet two conditions:

1.Do vote at least the same number of voters as in the last parliamentary elections, ie. 4 345 450 voters 6 949 120 voters included in the electoral rolls;

2.Review with 50% + 1 of the votes to be considered legitimate.

In the absence of the required minimum number of voters for the validity of the consultation, but with a minimum of 20% voter turnout and more than half of the respondents with "yes", the Belene NPP's dispute over the return to the National Assembly , where MEPs will discuss the future of nuclear energy in Bulgaria and take the final decision on the fate of the unfinished second nuclear power plant to the Belene town of Bled, as it is in practice.

Subsequently, the solution of the matter is diminishing over time and the development of new nuclear capacities in Bulgaria is stopped.

Over the past 25 years, many committees, expert groups, etc., have been set up, whose main purpose is to delay the process, to push foreign interests and to spend money. Thus, the bill for the project swells, and instead of the planned $ 2 billion, it already exceeds three times these figures, without having done anything for the development of the construction. Over the years, there has been talk in the public space of many offenses and suspicions of money playing between public figures, politicians and experts, but that remains in the sphere of supporters. Or, as Margaret Truman, the daughter of the former US president and CIA founder Harry Truman, says, this is a "capitalist solution to a socialist problem." In 2012, the Anti-Corruption and Tax Fraud Unit of the Sofia City Prosecutor's Office initiated proceedings for crimes and damages in particularly large proportions, and in March 2015 a Prosecutor's Order was issued that the proceedings had been terminated for lack of crime.

Meanwhile, after stopping work on the project, lawsuits have begun between the Bulgarian and the Russian countries, which lasted for several years and reached the International Court of Arbitration. The decision of the Court of Arbitration in Geneva, which was announced in the summer of 2016, ordered the Republic of Bulgaria to pay the equipment of the contractor at Atomstroyexport to about € 620 million. In September 2016, following a brief debate, the National Assembly approved the NEK to postpone a state loan for payment with the Russian side, because daily delays cost the Bulgarian taxpayer approximately € 330,000.

Three scenarios are outlined in Bulgaria regarding the fate of the equipment:

1. To sell it to another country, talking hard about Iran. This scenario is unlikely due to the specificity of the product and the price we can get. We already have the bitter experience of reselling the first one, which we sold to Russia for ⅓ of cost;

2. Privatize the project by looking for a strategic investor. Such a potential investor would most likely be Russian or Chinese again, which is not perceived by some political circles who are enslaving their fictional ideals;

3. Government to continue implementing the project, meaning taxpayers to bear the costs.

There are many arguments for the development of nuclear power and there are many arguments for and against, but the time has come if we want to be a country with some weight, not a mattress, to begin to defend our interests because all the major

energy projects surround us, at the expense of our neighbors. Because with our country's development and the inadequate energy policy that our governments are leading, we will soon become an energy importer and for the same energy we use now, we will have to pay intermediaries and other countries for their delivery. In my opinion, it is vitally necessary for Bulgaria to make decisions on major strategic projects that politicians do not follow their business goals and the recommendations of their "friends", but listen to the arguments and opinions of experts and experts in the relevant fields.

3.Conclusions:

1. At the beginning of the construction of the Belene NPP, a thorough and thorough analysis of the proposed sites was made and the best option chosen, according to our and foreign specialists;

2. The Commission shall officially designate the NPP "Belene" as one of three examples of the nuclear project of the third generation and recommends future new nuclear capacity to be only level of safety and economic efficiency of this third generation reactors;

3. Dissolution of project implementation, multiple committees, expert reports, etc. procedures cost more than once the project, which further exacerbates the Bulgarian taxpayer;

4. It is necessary to find a strategic investor and to complete the project and to defend the Bulgarian national and energy interests and not foreign and lobbyist ones.

4.Literature:

1. Набатов Н. и колектив, Електроенергетиката на България,София, ТАНГРА ТанНакРа ИК, 2015, 632-690 стр.

2. Манчев Б. – АЕЦ „Белене“ – лекции пред клуб „Енергетик“, 2010 г.

3. ЦИК, Резултати от референдума : „Да се развива ли ядрената енергетика в Република България чрез изграждане на нова ядрена електроцентрала?“ , София, 2013 г.

4. Постановления и решения на МС на Република България, София,

5. Dolchinkov N. T., N. B. Nichev, Characteristics of radiation, Revista academiei for ţelor terestre NR. 2 (82)/2016;

6. Dolchinkov N. T. , N. B. Nichev, Radiation background of the atmosphere, soil and water in Bulgaria and its monitoring in the contemporary political conditions,ISJ Security & future, №1/2017;

7. Truman Margaret, Murder in the CIA, Random house New York, 1987.

TRAFIC INDICATORS IN CONTEXT OF SUSTAINABLE TRANSPORT DEVELOPMENT

Ass. M-r Stevan Kjosevski[1] , Prof. Dr Atanas Kochov[2], Assoc. Prof. Dr Aleksandar Kostikj[2], Prof. Dr Darko Danev[2]
University Mother Theresa, Skopje, Republic of Macedonia[1]
Faculty of Mechanical Engineering, Ss. Cyril and Methodius University in Skopje, Republic of Macedonia[2]
aleksandar.kostikj@mf.edu.mk

Abstract: *Sustainable transport, as one of the areas on which sustainable development should be founded, depends more and more on introduction of electric vehicles in daily traffic. This paper describes part of the results of wider research related to the analysis of all sustainable transport indicators. Since introduction of electric vehicles is supposed to be done stage by stage in the actual transport, deep understanding of its main parameters/indicators is a prerequisite for reliable analysis. The paper identifies traffic and vehicle structure parameters and rang them in hierarchic order. This structure can serve as substructure in more complex structure of all transport parameters in wider researches.*

Keywords: TRANSPORT, TRAFFIC, INDICATORS, ELECTRIC VEHICLES, SUSTAINABILITY, HIERARCHY

1. Introduction

Humanity faces number of daily challenges and future treats. Reasonable and responsible answer to them is the strategy of Sustainable Development, [1]. Figure 1 shows graphic interpretation of core terms in the system of three main pillars of contemporary life: Economy, Society, and Environment.

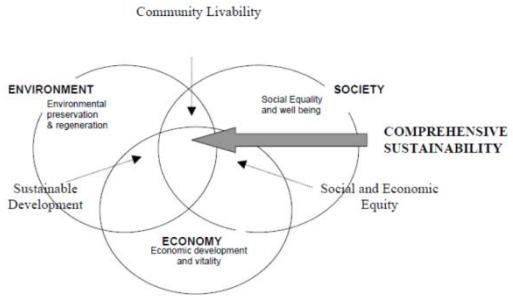

Fig. 1 *Graphical presentation of specific areas Environment, Society, and Economy form*

United Nations has defined 17 goals of sustainable development, figure 2 [1].

Fig. 2 *Goals of sustainable development*

Being one of the biggest and crucial parts in all three pillars, the importance of sustainable transport has been recognized on highest level, and number of events and documents has urged it's fast and efficient development as a contribution to the achieving Sustainable development goals, figure 3, [2].

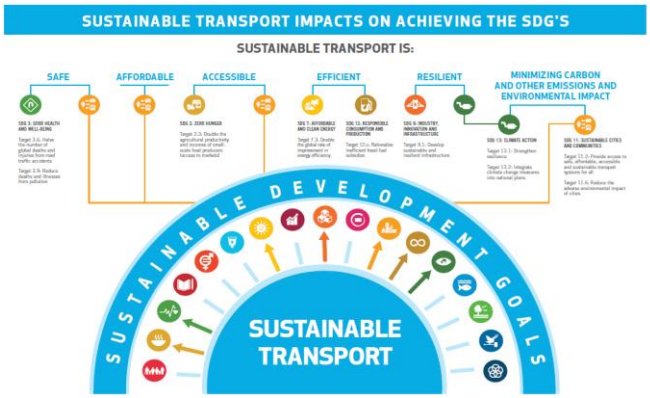

Fig. 3 *Sustainable transport impacts on achieving Sustainable development goals*

On the road to achieving sustainable transport, each country/region has to start from actual transport demand and characteristics. Together with that, all other economic, social and environmental characteristics have to be taken into account with view of alternatives available towards achieving sustainable development goals. In that process, number of decisions have to be taken, and policies created, in an environment of multi criteria and multi goals tasks. The scientific approach to those tasks employ multi criteria decision making tools, in which actual transport characteristics get a role of its indicators. That means that those indicators has to be identified, titled, structured, and measured in a way appropriately to the methodology employed.

If we take official statistical documents for different countries (example: [11]), it is easy to notice that each of them has different approach to describing the characteristics of the transport.

Different research papers deal with the challenge to define transport indicators ([4], [5], [6], [7], [8], [9], and [10]). All of them are taking those steps to deal with the research goal they have at the moment. As a result, one could make a list of big number of indicators which have number of overlaps, but there are also still big holes in terms of covering the whole area. This is especially a case if one aims to consider the capacity of electric vehicles to contribute to the sustainable transport, i.e. to the achieving the goals of sustainable development.

This research describes the effort to recognize actual transport indicators as a base for employment of multi criteria decision making tools in the context of introduction of electric vehicles as a support towards sustainable development.

2. Prerequisites and means for solving the problem

The variety of statistical data and indicators regarding transport coming from different sources shows that there is a need for their systematic collection and analysis. Based on that, a proposal for typical indicators describing the needs, intensity and structure of the actual transport could be given. This paper shows the activities undertaken in that direction for the region of Western Balkan.

All countries in the region issue annual statistical data for road transport, but very few data are directly comparable. That data are mainly related to the number of registered vehicles by their type (example on figure 4, [3], [11], [15]).

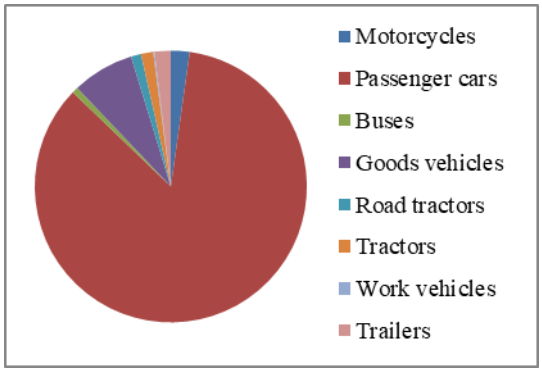

Fig. 4 *Structure of registered vehicles by their category*

Unfortunately, there are not always comparable data regarding the place of registration, their average age, or structure according to the type of the fuel.

Information about the structure of the roads, and traffic intensity are either inconsistent, or are not always present like in example: table 1, [3], [11], and [15].

Table 1: *Length and use of the roads*

	Length (km)	Kilometers passed (millions yearly)			
		Total	Motorcycles and three cycles	Passenger cars and light duty vehicles	Busses
Total length	1,724	178.4	2.2	143.5	5.6
Type of road					
All E-roads	550	63.1	0.1	55.2	1.7
Total non E-roads	1,173	115.3	2.1	88.3	3.9
Highways	37	0.6	0	0.3	0.1
Other non E-roads	1,136	114.7	2.1	88	3.8

3. Solution of the examined problem

Most of the research efforts aiming to contribute to the idea of sustainable transport define number of indicators which could serve in the process of decision making and creating appropriate policies. Those indicators make another variety, also not always consistent ([4], [5], [7], [8], [9] and [10]). The total number of such indicators varies between 10 and 88. Furthermore not all of those indicators describe the actual state of the transport and their number also varies a lot.

Described situation is proposed to be solved by standardization of the indicators, and the way their indices are measured and collected. Tables 2, 3 and 4 contain proposed transport related indicators in the economic, social, and environmental pillars, respectively, [14].

Table 2: *Economic indicators of transport*

ECONOMIC	
Transport Demand and Intensity	Infrastructure
Volume of transport relative to GDP	Per capita local road length
Vehicle prices relative to GDP	Density local road infrastructure (km-km2)
Volume of transport (passenger-km)	Parking spaces
Transport performances	

Table 3: *Social indicators of transport*

SOCIAL		
Accessibility and Mobility	Affordability	Safety and Health
Personal mobility (daily or annual person-km and trips by income group)	Private car ownership	Exposure to particulate matter (PM) and exhaust gases
Volume of passengers	Average household expenditure	Traffic noise levels
Average passenger journey time	Share of transport cost from total household expenditure	
Average passenger journey length		
No. of journeys		
Total time spent in traffic		

Table 4: *Environmental indicators of transport*

ENVIRONMENTAL		
Car Emissions	Technology Level	Impacts on Environmental Resources
Particulates emissions	Proportion of vehicle fleet meeting certain air emission standards (Euro IV, Euro V etc.)	Energy Efficiency
NOx emissions	Average age of vehicle fleet	Use of renewable energy sources in current fleet
CO emission		Use of renewable energy sources in first registered vehicles
CO_2 emissions		Transport energy consumption per capita

As mentioned, standardized transport indicators could be fully useful if the way of collection and measurement of their indices is scientifically based. An example to such approach is shown in [12] and [13].

4. Discussion of the results

Results from the research undertaken are given in the form of the tables 2, 3 and 4. Being a part of wider research ([14]), proposed indicators have been tested in the area of West Balkan. The results achieved in that process have shown that such indicators could serve for analyses of sustainability of transport. The indices of all

proposed indicators have reached very high level of consistency and give reliable source for decision making on government, municipalities, corporative and personal level.

5. Conclusion

Transport is very complex and important part of life. It has economic, environment, and social dimensions. Many decisions have to be done, and policies created in order to achieve its sustainability. In that process of multi criteria decision making first step is to recognize relevant indicators. Such indicators should be clear, understandable, measurable, and widely accepted. The indicators proposed in this paper could serve for better describing the characteristics of actual transport, as a prerequisite for its further sustainable development.

6. References

[1] United Nations, *„Transforming our World: The 2030 Agenda for Sustainable Development“*, United Nations

[2] United Nations, *„Ashgabat Statement on Commitments and Policy Recommendations of the Global Sustainable Transport Conference“*, Global Sustainable Transport Conference; Ashgabat, Turkmenistan; 27 November 2016

[3] Kjosevski Stevan, Kochov Atanas, Kostikj Aleksandar, *„An approach towards planning of electric vehicles charging infrastructure based on vehicle and transport structure“*, XXIV International scientific and technical conference “trans & MOTAUTO”, 2016, Bulgaria

[4] Attila Buzási, Mária Csete, *„Systainability Indicators in Assessing Urban Transport Systems“*, Periodica Polytechnica Transportation Engineering

[5] A. Dobranskyte-Niskota, A. Perujo, and P. Jensen, *„Indicators to Assess Systainability of Transport Activities Part 2. “*, European Commission - Joint Research Centre

[6] European Environment Agency, *„Transitions towards a more sustainable mobility system“*, TERM 2016; EEA Report no 34/2016

[7] Victoria Transport Policy Institute, *„Well Measured: Developing Indicators for Sustainable and Livable Transport Planning“*.

[8] Hippu Salk Kristle Nathan and B. Sudhakara Reddy, *„Urban Transport Sustainability Indicators - Application of Multi-view Black-box (MVBB) framework“*, Indira Gandhi Institute of Development Research, Mumbai

[9] Marie Kubáňková – Jaroslava Hyršlová – Helena Becková, *„Indicator Systems for Measuring and Monitoring Sustainability of Transport“*, The 9th International Days of Statistics and Economics, Prague, September 10-12, 2015

[10] Monika Eisenhammerová, *„Sustainable Transport Indicators“*, Number 4, Volume XI, December 2016

[11] Државен завод за статистика, *„Транспорт и други услуги, 2015“*, Државен завод за статистика Република Македонија

[12] Иванов Вл., К.Стоилова, *„Сравнителен анализ на методи за измерване на характеристиките на транспортен трафик“*, Technics Techologies Education Safety 31.5-3.06.2017 Veliko Tarnovo, 3, 2017, ISSN:2535-0315, 239-244

[13] Иванов Вл., *„Измерване на характеристики на транспортен трафик“*, XXV International Scientific-Technical Conference "trans&MOTAUTO" 28.06.–01.07.2017 Burgas, Bulgaria, 2, 2017, ISSN:2535-0307, 112-115

[14] Stevan Kjosevski, *„Decision-making and policy to introduce electric vehicles as a contribution to regional sustainable development“*, PhD Thesis, Skopje, 2018

[15] Kjosevski Stevan, Kochov Atanas, Kostikj Aleksandar, *„Vehicles and traffic structure as core aspects towards introducing electric vehicles in Republic of Macedonia“*, 26th JUMV International Automotive Conference Science and Motor Vehicles, Belgrade, 19 - 20 April 2017

SEDIMENT RECYCLE AFTER BIODIESEL PRODUCTION

ПЕРЕРАБОТКА ОСАДКОВ, ОБРАЗУЮЩИХСЯ ПОСЛЕ ПОЛУЧЕНИЯ БИОДИЗЕЛЯ

Sofronkov A.N. Professor, Doctor of Engineering Science; Vasilyeva M.G. Senior Lector

Odessa State Ecological University. Odessa, Ukraine.

a_sofronkov@ukr.net

razmargo@ukr.net

The EU's energy policy is to increase the energy of renewable sources to 15% by 2020 with the production of biodiesel being ~ 7% of the total energy produced. In the field of transport energy supply the EU policy is to support the reduction of polluting gases emissions.

In 2014 biodiesel production amounted to 3.0 billion liters worldwide, ~ 90% of which was produced in Europe. The production and use of biodiesel in Germany has increased significantly due to tax exemption. This was facilitated by the established wide network of filling stations (1500).

It should be taken into account that biofuel is 1.5 times cheaper than gasoline and when biofuel is burned, just as much carbon dioxide (CO_2) is released into the atmosphere as absorbed by its plants which are its raw materials.

Table 1 shows the total amount of energy consumed when using various types of fuel.

Table 1

Total amount of energy consumed when using various types of fuel (million tons).

Fuel	1990	2000	2010	2020	2030
Gasoline	132,0	130,0	142,0	145,0	141,0
Kerosene	29,0	45,0	53,0	63,0	72,0
Diesel	103,0	148,0	182,0	208,0	224,0

However, waste remained after biodiesel production pollutes the environment [1]. The process of production is represented in the scheme.

Process scheme of biodiesel production (based on rape)

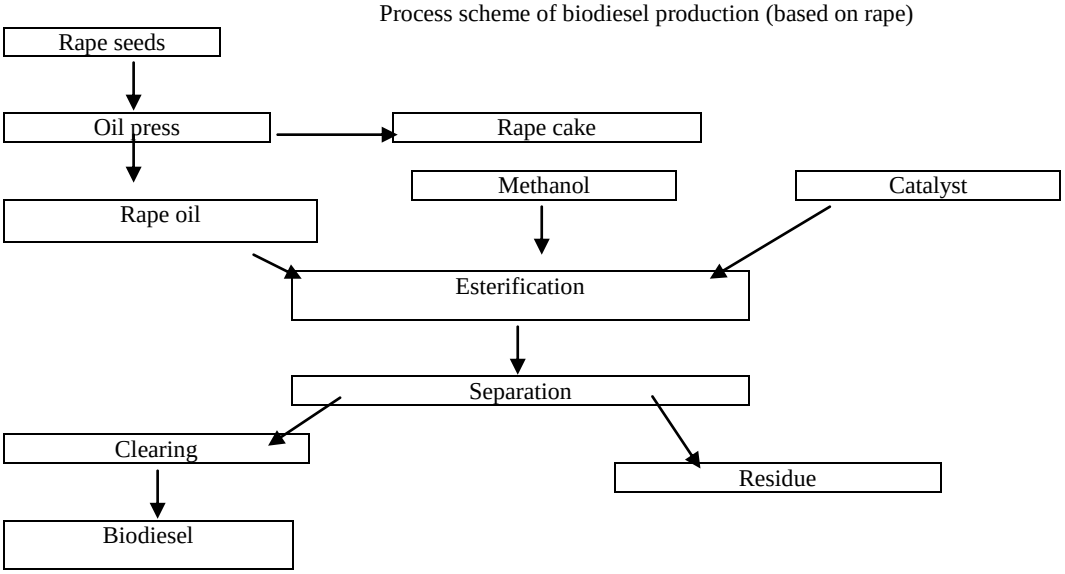

The purpose of this research is to develop a technology for processing residues remained after biodiesel production in order to reduce environmental pollution.

The material of the research is the sediment remained at factories after biofuel production.

The object was initially examined chromatographically in order to establish the composition of sediment formed after biofuel production [2]. Sediment electro-oxidation was carried out in a conventional glass cell with a separated cathode and anode space in a 7M solution of potassium hydroxide (KOH) at various electrodes (Pt, Ni-Re, Ni_2B, Co_2B, Fe_2B) at different temperatures and sediment concentrations at the Sistem-500 potentiostat. The potential was measured relative to the mercury oxide reference electrode [3]. The degree of oxidation was judged not only by the polarization curves obtained, but also by the position and magnitude of the peaks in the IR spectra taken before and after the sediment oxidation. The substances obtained again after electrooxidation were identified using various physicochemical methods of UV, IR spectroscopy [4-6]. The sediment composition studied with a chromatograph is shown in Table 2.

Table 2

The composition of the researched sediment obtained during biodiesel production at various factories

N/N	Substance	Sediment fraction	Sediment fraction	Sediment fraction
1	Glycerin	83,60	97,80	95,00
2	Esters of methyl acids C-16:0	0,10	0,15	0,10
3	Esters of methyl acids C-16:0	0,40	-	-
4	Acids C-16:0	0,10	0,10	0,08
5	Acids C-18:N	-	0,40	0,35
6	Ester of methyl acid C-22:0	-	0,06	-
7	Monoglyceride	4,50	0,20	2,00
8	Ester of methyl acid C-18:0	4,50	-	2,50
9	∑ Esters of methyl acid C-18:1+2+3	2,20	2,00	0,20
10	∑ Esters of methyl acid C-18:N	0,60	-	-

As can be seen at the table above, the composition of sediment obtained at various factories differs insignificantly.

The polarization curves obtained at sediment electro-oxidation when producing biodiesel are presented in Fig. 1.

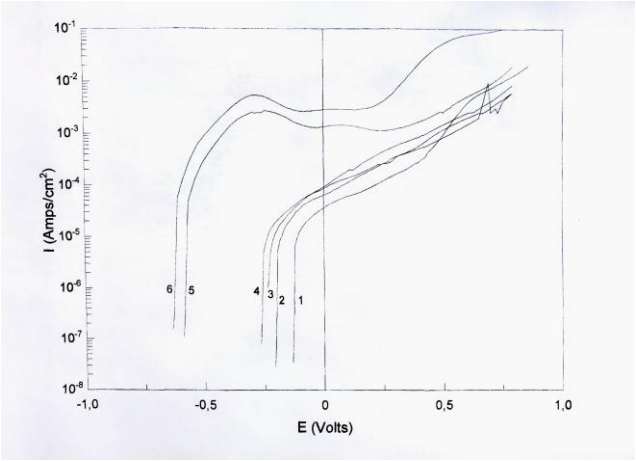

Рис 1. The polarization curves obtained at sediment electro-oxidation after biodiesel production: 1- smooth Ni; 2- Fe_2B; 3- Co_2B; 4- Ni_2B; 5- Ni-Re (303K); 6- Ni-Re (323K)

As can be seen at the figure, sediment electro-oxidation obtained in biofuel production increases for all the researched catalysts electrodes (Pt, Ni-Re, Ni_2B, Co_2B, Fe_2B) with increasing temperature and concentration in the alkaline solution (7M KOH), which is not unexpected . The potential of the working electrode was established in 3-5 minutes and was reproduced quite well while shifting into the field of large potentials with the researched sediment concentration increase. The maximum current density achieved on smooth platinum is ~ 10 mA / cm^2 at the potential of 0.3 V.

The researched catalysts (Pt, Ni-Re, Ni_2B, Co_2B, Fe_2B) were studied by X-ray diffraction analysis on unfiltered $Fe_{k\alpha}$ radiation (λ_{Fe} = 1,93 Angstrom). The URS-60 apparatus (the "powder" method, the Debye camera) was used for the X-ray check.

The Raney alloy was obtained by adding powdered nickel to the aluminum melt followed by cooling in air to room temperature. The alloy was then crushed to a powdery condition. The alloy leaching was carried out during a day in a 20% sodium hydroxide solution (NaOH). The content was then transferred to a stainless steel container and placed on a water bath for 8 hours. After the mentioned time the mother liquor was drained, the alloy was poured with a fresh 30% solution, placed in an autoclave, heated to a temperature of 353-363 K. The autoclave was cooled to a room temperature, the resulting alloy was washed with a 10% NaOH solution 3-5 times and then with distilled water to pH = 7. The resulting catalyst was stored in ethyl alcohol solution [7].

Borides of variable valence metals (Ni_2B, Co_2B, Fe_2B) were electrochemically obtained by using an electrolyte of the following composition: $NiCl_2 \cdot 6 \cdot H_2O$ (AR) - 120 g/l; $NaBH_4$ - 5g/l; NaOH - 40 g/l; Rochelle salt - 50 g/l; The bath temperature is 333 K; sedimentation time - 20 min. To slow down the hydrolysis reaction a strong alkaline medium pH>12 was used. $6Ni^{2+} + 5\ BH_4^- + 6H_2O + 7e \rightarrow 3\ Ni_2B + 2B(OH)_3 + 13\ H_2$

To establish the phase composition of the obtained borides not only X-ray phase analysis was used but the amount of boron was also determined. For that purpose the films were dissolved in "royal vodka" and boron was determined by the method [8].

Calculation of interplanar distances was carried out according to the Wolf-Brag formula [9]

$2d \sin\Theta = n\lambda$

The catalyst dispersion was carried out according to the Selyakov-Scherrer formula [10].

The crystal lattices parameters were calculated from quadratic forms for various syngonies (cubic, tetragonal, hexagonal) [11]. The results of the calculations are presented in Table 3.

Table 3

Parameters of crystal lattice in the Ni-Re alloy

Phase	Parameters of pure phases crystal lattice in the equilibrium condition			Parameters of the crystal lattice in the Ni-Re alloy		
	a , A^0	b, A^0	c,A^0	a , A^0	b, A^0	c,A^0
$Ni\ Al_3$	6,611	4,812	7,366	6,650	4,770	7,390
Ni_2Al_3	4,028	4,89	-	4,045	4,855	-
Ni Al	2,887	-	-	2,872	-	-
Ni_2B	-	-	-	4,985	-	4,253
Co_2B	-	-	-	5,027	-	4,222
Fe_2B	-	-	-	5,110	-	4,250

It is known that the catalytic activity of variable valency metal alloys depends not only on the nature and size of the catalyst surface but also on the d-characteristic surface [12].

There is a relationship between the d-characteristic, the number of electrons (z) above the argon shell and the radius of the single bond (R).

$R = 1{,}825\text{-}0{,}043z\text{-}(1{,}6\text{-}0{,}1z)\ \delta\ 10^{-2}$

There is another formula that expresses the relationship between single bond radius and fractional bond index (the ratio of valency to the coordination number)

$R = R_n + 0,3 \lg n$

So for δ we get:

$\delta = (1,825 - R_n - 0,3 \lg n - 0,043z) : (1,6 - 0,1 z);$

The change in the crystal lattice parameter due to impurities introduction and the carrier nature will lead to a change in the catalytic activity, which we observe as a more complete sediment oxidation formed in the biofuel production on Ni-Re rather than on borides of variable valency metals.

To confirm the possibility of sediment electro-oxidation, production and identification of electro-oxidation products formed after biofuel production in alkaline electrolyte, an "Specord" IR spectrometer was used. Typical IR spectra of sediment oxidized on Ni-Re are shown in Fig. 2a, b

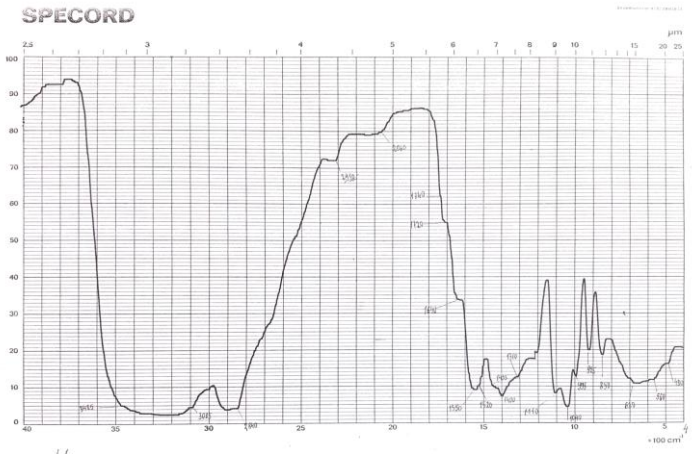

Fig. 2a

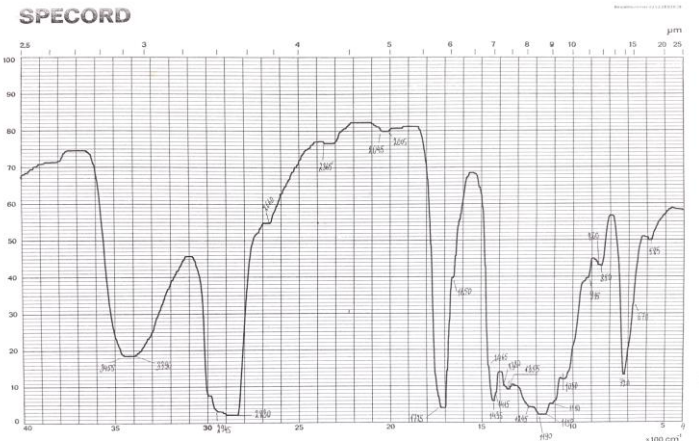

Fig. 2b

Fig. 2a,b. IR spectra recorded on the Specord spectrometer before (a) and after (b) sediment oxidation

As can be seen at the obtained spectra electro-oxidation shows significant changes in the wave number range of 2800-1550 cm^{-1} and 1550 - 650 cm^{-1}.

Sediment electro-oxidation can be represented by the following scheme

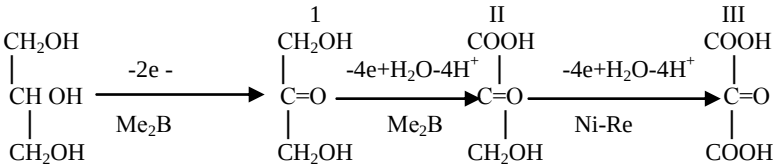

The obtained reaction products can be identified as: I-1,3-dihydroxypropanol (dihydroxyacetone), II-2-oxo, 3-hydroxypropanoic acid (hydroxyhydric acid), III-2-oxo-propanedioic acid (mesoxalic acid) - a component of lotions, emulsifiers, creams to intensify tanning, catalyst for the synthesis of esters.

This reaction was studied [13], nickel (I and II) and palladium applied to coal (III) were used as a catalyst. The use of other catalysts, Raney nickel (Ni-Re) and Me_2B borides allowed to increase the yield of the reaction product.

This research resulted in developing a technique for recycling waste generated in the biodiesel production.

It shows the possibility of a more complete electro-oxidation of generated waste using Ni - Re catalysts and a transition metal boride (Me_2B)

REFERENCES

1. Statistic in focus – Agriculture and fisheries – 3/2006. European Communities. 2006 p. p. 6.
2. Porzinskiy S., Yankovskiy M., Berman A. [Fundamentals of chromatography applications in catalysis.] Moscow: MIR, 2006. 560 p.
3. K. Vetter. Elektrochemicsche kimtik. Berlin, Gottingen, Heidelberg, 1961. 856 p.
4. Kozitsina L.A., Kupletskaya N.B., [Application of UV, IR and NMR spectroscopy in organic chemistry.] Moscow: Vysshaya shkola, 1971. 264 p.
5. Ioffe B.V., Kostikov R.R., Razin V.V. [Physical methods of determining the structure of organic molecules.] Leningrad: Leningrad university publ., 1976. 344 p.
6. Sil`versteyn R., Bassler G., Morril T. [Spectrometric identification of organic compounds]. Moscow: MIR, 1977. 590 p.
7. Yusti E., Vinzel` A. [The fuel cells]. Moscow: MIR, 1964. 480 p.
8. Nemodruk A. A., Paley P.N., Hun-I, Factory Laboratory, 1962, T.28, 6.4. p. 406-408
9. [Guide to x-ray diffraction study of the moth crystals.] Leningrad: Neva, 1975. 218 p. (Ed.: V.A. Frank-Kamenetskyi)
10. Rusakov A.A. [Radiography of metals]. Moscow: Atomizdat, 1977. 212 p.
11. Mirkin L.I. [Handbook of x-ray diffraction analysis of metals]. Moscow: Phisics-Mathematics Literatures Publ., 1961. 863 p.
12. Davtyan O.K. [Kinetics and catalysis chemical and electrode processes]. Armyanskaya SSR Academy Sciences Publ., 1984. 383 p.
13. [Electrochemistry of organic compounds]. Moscow: MIR, 1976. 731 p. (Ed. M. Bayder).

A PROCESSES CONTROL SIMULATION TOOL

Assoc. Prof. Hyniova K.
Faculty of Information Technology– Czech Technical University in Prague, Czech Republic

hyniova@fit.cvut.cz

Abstract: *The paper deals with a variable multifunctional simulation tool that enables to design and assemble animated models of various technological processes controlled by externally connected fuzzy logic unit. It enables to verify the correctness of fuzzy controller settings in the future control of real technological processes in practice. This tool represents an effective, innovative, and creative concept important to understanding control approach of technological processes modeling as an insight to behavior of real industrial processes and their control which is based on fuzzy logic. On the base of this animated simulation, real technological processes control can be realized successfully according to producer demands afterwards. Models of technological processes assembled by this simulation tool can be then externally controlled by various control strategies (traditional PID controllers, ON-OFF controllers,PLC controllers, fuzzy logic controllers etc.) via a proper real controller connected to the computer. In the paper, two-conveyor-belt system for product packing is shown. The goal consists in control of synchronization of products and boxes placed on individual conveyor belts in order to pack the product into the box. The main concern here is to improve dynamic performance and control efficiency with the help of assembling an animated model of the controlled technological process and its external control by a fuzzy logic unit.*

Keywords: CONTROL, CONVEYOR, SIMULATION, FUZZY LOGIC, PROCESS, CONTROLLER

1. Introduction

It is desirable nowadays for researchers in engineering to try to use some of their more understandable and/or practical work as a material to give an insight to behavior of real industry processes to industry technologists as much as possible. In industry, there are still mostly used PID control, sliding mode control for multi degree of freedom analytical structural systems, PLC control, fuzzy logic control, and their modifications like neuro-fuzzy techniques etc.

The main goal of the research was to create a variable multifunctional simulation system that enables to design and assemble animated models of complicated technological processes with the help of personal computers and their external control by a real fuzzy logic control unit connected to the computer. In the paper, the main concern is to study dynamic performance of conveyors synchronization and control efficiency with the help of assembling an animated model of the controlled technological process and its external control by fuzzy logic unit. The simulation technique that is discussed in the paper can take many forms and offers interesting ways for the technologists to explore and navigate them through the possibilities [1].

The presented paper reports how the work, we carried out in the areas of control of technological processes, has been used as a simulation tool to gain optimal settings of technological processes fuzzy controllers to reach the best process behavior in practice. In case of control of technological processes, the research is concerned on the development of advanced solutions in fuzzy control strategy. These solutions are simulation-based and implement an active approach whereby control schemes react to random disturbances.

2. Simulation Tool

At the Czech technical University in Prague, a variable multifunctional simulation tool that enables to design and assemble animated models of technological processes with the help of personal computers has been developed.

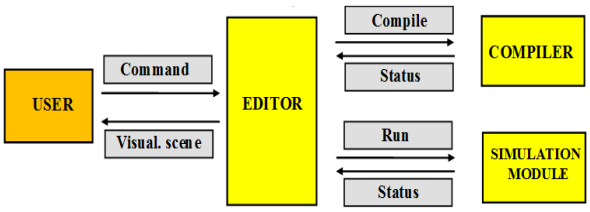

Fig. 1 *Communication between modules*

Such models of technological processes can be externally controlled by traditional PID controllers, PLCs, fuzzy logic controllers, etc.

The attention was focused on creating a universal, modular and user friendly system that would be easily extendable according to user demands. To satisfy all these requirements, we created a system with a built-in editor, compiler, and simulation modules that allows assembling wide class of technological scenes. The block diagram illustrating communication between the individual modules is shown in Fig.1.

To ensure correct understanding behavior of the simulated technological processes, we created a concept of real-time animation. The only part with the help of which standard users can build up the simulated technological scene is the editor module. It contains a library of various objects which is comfortably extendable according to user demands. The objects can be sorted into six categories:

- input objects (generators of analog and binary signals ...)
- drives
- actuators (conveyor belts, robots, start and destination points of transported subjects, ...)
- sensors (position sensors, tachogenerators, counters, etc.)
- output objects (scales, displays...)
- connections / linkages (cables, wires, pipelines)

The editor is equipped with a built-in checker for testing if all objects of the created scene are correctly located and do not cover each other. After the compilation command has been received, the compiler executes syntactic tests of the built scene and creates connections between the individual objects. If the compilation process is successful the compiler gives control back to the editor module that runs the simulation phase and announces a message about successful compilation.

In case of abortive compilation, the editor takes over the error code and announces an error message. The simulation module is represented by a simulation cycle that ensures testing of all scene objects every 50 ms. The simulation process can be externally interrupted by the user (by pushing a key) or internally by an error whose code is immediately announced in the form of an error message.

The simulation module is a useful tool to check the knowledge of hardware structure and connections in the controlled process. It leads not only to understanding which components are suitable or necessary for the real design but also gives a real imagination of all parameter levels in the process (supply voltages, actuator revolves, etc.). The simulation itself gives immediately information to the user whether the created configuration of the simulated scene is correct or not.

3. Simulated Technological Process

To illustrate a built up scene and its connection to external control executed by a fuzzy logic controller, an illustrative example-externally controlled conveyor belt process by the modular PLC C200H with fuzzy logic unit FZ001 OMRON is shown in Fig.2.

The unit is used to control two conveyor belts for products packing. The products are carried on the conveyor belt A at random intervals, but at a fixed speed. The boxes are carried in regular intervals on conveyor belt B, which runs in parallel to conveyor A at speed controlled by fuzzy logic unit. The fuzzy logic unit adjusts the speed of conveyor B so that the boxes arrive to the same point at the same time as the products. Actually, the goal is to synchronize occurrence of boxes and products at a specific place where the product will be packed in the box. The required information for conveyor B control is the offset E between the product and the box and the rate DE that the offset is changing.

The components of the simulated process and their function are given in the part list (Tab. 1).

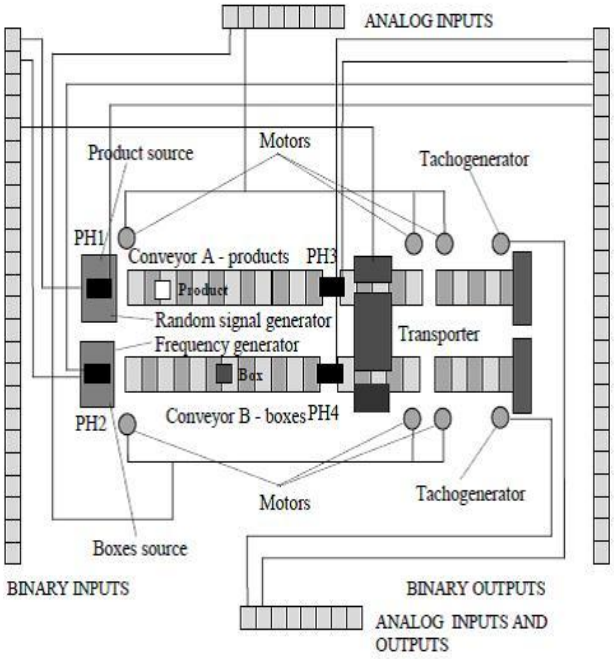

Fig. 2 *Simulated technological process - two conveyor belt system*

Table 1: *Component list*

Component	Component function
Motor A (B)	Drives conveyor belt A (B)
Tachogenerator A (B)	Tachogenerator for conveyor belt A (B)
Photoelectric sensors (4)	Sense passing products and boxes
Input unit	Receives photoelectric sensor inputs
Output unit	Outputs to motors and conveyors
Analog input unit	Converts analog speed data to digital form
Analog output unit	Converts the digital output from fuzzy logic processing to analog data and outputs it

4. Process Control

To control the technological process described above the modular PLC C200H with fuzzy logic unit FZ001 OMRON [1], [2], [3], [4], [5] is used. It controls the process via interface boards AX 5212 (8 output analog voltage/current channels) and AX 5411 (16 input and 2 output analog channels, 24 input and output binary channels) manufactured by AXIOM. External control of the simulated process is executed by PLC C200H OMRON with fuzzy logic unit FZ001 of the following configuration:

- binary inputs (sensors PH1, PH2, PH3 and PH4)
- analog inputs (conveyor A speed, Conveyor B speed)
- binary outputs (random frequency generator generating products and adjustable frequency generator generating boxes)
- analog outputs (conveyor A speed, conveyor B speed)
- PLC configuration [4] :

C200H-CPU31	C200H-FZ001
C200H-OD212	C200H-ID21
C200H-PRO15-E	C200H-DA001
C200H-AD002	C200H-BC081
C200H-LK20	

The way how to set the fuzzy controller is explained in the next paragraph. Fuzzy logic controller provides an effective tool of capturing the inexact nature of the described industrial process. Basically, fuzzy logic controller converts linguistic control rules based on expert knowledge and experience into automatic control [1]. As the process behaves randomly conventional precise mathematical control is impossible.

4. Fuzzy Controller

The basic configuration of the fuzzy logic controller is shown in Fig.3. It consists of four basic components: fuzzification interface, knowledge base, decision making logics (fuzzy inference system), and defuzzification interface.

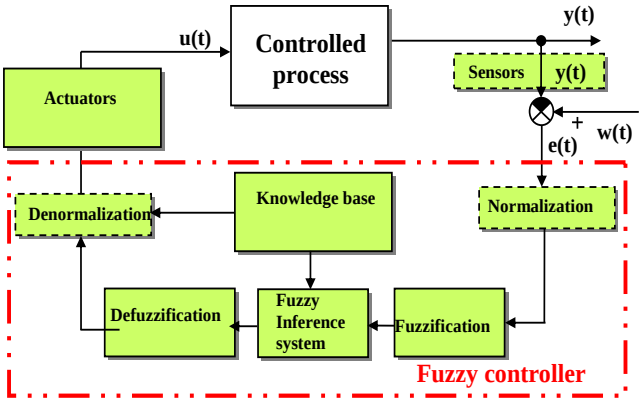

Fig. 3 *Fuzzy controller structure*

The fuzzification converts crisp output data of the controlled process into suitable linguistic variables [5].

To adjust the conveyor B speed VB to move the boxes to the same point where products occur at the same time, the information about offsets E between the products and the boxes and the rate DE that the offset is changing is necessary.

- The input data for product/box offset are taken from the relative product/box offset position E:

(1) $E=POS(Product) - POS(Box)$

- The input data for the rate of change of the offset DE is the difference between the most recent value of E (i.e. E(n)) and the previous value of E (i.e. E(n-1)):

(2) $DE=E(n)-E(n-1)$

The condition/conclusion membership functions that assign numerical values to how well a specific value of a fuzzy variable (E, DE, VB) satisfies the condition/conclusion part of the rule are shown in Fig.4.

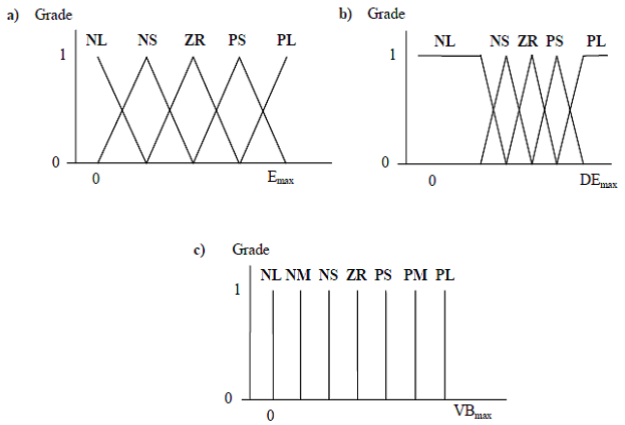

***Fig. 4**. Condition membership functions for: product/box offset E (a), offset rate of change DE (b), and conclusion membership function (conveyor B speed VB adjustment) (c)*

In Fig. 4:

- NL… Negative Large
- NM… Negative Medium
- NS … Negative Small
- ZR … Zero
- PS … Positive Small
- PM … Positive Medium
- PL … positive Large

The rules were created by organizing common know-how about the simulated process in everyday expressions. These IF-THEN statements that show how much the conveyor B speed has to be adjusted depending on E and DE are presented in Table. II.

The linguistic rules given in Tab. II need to be converted to a simplified form (Table III) than can be entered into the fuzzy logic unit.

The final result of the fuzzy logic processing for the fuzzy logic outputs is calculated by center of gravity method.

The final result of the fuzzy logic processing for the fuzzy logic outputs is calculated by center of gravity method.

The crisp value of the controller output defuzzification is calculated according to the following center of gravity formula:

$$x_T = \frac{\int_{-FFF}^{+FFF} \mu^*(x) x dx}{\int_{-FFF}^{+FFF} \mu^*(x) dx} \quad (3)$$

where $\mu^*(x)$ is the area line determined by the output value membership function. reliability and long lifetime, their usage as shock absorbers seems to be ideal.

***Table 2:** Expressing rules*

E / DE	Box is ahead a lot	Box is ahead	About even	Product is ahead	Product is ahead a lot
Box is much faster	Slow box a lot	Slow box	Slow box a little	Speed the box up a little	Speed the box up
Box is faster	Slow box a lot	Slow box	Slow box a little	Speed the box up a little	Speed the box up
About even	Slow box a lot	Slow box a little	Do not change	Speed the box up a little	Speed the box up a lot
Box is slower	Slow box	Slow box a little	Speed the box up a little	Speed the box up	Speed the box up a lot
Box is much slower	Slow box	Slow box a little	Speed the box up a little	Speed the box up	Speed the box up a lot

***Table 2:** Converting to lables*

Offset / Rate of Change DE	Product/box Offset E				
		NL	NS	ZR	PS	PL
	NL	NL	NM	NS	PS	PM
	NS	NL	NM	NS	PS	PM
	ZR	NL	NS	ZR	PS	PL
	PS	NM	NS	PS	PM	PL
	PL	NM	NS	PM	PM	PL

Centre of gravity method computes the center of gravity of singletons (Fig.4c) that have been defined by firing of any of the rules. These singletons are weighted by the given rule weight. It can be immediately verified on the computer screen that the simple knowledge base shown above gives surprisingly good results.

5. Results

A simple example of simulated externally controlled technological process has been presented. A series of such illustrative examples is used in the university courses ”Processes Control” at the Dept. of Digital Design at the Czech Technical University in Prague to make control strategies and techniques more understandable and creative.

The simulation tool has been tested in industry, namely in a soap manufacture. On the base of the simulation, they reached satisfactory results in fuzzy logic control of synchronized conveyor belts in practice. They set the same fuzzy controller parameters like during the simulation and gained very satisfactory synchronization of products and boxes carried on the conveyer belts.

Acknowledgement: This research has been supported by the MSMT CR project INTER VECTOR No. LTV 17019.

References

[1] K.Hyniova, A. Stribrsky, “Instrumentation of Processes,” FEE CTU. Prague, pp. 160-189,2014, 1964

[2] OMRON Programming Tool for OMRON PLC, OMRON, 1996

[3] OMRON C200H – Operation Manual, OMRON, 1992

[4] OMRON C200H –FZ001Fuzzy Logic Unit-Operation Manual, OMRON, 1992

[5] L. A. Zadeh, “Outline of A New Approach to The Analysis of complex Systems and Decision Processes, Trans .Syst,. Man, Cyber. Vol-SMC- 3,No.1, pp.28-44, 1973

THERMALPHYSICAL PROPERTIES OF POLYMER MICRO- AND NANOCOMPOSITES

D.Sc., prof., Member-cor. NAS of Ukraine Fialko N., Ph.D. Sci., As. Prof. Dinzhos R., Ph.D. Sen.Res. Navrodsky R., D.Sc., prof. Prokopov V., Ph.D. Sen. Res. Sherenkovsky Yu., Ph.D. Sen.Res. Meranova N.
Institute of Engineering Thermophysics NAS of Ukraine
nmfialko@ukr.net

***Abstract**: The results of experimental studies of the thermophysical properties of high-heat-conducting polymer micro- and nanocomposite materials based on various polymer matrices (polyethylene, polypropylene, polycarbonate and polymethylmethacrylate) and fillers (carbon nanotubes, aluminum and copper microparticles) are presented. The data on study of the heat conductivity coefficient, specific heat, and heat of crystallization of the composites in question are analyzed in a wide range of changes in the mass fraction of fillers from 0.2 to 10%.*
***Key words**: THERMOPHYSICAL PROPERTIES, POLYMER MICRO- AND NANOCOMPOSITES, CARBON NANOTUBES*

1. Introduction

The prospects of using polymer micro- and nanocomposite materials are associated with a complex of their unique physical and technological characteristics [1-5]. One of the important directions of application of these materials is the use of their high-heat-conducting modifications. This circumstance makes it necessary to study the various thermophysical properties of high-heat-conducting polymer micro- and nanocomposites, such as the heat conductivity coefficient, the specific heat, the heat of crystallization, etc. It is necessary to obtain detailed information on these properties, which includes their concentration, temperature and other dependencies.

The creation of high-heat-conducting polymeric micro- and nanocomposite materials is based, as is well known, on the use of fillers with high values of the heat conductivity coefficients [6-7]. In this connection, it is of interest to consider the efficiency of using these fillers from various materials to produce the required high-heat-conducting modifications of polymer composites.

According to the available research data, the thermophysical properties of polymer micro- and nanocomposite materials substantially depend also on the type of polymer matrix [8]. This one determines the importance of using these properties for composites based on different polymer matrices.

The present article is devoted to experimental studies of the thermophysical properties of high-heat-conductivity polymer micro- and nanocomposite materials using various fillers and polymer matrices (partially crystalline and amorphous) under conditions of their different combinations.

2. Prerequisites and means for solving the problem

In the scope of this paper, the task is to create polymer micro- and nanocomposites with relatively high values of their heat conductivity coefficients λ exceeding 20 W/(m·K). The possibility of developing such composites based on partially crystalline - polyethylene (PE), polypropylene (PP) and polycarbonate (PC), and amorphous - polymethylmethacrylate (PMMA), polymeric matrices using as filler carbon nanotubes (CNTs) and microparticles of aluminum or copper is considered. The carbon nanotubes used in the studies were fabricated using the CVD method (chemical vapor deposition). The content of mineral impurities in these CNTs was ~ 0.1%. The specific surface area of the CNT, determined by the adsorption of N_2, was 190 m^2/g. The outer diameter of the CNT, found using the method of small-angle X-ray scattering, was 20 nm, the length was (1 ... 5) μm, the wall thickness was ~ 5 nm [9]. The manufacturer of carbon tubes is OOO "Spetsmash".

Aluminum and copper microparticles used as fillers were obtained from aluminum or copper sawdust by grinding them in a ball mill to form particles (0.5 ... 1) μm in size.

In order to develop high-heat-conducting polymer composites, a complex of experimental studies of their thermophysical properties was performed with a variation of the mass fraction of the filler from 0.2 to 10%. Samples of composites for the study were prepared by the method of hot pressing of the composition obtained by mixing its components in the powder state in a magnetic stirrer. The of heat conductivity coefficient of polymer composites was determined using a modified IT-λ-400 device [9]. To find the specific mass heat capacity of the composites, a differential scanning calorimetry method at the Perkin-Elmer DSC-2 installation with the modified IFA Gmb Ulm software was used.

Determination of the specific heat of crystallization q_{cr} of the investigated composites was based on the use of experimentally obtained exotherms of crystallization during cooling of composites from a melt with a given constant velocity V_t

$$q_{cr} = \frac{\int_{T_N}^{T_K} (Q_{\Pi} - Q_{\Pi}^{\max}) dT}{V_t},$$

where T - is the absolute temperature; T_N, T_K - temperature of the beginning and the end of crystallization; Q_{Π}, $Q_{\Pi}^{\max}$ - the current and maximum values of the heat flux per unit mass.

3. Results and discussion

The characteristic results of experimental studies of the dependence of the heat conductivity λ of polymer composites on the mass fraction ω of the filler are shown in Fig. 1 and 2. Here Fig. 1 corresponds linear, and Fig. 2 - the logarithmic scale along the ordinate axis. As follows from the data presented in Fig. 2, for 12 composite materials in question, there is a tendency to increase the values of λ with increasing content of fillers ω. The obtained dependences $\lambda = f(\omega)$ are characterized by the presence of the effects of a sharp change in the value of λ for certain values of the mass fraction ω of the filler. The two discontinuities in the heat conductivity coefficient on the curve $\lambda = f(\omega)$, which were discovered in the experiment, are explained within the percolation theory by the formation of continuous percolation structures of filler particles, which play the role of unique heat-conducting channels. And the first critical concentration of the filler, called the first percolation threshold, corresponds to the formation of percolation clusters, while the second critical concentration (the second percolation threshold) corresponds the formation of a percolation grid. The Table 1 shows the values of the percolation thresholds for the polymeric composites studied, determined from the experiments. As can be seen, when using all considered polymer matrices for CNT-based composites, both percolation thresholds are lower than those based on copper or aluminum microparticles. In this case, the differences in the values of the first percolation threshold for polymers filled with CNT and microparticles of aluminum or copper are relatively small. The only exception is the situation corresponding to the polymer matrix of polycarbonate filled with CNT and aluminum microparticles.

The differences in the values of second percolation threshold when using CNT, aluminum or copper microparticles as a whole are noticeably higher in comparison with the first percolation threshold.

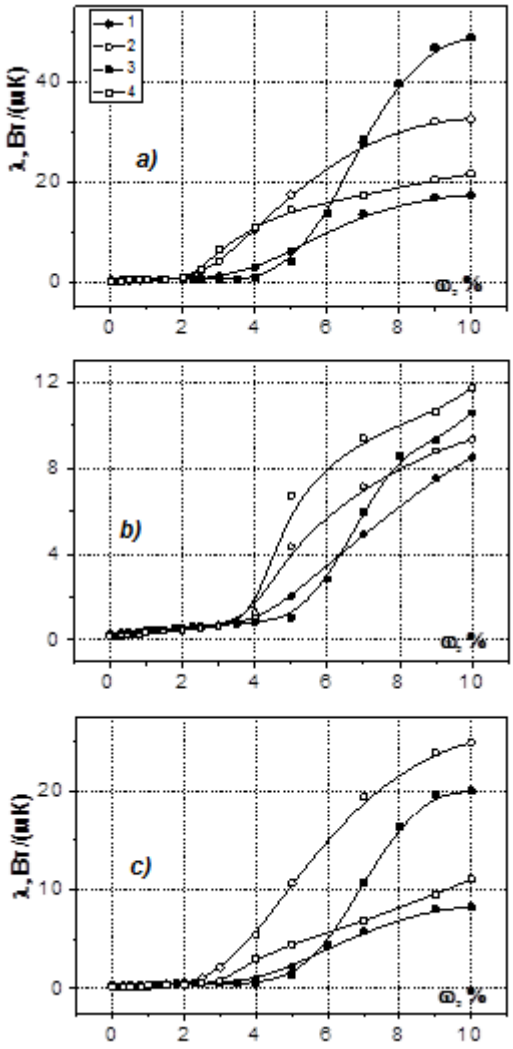

***Fig. 1**. Dependence of the heat conductivity coefficient λ of polymer composite materials on the mass fraction of the filler when using polyethylene (1), polypropylene (2), polycarbonate (3) and polymethylmethacrylate (4) as polymer matrices and for different types of filler: a) CNT; b) copper microparticles; c) aluminum microparticles*

***Table 1.** The values of percolation thresholds (%) for polymer micro- and nanocomposites studied*

Matrices \ Filler	CNT		Cu		Al	
	Percolation Threshold Number					
	1	2	1	2	1	2
PE	0.55	3.50	0.80	4.80	0.65	4.20
PP	0.40	2.80	0.65	4.50	0.85	3.40
PC	0.30	4.60	0.70	5.80	1.20	5.20
PMMA	0.55	2.30	0.85	4.20	0.80	3.50

Attention is also drawn to the lower values of the second percolation threshold when using fillers of aluminum microparticles, in comparison with microparticles of copper.

From the data shown in Fig. 1, it follows that in the range of variation of the mass fraction of the filler ω, the use of CNTs makes it possible to obtain composite materials with heat conductivity coefficient values $\lambda \geq 20$ W/(m·K) for all polymer matrices in question except for PE. When using microparticles of aluminum as the filler, these values of λ are achieved only for composites based on PP and PC. As for the filler from copper microparticles, then, as the results of the performed studies show, in this case, composites with $\lambda \geq 20$ W/(m·K) cannot be obtained for the polymer matrices in question.

According to the data obtained under these conditions, the maximum values of the heat conductivity coefficients of the composites λ_{max} are different from each other when different fillers are used. Thus, the value of λ_{max} is 48.7 W/(m·K) when using CNTs and is only 29.4 and 11.7 W/(m·K) when the polymers are filled with aluminum and copper microparticles, respectively. The indicated maximum values of λ for these fillers are achieved using different matrices, namely PC for CNT, PP for aluminum microparticles and PMMA for copper microparticles (Fig. 1).

It can be seen from Fig. 1 that when studying the heat conductivity coefficient of composites using different fillers for a particular polymer matrix, the value of λ for all polymers filled with CNTs significantly exceeds these values when they are filled with aluminum or copper microparticles in a range of ω values corresponding to $\lambda \geq 1$ W/(m·K). Regarding the ratio of the values of the heat conductivity coefficients of composites when using fillers of aluminum or copper microparticles, then in the indicated region for matrices from PP and PC, the values of λ are appreciably higher when filling polymers with aluminum microparticles.

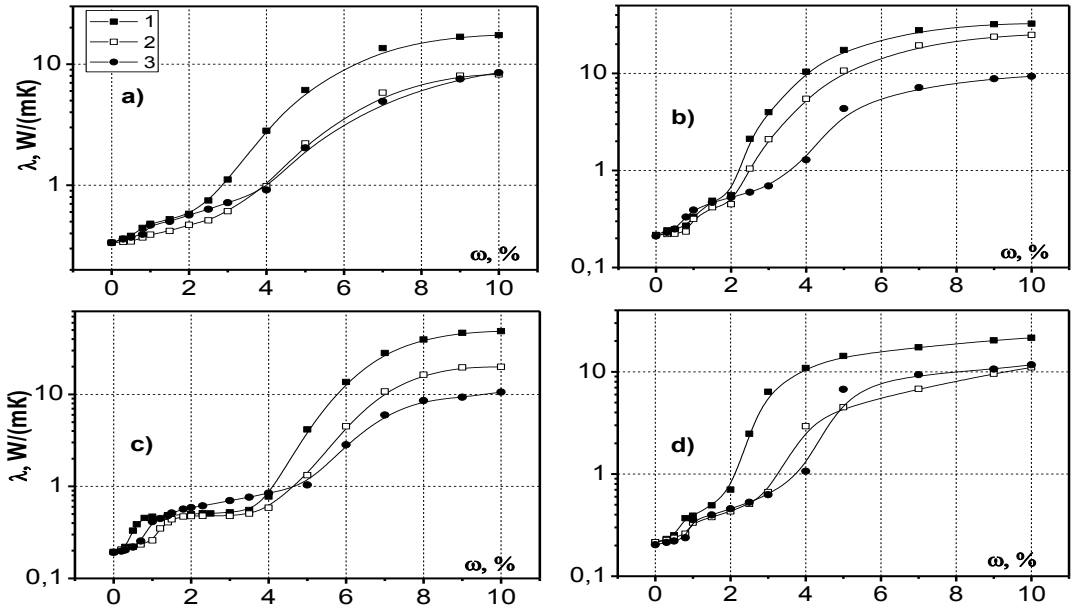

***Fig. 2.** Dependence of the heat conductivity coefficient λ of polymer composite materials on the mass fraction of the filler when polyethylene (a), polypropylene (b), polycarbonate (c) and polymethylmethacrylate (d) are used as polymer matrices and for different types of filler: 1 - CNT; 2 - aluminum microparticles; 3 - copper microparticles*

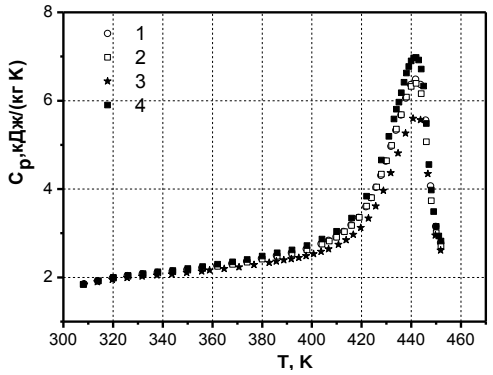

Fig. 3. *Temperature dependence of the specific heat for polymer composite materials based on polypropylene filled with aluminum (1), copper (2) and CNT (3) microparticles with filler content ω = 10%, and for an unfilled polymer matrix (4).*

For matrices from PE, the above picture as a whole is preserved with very small differences in the values of λ for the two fillers under consideration. In the case of PMMA matrices, on the contrary, the values of λ of composites filled with copper microparticles are large.

Knowledge of the temperature dependences of the specific heat of polymer composites is great interest for the practice of use of these composites. These dependencies contain information on the melting (softening) temperatures of composites, which determines the temperature intervals for possible operation of composites. In addition, they are necessary for solving nonlinear non-stationary problems of heat conductivity for equipment elements or instruments made of polymer micro- and nanocomposites.

A complex of experimental studies of the temperature dependence of the specific heat for the above-mentioned polymer composites based on PE, PP, PC and PMMA filled with CNT and aluminum or copper microparticles has been performed. Here appropriate comparisons with unfilled polymers are made. According to the obtained data, for composites based on partially crystalline polymers, a certain decrease in the heat capacity is observed in comparison with the unfilled matrix. And this manifests itself, first of all, in the zone of the maximum of the curve $c_p = f(\omega)$, which corresponds to the melting temperature of the composites. As shown by the analysis of research results, this decrease in the heat capacity values is greatest when polymers filled by CNT. The level of this decrease with respect to the maximum value of c_p for the corresponding unfilled polymer is the largest for PP-based composites and is approximately 20%, significantly lower when using a PC matrix (14%) and the lowest for the PE matrix (7%).

The decrease in the values of c_p for polymers filled with aluminum or copper microparticles, compared with the situation of an unfilled matrix, is significantly lower than when used as a filler CNT. In the case of fillers made of aluminum or copper microparticles, the decrease data are close in magnitude.

It is also noteworthy that for polymer PC and PE matrices the deviations of values c_p for composites based on aluminum or copper microparticles is very small in relation to the maximum values c_p, and for a matrix of PP these deviations are quite noticeable .

The obtained experimental results of the dependences $c_p = f(T)$ also showed that the melting temperatures for all the considered polymer composites practically do not differ from these temperatures for the corresponding unfilled matrices.

The study of the heat of crystallization q_{cr} for the polymer composites under consideration and the corresponding unfilled matrices in a wide range of variation of their cooling velocity V_t from the melt (1 ... 20 K/min) and the mass fraction of the filler ω (0.2 ... 10%) are performed. The results of the conducted studies showed that the values of the heat of crystallization of composites decrease with increasing V_t and ω. In this case, the differences in the values of q_{cr} for the composite and the corresponding unfilled matrix are greatest for composite materials based on polyethylene and substantially lower for composites based on polypropylene and polycarbonate. It is also established that for all polymer matrices, these differences depend on the filler used. They are maximum for CNTs, noticeably smaller for aluminum microparticles, and the smallest for copper microparticles (Table 2).

Table 2. *The values of the heat of crystallization, q_{cr} (J/kg), for polymer micro- and nanocomposite materials based on polyethylene, polypropylene, polycarbonate filled with CNT, aluminum or copper microparticles with an filler content of ω = 4% for different cooling velocity V_t of composites*

V_t, K/min.	Unfilled matrix			Filler								
				CNTs			Copper			Aluminum		
				Matrices								
	PE	**PP**	**PC**	**PE**	**PP**	**PC**	**PE**	**PP**	**PC**	**PE**	**PP**	**PC**
1	1624	1073	529	972	1009	448	1430	1055	508	1286	1048	501
2	782	528	262	444	468	217	684	513	247	625	507	242
5	306	209	104	160	177	84	265	202	96	237	197	95
10	146	103	52	77	83	41	131	99	48	119	96	47
20	73	51	24	37	40	10	63	51	23	56	47	20

4. Conclusions

A complex of experimental studies of the thermophysical properties of polymer micro- and nanocomposite materials obtained by hot pressing of the composition, which is formed as a result of mixing its components in the powder state in a magnetic stirrer are performed. The experiments were carried out for a wide class of composites based on various polymer matrices (polyethylene, polypropylene, polycarbonate and polymethylmethacrylate) when they were filled with CNTs or copper or aluminum microparticles in the range of 0.2-0.10% of the filler mass fraction. Wherein:

1. Experimental concentration dependences of the heat conductivity coefficients of materials are obtained and their interpretation is given on the basis of percolation theory. The possibility of obtaining polymer composites with relatively high heat-conducting properties up to λ = 48.7 W/(m·K) is shown at a relatively low filler content (up to 10%).

2. Experimental dependences of the specific heat of composites c_p on temperature are constructed. It is shown, in particular, that for composites based on partially crystalline polymers, there is a some decrease in c_p in comparison with an unfilled matrix, this decrease apparent mainly in the region of the maximum of the curve $c_p = f(T)$.

3. The values of the specific heat of crystallization of q_{cr} of polymer composite materials in a wide range of the change of their cooling velocity V_t (from 1.0 to 20 K/min) have been determined experimentally. It is shown that the heat of crystallization of composites decreases substantially with increasing velocity V_t and mass fraction of fillers ω.

5. References

1. Dinzhos R.V. Features of heat conductivity of composites on the basis of thermoplastic polymers and aluminum particles. Journal of Nanoscience and Electronic Physics. 2015. T. 7, N. 3. P. 03022-1 03022-5. (Dinzhos, R.V., N.M. Fialko, E.A. Lysenkov)
2. Dolinsky A.A. Thermophysical characteristics of high-heat-conducting polymer micro- and nanocomposites. Industrial heat engineering. 2015. №5. P. 5-15. (Dolinsky, A.A., N.M. Fialko, R.V. Dinzhos, R.A. Navrodskaya)
3. Dolinsky A.A. Thermophysical properties of low-heat-conducting polymer nanocomposites for power equipment components. Industrial heat engineering. 2015. №6. P. 5-14. (Dolinsky, A.A., N.M. Fialko, R.V. Dinzhos, R.A. Navrodskaya)
4. Dinzhos R.V. Enthalpy relaxation in the cooling/heating cycles of polyamide 6/organoclay nanocomposites. I. Non-isothermal crystallization. J. Macromol Sci. Phys. 2005. Vol. B44, – P. 421-430. (Dinzhos, R.V., E.G. Privalko, V.P Privalko)
5. Dinzhos R.V. Modeling of heat conductivity of polymer composites based on polymethylmethacrylate with different types of fillers. East European Magazine of Advanced Technology. 2015. No. 6. P. 21-24. (Dinzhos, R.V., E.A. Lysenkov, N.M. Fialko)
6. Dinzhos R.V. Analysis of heat conductivity of polymer nanocomposites filled with carbon nanotubes and carbon black. Journal of Nanoscience and Electronic Physics. 2014. T. 6. No. 1. P. 01015-1 - 01015-6. (Dinzhos, R.V., N.M. Fialko, E.A. Lysenkov)
7. Fialko N.M. Heat conductivity of polymer micro- and nanocomposites based on polyethylene with different methods of their production. Industrial heat engineering. 2017. №4. P. 21-25.(Fialko, N.M., R.V. Dinzhos, Yu.V. Sherenkovsky, N.O. Meranova, R.A. Navrodskaya)
8. Fialko N.M. Influence of the polymer matrix type on the thermophysical properties and structure formation of polymer nanocomposites. Technological systems. 2016. №3. P. 49-59. (Fialko, N.M., R.V. Dinzhos, R.A. Navrodskaya)
9. Dolinsky A.A. Thermophysical properties of polymer micro- and nanocomposites based on polycarbonate. Industrial heat engineering. 2015. №2. P. 12-18. (Dolinsky, A.A., N.M. Fialko, R.V. Dinzhos, R.A. Navrodskaya)